

AD-A264 174



WL-TR-92-2096

PULSE MITIGATION AND HEAT TRANSFER
ENHANCEMENT TECHNIQUES

VOL 2 - EFFECT OF SURFACE WETTABILITY
AND ROUGHNESS IN EVAPORATIVE SPRAY COOLING



L.C. Chow
M.S. Sehmbe
M.R. Pais
University of Kentucky
Department of Mechanical Engineering
Lexington, KY 40506-0046

AUG 1992

FINAL REPORT FOR 07/01/87 - 07/31/92

APPROVED FOR PUBLIC RELEASE; DISTRIBUTION IS UNLIMITED.

DTIC
ELECTE
MAY 03 1993
S E D

93-09301



92 4 1 07 1
AERO PROPULSION AND POWER DIRECTORATE
WRIGHT LABORATORY
AIR FORCE MATERIEL COMMAND
WRIGHT-PATTERSON AFB OH 45433-6563

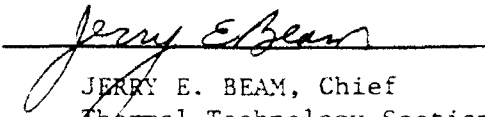
NOTICE

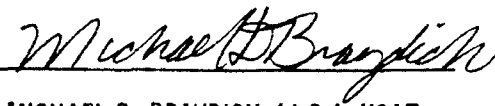
When Government drawings, specifications, or other data are used for any purpose other than in connection with a definitely Government-related procurement, the United States Government incurs no responsibility or any obligation whatsoever. The fact that the government may have formulated or in any way supplied the said drawings, specifications, or other data, is not to be regarded by implication, or otherwise in any manner construed, as licensing the holder, or any other person or corporation; or as conveying any rights or permission to manufacture, use, or sell any patented invention that may in any way be related thereto.

This report is releasable to the National Technical Information Service (NTIS). At NTIS, it will be available to the general public, including foreign nations.

This technical report has been reviewed and is approved for publication.


MICHAEL MORGAN
Project Engineer


JERRY E. BEAM, Chief
Thermal Technology Section


MICHAEL D. BRAYDICH, Lt Col, USAF
Deputy Chief
Aerospace Power Division
Aero Propulsion & Power Directorate

If your address has changed, if you wish to be removed from our mailing list, or if the addressee is no longer employed by your organization please notify WL/POOS, WPAFB, OH 45433-6563 to help us maintain a current mailing list.

Copies of this report should not be returned unless return is required by security considerations, contractual obligations, or notice on a specific document.

WL-TR-92-2096

PULSE MITIGATION AND HEAT TRANSFER
ENHANCEMENT TECHNIQUES

VOL 2 - EFFECT OF SURFACE WETTABILITY
AND ROUGHNESS IN EVAPORATIVE SPRAY COOLING



L.C. Chow
M.S. Sehmbeey
M.R. Pais
University of Kentucky
Department of Mechanical Engineering
Lexington, KY 40506-0046

AUG 1992

FINAL REPORT FOR 07/01/87 - 07/31/92

APPROVED FOR PUBLIC RELEASE; DISTRIBUTION IS UNLIMITED.

AERO PROPULSION AND POWER DIRECTORATE
WRIGHT LABORATORY
AIR FORCE MATERIEL COMMAND
WRIGHT-PATTERSON AFB OH 45433-6563

NOTICE

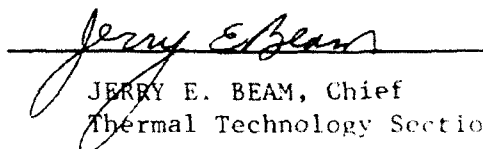
When Government drawings, specifications, or other data are used for any purpose other than in connection with a definitely Government-related procurement, the United States Government incurs no responsibility or any obligation whatsoever. The fact that the government may have formulated or in any way supplied the said drawings, specifications, or other data, is not to be regarded by implication, or otherwise in any manner construed, as licensing the holder, or any other person or corporation; or as conveying any rights or permission to manufacture, use, or sell any patented invention that may in any way be related thereto.

This report is releasable to the National Technical Information Service (NTIS). At NTIS, it will be available to the general public, including foreign nations.

This technical report has been reviewed and is approved for publication.



MICHAEL MORGAN
Project Engineer



JERRY E. BEAM, Chief
Thermal Technology Section



MICHAEL D. BRAYDICH, Lt Col, USAF
Deputy Chief
Aerospace Power Division
Aero Propulsion & Power Directorate

If your address has changed, if you wish to be removed from our mailing list, or if the addressee is no longer employed by your organization please notify WL/POOS, WPAFB, OH 45433-6563 to help us maintain a current mailing list.

Copies of this report should not be returned unless return is required by security considerations, contractual obligations, or notice on a specific document.

REPORT DOCUMENTATION PAGE			Form Approved OMB No 0704-0188	
Public reporting burden for this collection of information is estimated to average 1 hour per response, including the time for reviewing instructions, searching existing data sources, gathering and maintaining the data needed, and completing and reviewing the collection of information. Send comments regarding this burden estimate or any other aspect of this collection of information, including suggestions for reducing this burden, to Washington Headquarters Services, Directorate for Information Operations and Reports, 1215 Jefferson Davis Highway, Suite 1204, Arlington, VA 22202-4302, and to the Office of Management and Budget, Paperwork Reduction Project (0704-0188), Washington, DC 20503.				
1. AGENCY USE ONLY (Leave blank)	2. REPORT DATE AUG 1992	3. REPORT TYPE AND DATES COVERED FINAL 07/01/87--07/31/92		
4. TITLE AND SUBTITLE PULSE MITIGATION AND HEAT TRANSFER ENHANCEMENT TECHNIQUES VOL 2 - EFFECT OF SURFACE WETTABILITY AND ROUGHNESS IN EVAPORATIVE SPRAY COOLING		5. FUNDING NUMBERS C F33615-87-C-2777 PE 63218 PR D812 TA 00 WU 08		
6. AUTHOR(s) D.C. Chow M.S. Schmbey M.R. Pais				
7. PERFORMING ORGANIZATION NAME(S) AND ADDRESS(ES) University of Kentucky Department of Mechanical Engineering Lexington, KY 40506-0046		8. PERFORMING ORGANIZATION REPORT NUMBER UK-ME-92-05		
9. SPONSORING / MONITORING AGENCY NAME(S) AND ADDRESS(ES) AERONAUTICAL ENGINEERING WRIGHT LABORATORY AIR FORCE MATERIEL COMMAND WRIGHT PATTERSON AFB OH 45433-6563 WL/POOS, Attn: MORGAN 513-2552922		10. SPONSORING / MONITORING AGENCY REPORT NUMBER WL-TR-92-2096		
11. SUPPLEMENTARY NOTES				
12a. DISTRIBUTION STATEMENT APPROVED FOR PUBLIC RELEASE; DISTRIBUTION IS UNLIMITED.		12b. DISTRIBUTION CODE		
13. ABSTRACT (Maximum 200 words) In the spray cooling of a heat surface, variations in the surface contact angle cause a change in nucleation characteristics and thereby influence the heat transfer process. The surface roughness variations affect the thickness of the liquid film formed by the spray; this has a profound effect on the heat transfer from the surface. The effect of these two parameters is studied experimentally under different spray conditions involving an air atomizing nozzle.				
14. SUBJECT TERMS SPRAY COOLING, SURFACE ROUGHTNESS, CONTACT ANGLE, ATOMIZING NOZZLE			15. NUMBER OF PAGES 93	
			16. PRICE CODE	
17. SECURITY CLASSIFICATION OF REPORT UNCLASSIFIED	18. SECURITY CLASSIFICATION OF THIS PAGE UNCLASSIFIED	19. SECURITY CLASSIFICATION OF ABSTRACT UNCLASSIFIED	20. LIMITATION OF ABSTRACT UL	

TABLE OF CONTENTS

SECTION	Page
1. INTRODUCTION	1
1.1 Motivation	2
1.2 Background	3
2. PRELIMINARY EXPERIMENTS	
2.1 Experimental Description	6
2.2 Preliminary Experimental Results	8
2.3 Spray Characteristics Analysis	9
3. IMPROVED APPARATUS DESCRIPTION	22
3.1 Experimental Description	22
3.2 Droplet Diameter and Velocity Measurement	31
4. EXPERIMENTAL RESULTS	38
4.1 Introduction	38
4.2 Experimental Procedure	39
4.3 Test Results	40
5. PHENOMENOLOGICAL MODELING AND ANALYSIS	54
5.1 Effects of Spray Conditions	55
5.2 Effects of Surface Conditions	65
5.3 Analysis	70
6. DROPWISE EVAPORATION	82
6.1 Introduction	82
6.2 Experimental Investigations	83
6.3 Analytical Modeling	85
6.4 Comparison with Experimental Results	96
7. COMPARISON WITH PREVIOUS RESEARCH	98
8. CONCLUSIONS AND RECOMMENDATIONS	104
8.1 Conclusions	104
8.2 Recommendations	108
9. REFERENCES	112
APPENDIXES	
A. Uncertainty analysis	115
B. Integral Thermocouple Calibration	121
C. Experimental Results Reference	125

LIST OF ILLUSTRATIONS

Figure		Page
2.1.1	Preliminary experimental apparatus	7
2.2.1	Preliminary experimental results	8
2.3.1	Heat flux vs. superheat, test case	11
2.3.2	Volume flux distribution	12
2.3.3	Incoming droplet diameter distribution	13
2.3.4	Outgoing droplet diameter distribution	14
2.3.5	Droplet entrainment prediction	15
2.3.6	Droplet expulsion rate prediction	18
2.3.7	Heat removal capability vs. heat flux	20
3.1.1	Experimental setup block diagram	23
3.1.2	Test-surface/heater-block design	24
3.1.3	Finite element analysis results	25
3.1.4	Integral thermocouple design	27
3.1.5	Test chamber design	28
3.2.1	Droplet diameter distribution, PDPA measurement	33
3.2.2	Droplet diameter distribution, digital video measurement	34
3.2.3	Volume vs. diameter	35
3.2.4	Velocity distribution	36
4.3.1	Effects of flow rate, nozzle TG.5	41
4.3.2	Effects of flow rate, nozzle TG.7	42
4.3.3	Impingement induced mixing	44
4.3.4	Effects of orifice diameter, maximum flow rate	46
4.3.5	CHF vs. impingement frequency	47
4.3.6	Data repeatability	49
4.3.7	Effects on noncondensable gas	50
4.3.8	Effects of fluid subcooling	52
4.3.9	Effects of surface roughness	53

Figure		Page
5.1.1	Splashing measurement apparatus	59
5.1.2	Splashing measurement results	60
5.1.3	Hydraulic jump control volume	61
5.1.4	Hydraulic jump measurement apparatus	63
5.1.5	Film thickness estimation results	64
5.2.1	Active nucleation site density	67
5.2.2	Vapor bubble growth rates	69
5.3.1	Heat flux from nucleation, impingement frequency effects	73
5.3.2	Heat flux from nucleation, effects of β	74
5.3.3	Heat transfer coefficient vs. nozzle flow rate	79
6.3.1	Model geometry	89
6.3.2	Model/ANSYS comparison	93
6.3.3	Grid size comparison	94
6.3.4	Dimensionless surface temperature vs. heat flux	95
7.1.1	Effective thermal conductivity	100
B.1	Integral thermocouple calibration analysis	122
B.2	Calibration results	123
C.1	Heat flux vs. superheat, nozzle TG.3	126
C.2	Heat flux vs. superheat, nozzle TG.4	127
C.3	Heat flux vs. superheat, nozzle TG.5	128
C.4.	Heat flux vs. superheat, nozzle TG.6	129
C.5.	Heat flux vs. superheat, nozzle TG.7	130

Accession For	
NTIS CRA&I	<input checked="" type="checkbox"/>
DTIC TAB	<input type="checkbox"/>
Unannounced	<input type="checkbox"/>
Justification _____	
By _____	
Distribution /	
Availability Codes	
Dist	Avail and/or Special
A-1	

LIST OF TABLES

Table		Page
2.1	Nozzle characteristics	10
3.1	Droplet diameter and velocity measurement results	37
4.1	Nozzle volumetric flow rates	40
6.1	Comparison with experimental data	97
B.1	Thermocouple calibration results	121
C.1	Experimental results reference	125

NOMENCLATURE

A	=	Area
c_l	=	Specific heat of liquid
d	=	Diameter
$ Fo$	=	Fourier number
$ Fr$	=	Froude number
$ g$	=	Acceleration due to gravity
$ h$	=	Heat transfer coefficient
$ Ja$	=	Jakob number
$ k$	=	Thermal conductivity
$ l$	=	Plate thickness
\dot{m}	=	Mass flow rate
\dot{m}_e	=	Liquid expulsion rate
$ N$	=	Number of active nucleation sites per unit area
\dot{n}	=	Droplet impingement frequency
$ P$	=	Pressure
$ q$	=	Heat flux
$ Q$	=	Volumetric flow rate
$ Q_d$	=	Heat input to evaporating droplet
$ r$	=	Radius or radial space coordinate
$ r_c$	=	Capillary radius
$ R$	=	Radius of unit cell
$ R_h$	=	Resistance to heat transfer in droplet
$ R^+$	=	Dimensionless vapor bubble radius
$ t$	=	Time
$ t^+$	=	Dimensionless vapor bubble growth time
$ T$	=	Temperature
$ u$	=	Vapor escape velocity
$ v$	=	Velocity
$ V$	=	Volume
$ We$	=	Weber number
$ x$	=	Axial space coordinate, distance

α	=	Thermal diffusivity
β	=	Spreading ratio
δ	=	Liquid film thickness, dimensionless droplet diameter
ϵ	=	Percent of wet surface area
λ	=	Latent heat of vaporization, dimensionless axial coordinate
η	=	Dimensionless radial coordinate
ρ	=	Density
σ	=	Surface tension
μ	=	Dynamic viscosity
ω	=	Uncertainty
θ	=	Dimensionless temperature
ψ	=	Dimensionless heat flux
τ	=	Dimensionless time
V	=	Dimensionless droplet volume

Subscripts

l	Pertaining to liquid
s	Pertaining to the surface
v	Pertaining to vapor

CHAPTER 1: INTRODUCTION

This report addresses the topic of spray cooling. For this research, the region of interest is confined to surfaces above the saturation temperature of the fluid, but below the Leidenfrost point. In this region, heat is removed predominantly due to liquid/vapor phase change where the liquid is supplied to the heated surface via a liquid droplet spray. The goal of the research is to obtain a fundamental understanding of the complex phenomena associated with this type of heat transfer.

In the region defined above, spray cooling can be divided into two separate categories, which are characterized by the coolant flow rate. In the very low flow rate range, the coolant supply is matched to the heat removal, and no excess fluid is present. In this case, heat is removed by dropwise evaporation from isolated wet patches on the surface. As the flow rate is increased, the droplets begin to conglomerate causing the surface to become flooded. When the surface is flooded, excess fluid must be supplied. In this case, heat is removed by nucleation within the liquid film, and evaporation from the upper liquid/vapor interface. The main body of the report deals with high-heat-flux spray cooling, in which, the surface is flooded with water. However, a chapter is also devoted to the situation in which no excess water is present.

Experiments were conducted which help to identify the relationships between the spray and surface conditions and the heat transfer. Variation in spray characteristics, such as flow rate, droplet size and velocity, is investigated to determine how the heat transfer is affected. Factors such as liquid subcooling, noncondensable gases, and surface roughness are also investigated. Phenomenological modeling is conducted to aid in understanding the complex heat transfer and fluid flow associated with spray cooling. The modeling is useful for explaining the trends observed in the experimental data.

1.1: MOTIVATION

Many applications are arising which require the development of new, efficient cooling techniques. High efficiency and high heat flux are especially important for future high-power spacecraft and aircraft thermal management systems. Also, many electronic chips are being developed for the next generation of supercomputers which require heat removal rates beyond the capability of current cooling techniques. There are also many existing technologies which may benefit greatly if spray cooling technology is advanced sufficiently. These include areas such as cooling of X-ray tube targets and high power lasers.

The high heat flux capability of spray cooling will allow the design of compact heat exchangers necessary to meet the stringent size and weight requirements of advanced aircraft and spacecraft systems. The high efficiency is important because sensitive electronic components must be maintained at low temperature to operate reliably. At the same time, the waste heat must be rejected to the ambient. In the case of spacecraft systems, the waste heat must be rejected by radiation. For a given heat load, the radiator area is inversely proportional to the fourth power of the heat rejection temperature. Therefore, since high efficiency allows high heat rejection temperature, considerable savings in radiator size and weight can be achieved using spray cooling. Similarly, in advanced aircraft systems, the ambient temperature is fixed necessitating efficient heat transfer to minimize the size and weight of the required condenser hardware. These factors are extremely important in advanced aircraft and spacecraft since size and weight savings translate into performance improvements and cost reductions.

Another reason spray cooling may be ideal for aircraft and spacecraft is the lack of dependence on buoyancy forces for vapor removal and liquid supply. Many possible candidates for high flux removal are not suitable for aircraft or spacecraft systems because of the uncertainty concerning the effects of microgravity, or transient body forces. Other techniques are ruled out by the necessity to use highly subcooled fluid.

1.2: BACKGROUND

Current heat transfer enhancement research has been directed towards phase change processes. This is because the relatively large latent heat can be extracted with only a few degrees superheat. Many investigations have been conducted to take advantage of thin film heat transfer, including jet impingement cooling, falling film cooling, and plane wall jet cooling. Improvements over pool boiling are possible because vapor escape is not limited by interaction with the bulk fluid. Of the various types of phase change heat transfer, spray cooling holds the greatest promise for large increases in heat transfer coefficient and critical heat flux (CHF).

Analysis of previously published data for spray cooling with water indicates that the heat transfer is highly dependent on the spray characteristics. Toda performed experiments which showed that maximum heat flux values of 200 to 250 W/cm² consistently occurred at a surface superheat between 30 and 60 °C [1]. In this research, the coolant flow rates were relatively low, and droplet velocity was very high in comparison with the present research. Eastman and Ernst demonstrated that heat fluxes of up to 2000 W/cm² can be removed from a surface maintained at 300 °C [2]. This research does not provide sufficient detail in the analysis to explain the heat transfer mechanisms. There is also some question as to the accuracy of the measurement techniques. Bonacina et al. investigated dropwise evaporation in the low heat flux range using low percentages of surface saturation [3]. Heat transfer coefficients for this research ranged from 1.5 to 15 W/cm²K depending on the droplet diameter and percentage of surface saturation. Very detailed measurements and analysis are provided. It is significantly easier to define the heat transfer situation in this range of flow rate than when the surface is overflowed. Pais et al. have investigated spray cooling with air atomizing spray nozzles [4]. This research has demonstrated heat fluxes up to 1000 W/cm² with a superheat of only 5 °C. The extremely efficient heat transfer is a result of the very thin films and effective vapor removal created by the air stagnation flow field. The air flow also has the effect of reducing the partial pressure of the vapor at the liquid/vapor interface. This reduces the temperature at

which evaporation occurs. Pais et al. also conducted later studies investigating the effects of surface roughness [5]. This work showed that for very smooth surfaces, the heat transfer was greatly improved. This was due to the suppression of nucleation heat transfer and even thinner liquid films. As a result, heat fluxes comparable to the rough surface case were removed at temperatures below 100 °C. Monde has also investigated spray cooling with air atomizing nozzles. He also demonstrated heat fluxes up to 1000 W/cm² but with higher superheats (50 °C) [6]. This is thought to be due to lower air flow rates and larger diameter droplets. This creates thicker liquid films forcing more of the heat to be transferred by nucleation rather than evaporation at the upper liquid/vapor interface.

The previous experimental results show a wide variation with spray characteristics. This indicates that extensive testing is necessary to quantify the effects of the spray characteristics and develop a fundamental understanding of evaporative spray cooling. The mechanisms causing CHF must be identified and understood if spray cooling is to be successfully utilized. After presentation of the present experiments and analysis, these previous results will again be considered in Chapter 7 with the purpose of explaining the wide variation in results.

Spray cooling depends on the inter-relationship of several factors. Many of these are similar in nature to those encountered in pool boiling. For example, the critical heat flux (CHF) in pool boiling, which is the highest heat flux at which the surface remains wet, occurs when hydrodynamic instabilities cause the vapor columns to collapse. This prevents liquid/solid contact, resulting in reduced heat transfer efficiency. A similar effect resulting from the liquid/vapor interaction can be anticipated in spray cooling. If droplets are small and their velocities are low, they may become entrained in the escaping vapor and never reach the surface. They must have high enough momentum to destroy nucleating bubbles and prevent the formation of a permanent vapor barrier. However, if the droplets are too large and fast, their kinetic energy cannot be absorbed by deformation upon impact with the surface, causing disintegration, rebound, and splashing. Also, nucleation within a thin film causes liquid to be ejected from the surface when the bubble bursts. All of these effects will result in

insufficient liquid supply to the surface which causes a transition to a nonwetting surface condition. In fact, it is postulated that the CHF occurs in lower flow rate cases when a liquid deficiency results due to droplet expulsion, splashing and entrainment. When the flow rate is increased to overcome these effects, the CHF occurs due to a different mechanism. When the vapor generation rate at the surface is too high, a vapor barrier forms on the surface in a given region in the time interval between impinging droplets. The surface temperature then exceeds the Leidenfrost point resulting in a nonwetting condition.

This research effort is directed towards developing an understanding of the basic phenomena associated with the spray cooling heat transfer process. If the mechanisms causing critical heat flux are well understood, steps can be taking to minimize the effects of these mechanisms so that the CHF can be increased. Similarly, if the important factors governing efficiency are well understood, improvements can be made in this area as well.

To accomplish the above goal, a wide range of experiments and analysis was conducted. Preliminary experiments conducted to identify the important factors are presented in Chapter 2. Based on these findings, an improved apparatus was designed and constructed. The new design is presented in Chapter 3. Experimental results obtained with the new apparatus are then presented in Chapter 4. This is followed by phenomenological modeling and analysis to explain the new results in Chapter 5. In Chapter 6, work is presented to further understanding of the low surface saturation dropwise evaporation regime of spray cooling. In Chapter 7, the discussion relating the current work to that of other researchers is given. Chapter 8 presents the conclusions and the recommendations for future work. A complete uncertainty analysis for all of the work presented is given in Appendix A. A description of a new temperature measurement technique is given in Appendix B. Appendix C contains experimental and analytical data referenced throughout the report.

CHAPTER 2: PRELIMINARY EXPERIMENTS

To begin the investigation into spray cooling, preliminary experimentation to understand the spray cooling process and identify the important governing factors was performed. This section describes the experimental setup, the results obtained, and their analysis.

2.1: EXPERIMENTAL DESCRIPTION

The preliminary high power density evaporative cooling test apparatus is shown in Figure 2.1.1. The heater block is a solid copper cylinder 10 cm in diameter. Six 1,000-watt cartridge heaters are inserted into the heater block. These heaters are controlled with a rheostat so that a variable power input may be obtained. The test surface is clamped to the heater block which is supported in a plexiglas box and surrounded with ceramic fiber insulation. A machinable ceramic seal and stainless steel cover are used to protect the insulation from the spray and ensure that heat removal occurs only by evaporation from the exposed test surface. This apparatus is capable of supplying up to $1,200 \text{ W/cm}^2$ to a 2.0 cm-diameter smooth copper surface.

During testing, the temperature gradient just below the sprayed surface is measured by six thermocouples. Three thermocouples measure the temperature gradient at the centerline. The other three thermocouples measure the temperature gradient at a radial distance of 0.5 cm. A data logger records the temperature measurements and calculates the heat flux and the surface temperature.

A variable-speed magnetic drive gear pump controls the nozzle pressure accurately at the desired pressure. The pressure was measured using a standard bourdon tube gauge with an accuracy of ± 2.0 psi. The flow rate was measured using a rotometer with an accuracy of 0.21 cc/s. Four different nozzles ranging from 0.51 to 0.76 mm in orifice diameter were used. The data on droplet diameters, velocities, and flow rates for the experiments performed are presented in the following section. The distance between the nozzle and the test surface can be varied but was left at 1.9 cm for the cases presented here.

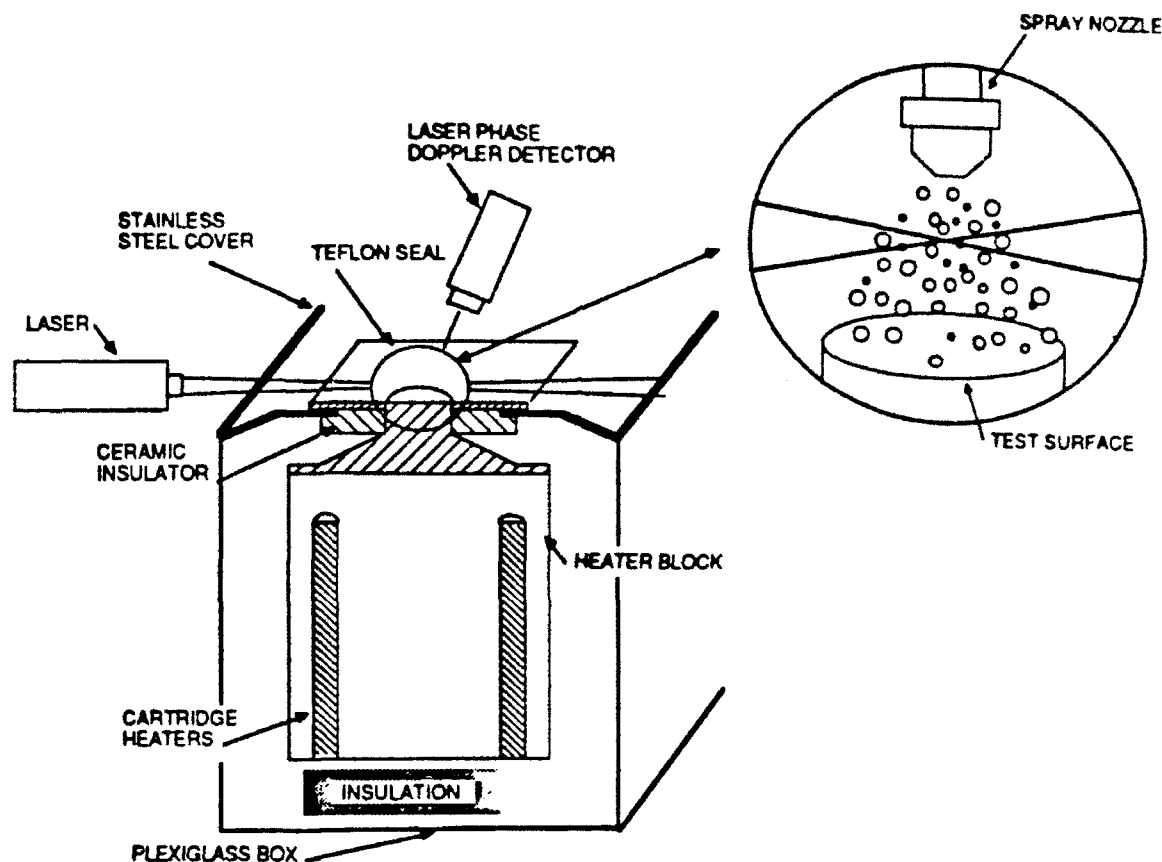


Figure 2.1.1: Preliminary experimental apparatus

For each experimental run, the following procedure was followed:

1. The surface was cleaned with acid to remove any oxidation or dirt.
2. The nozzle pressure was set to the desired value.
3. The power to the heater block was gradually increased at a rate slow enough to ensure quasi-steady measurements. The energy stored in the section just below the test surface was less than 0.1 percent of the heat removed by evaporation.
4. When the critical heat flux was reached, or the heater block temperature became too high, the heater power was turned off and the experiment was terminated.

2.2: PRELIMINARY EXPERIMENTAL RESULTS

Figure 2.2.1 presents preliminary experimental results obtained by the method described above. Nozzles 1 through 4 were all operating at 20 psig. The nozzle characteristics at this pressure are presented in Table 2.1 in Section 2.3 of this report. These first experiments show that a heat flux of over $1,100 \text{ W/cm}^2$ is removed with a surface temperature of 160°C using room temperature water. It was observed that the critical heat flux increased with increasing flow rate. Since the nozzles are pressure atomizing nozzles, the droplet diameters and velocities should not vary significantly for the different orifice sizes at the same pressure. The main difference is in flow rate. Since the percentage of the spray which is entrained or rebounded is dependent mainly on the droplet velocity and diameter distribution, the critical heat flux should be proportional to the flow rate. Examination of Figure 2.2.1 does substantiate this conclusion.

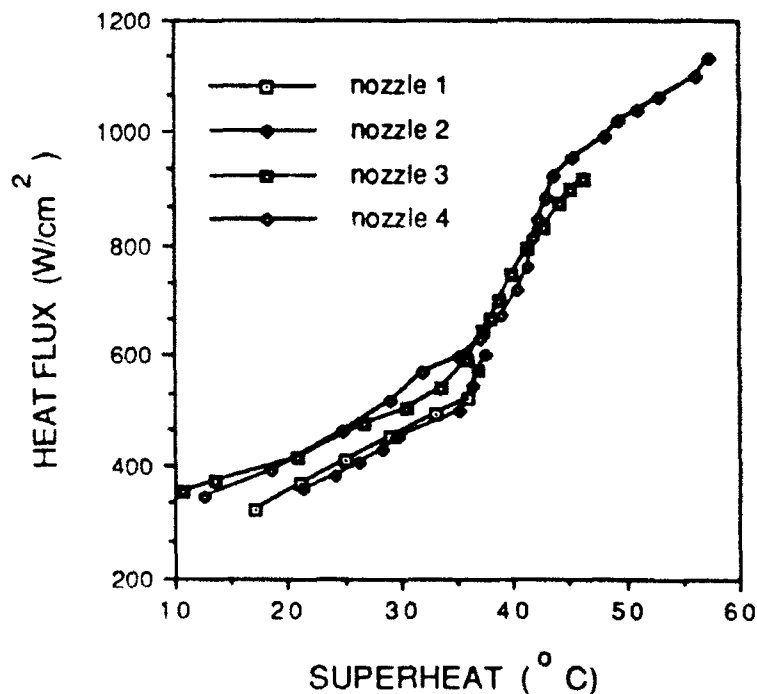


Figure 2.2.1: Preliminary experimental results

During all the experiments, the critical heat flux was always preceded by a dryout in the center of the surface which propagated radially outwards as the heat flux increased. This dryout was probably caused by a deficiency in liquid supply at the center of the surface. The deficiency occurred even though the overall flow rate was much higher than was required to remove the heat being supplied to the surface (assuming complete evaporation). The deficiency is caused by droplet entrainment, splashing, and expulsion from bursting vapor bubbles. Small, low velocity droplets become easily entrained in the escaping vapor because of their low momentum. Even though the number of entrained droplets is sometimes high, they contribute very little to the overall volume flow rate. Large droplets with high velocity have more kinetic energy than can be absorbed by impact with the liquid film. Therefore, disintegration and splashing occurs. Evidence presented later indicates that less than 10 percent of the overall volumetric flow rate is lost in this manner. The predominant mechanism by which fluid is lost is by expulsion. When a vapor bubble bursts in a thin film, liquid drops can be expelled from the surface.

Since dryout always began in the center of the surface, an analysis of the spray characteristics directly above the center of the surface may indicate the reason for the deficiency. This analysis is presented in the following section.

2.3: SPRAY CHARACTERISTICS ANALYSIS

As discussed in the previous section, the spray characteristics directly above the center of the surface were measured using a laser phase Doppler system and analyzed to determine the phenomena leading to the CHF. The measurements include droplet velocity, droplet diameter, and volume flux distributions for various experimental conditions. This section describes these measurements, the data obtained, and the relationships between the spray characteristics and the heat transfer results. An in-depth analysis of the effects of the spray characteristics on the heat transfer for one experimental case is presented. The results of this analysis are then used to explain the

heat transfer results for the other experimental cases presented in the previous section.

For the experimental results already presented, four different spray nozzles were used. The characteristics of these nozzles, operating at various pressures, influence the heat transfer. Knowledge of the droplet diameter and velocity distributions, and the volume flux profiles is of vital importance to the understanding and analysis of the experimental results. Table 2.1 shows manufacture specifications for the orifice diameter, nominal volumetric flow rate, and spray cone angle for the four nozzles tested (Spraying Systems Co.). More detailed information concerning the spray characteristics was obtained using a laser phase Doppler system.

Table 2.1: Nozzle characteristics

Nozzle	Orifice dia. (mm)	Flow Rate (cc/s)			Cone Angle	
		20 psig	30 psig	40 psig	20 psig	40 psig
1	0.51	2.64	3.28	3.78	50°	58°
2	0.56	3.61	3.58	4.36	56°	60°
3	0.69	5.36	6.31	7.58	54°	59°
4	0.76	6.31	7.58	8.83	54°	60°

The laser phase Doppler system used for this study was an Aerometrics Phase Doppler Particle Analyzer (PDPA). A detailed theoretical discussion of the procedure is reported in Reference 7. The optical configuration of the PDPA is the same as that of a conventional laser Doppler velocimeter. Light is scattered from droplets passing through the fringe patterns formed by the intersection of two laser beams. This scattered light produces another interference fringe pattern in the far field which is imaged on an aperture. The spacing of the fringes in this pattern is directly proportional to the droplet diameter. As the drop moves, the fringe pattern is swept across the aperture. Its passing is observed by three detectors located at selected spacings behind the aperture. The signal produced by each of these detectors is identical in frequency content which is used to determine the droplet velocity. However, because of the spatial separation employed between the detectors, a phase difference exists

between the signals. This phase shift is proportional to the fringe spacing and, therefore, the droplet diameter.

Measurements of the droplet velocity, diameter and volume flux distributions were made under various experimental conditions. As mentioned previously, a detailed analysis for one experimental case is presented in this section. All measurements discussed relate to nozzle number 2 operating at 25 psig with 25 °C water. The heat flux versus surface superheat curve is given in Figure 2.3.1. This figure will be referenced throughout the section and discussed in greater detail following further analysis.

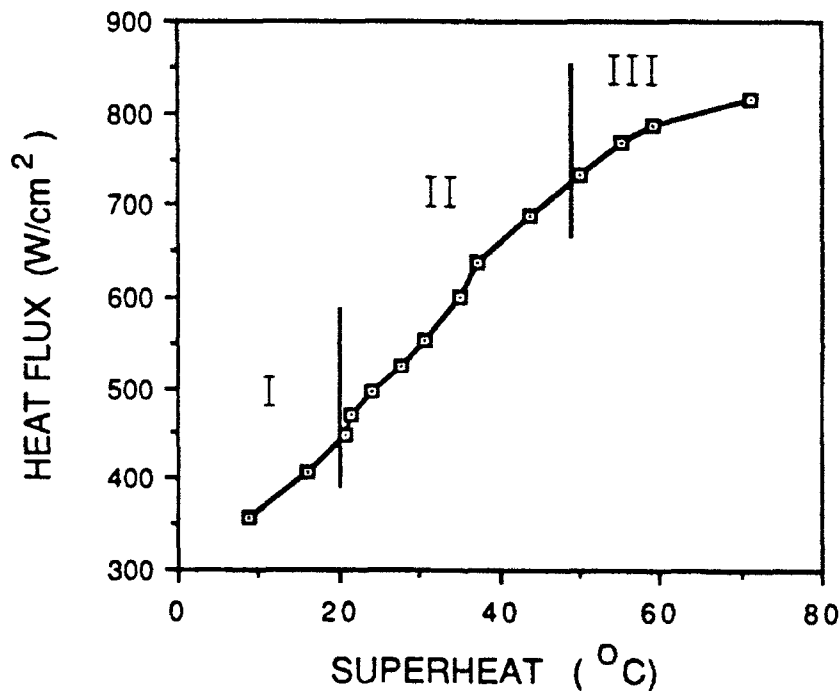


Figure 2.3.1: Heat flux vs. superheat, test case

The volume flux distribution for nozzle 2 at 25 psig was measured with no test surface present for the same spray conditions as in the test case presented in Figure 2.3.1. The curve presented in Figure 2.3.2 shows the volume flux distribution plotted against radial position within the spray. All laser phase Doppler measurements were taken at a distance of 1.55 cm from the nozzle exit (3.5 mm above the test surface). The measured volume flux integrated over the surface area was

within 3 percent of the total volumetric flow rate. When these measurements are repeated when the test surface is present, the volume flux measurements are not useful because they do not distinguish between liquid coming to the surface and liquid leaving the surface by entrainment, splashing, or expulsion.

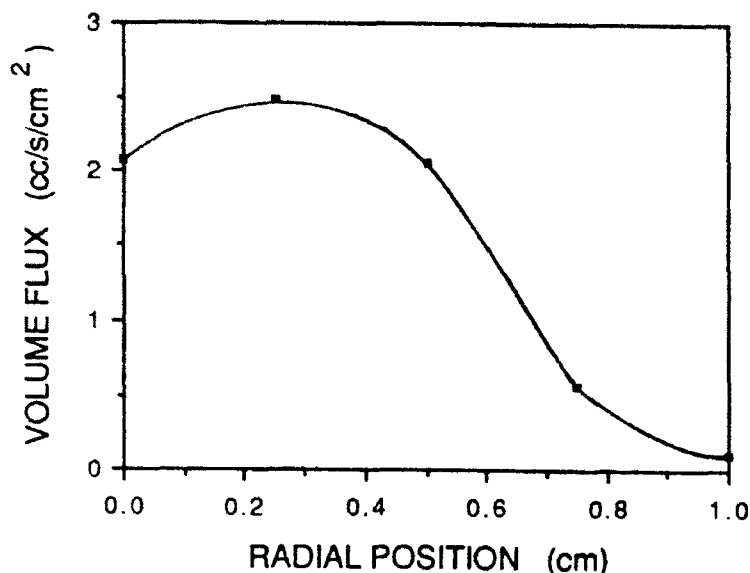


Figure 2.3.2: Volume flux distribution

From Figure 2.3.2, the incoming volume flux distribution is known. The next step is to use the LPDA measurements to determine the percentage of the incoming spray which comes back off of the surface. To do this, the total volume of droplets with positive velocities (incoming droplets) is calculated using the corresponding diameter measurements. The same is then done for the droplets with negative velocities (outgoing droplets). The percentage which comes back off of the surface is equal to the ratio of the outgoing total volume to the incoming total volume.

Histograms of the incoming and outgoing droplet diameter distributions are presented in Figures 2.3.3 and 2.3.4 for increasing heat flux for a sample size of 5,000 measurements. To determine the frequency at which the distributions repeat, the total incoming volume

can be summed and divided into the volume flux from Figure 2.3.2.

From Figure 2.3.3, it is evident that as the heat flux increases, the smaller droplets become entrained in the escaping vapor, and never reach the surface. Although the number of droplets entrained is quite large, the diameters are very small. This indicates that the droplets in the size range entrained contribute very little to the overall impinging flow rate. Therefore, the entrainment should have little effect on the heat transfer for these nozzles. However, this indicates that certain nozzles which only provide small droplets may not be suitable for high heat flux cooling.

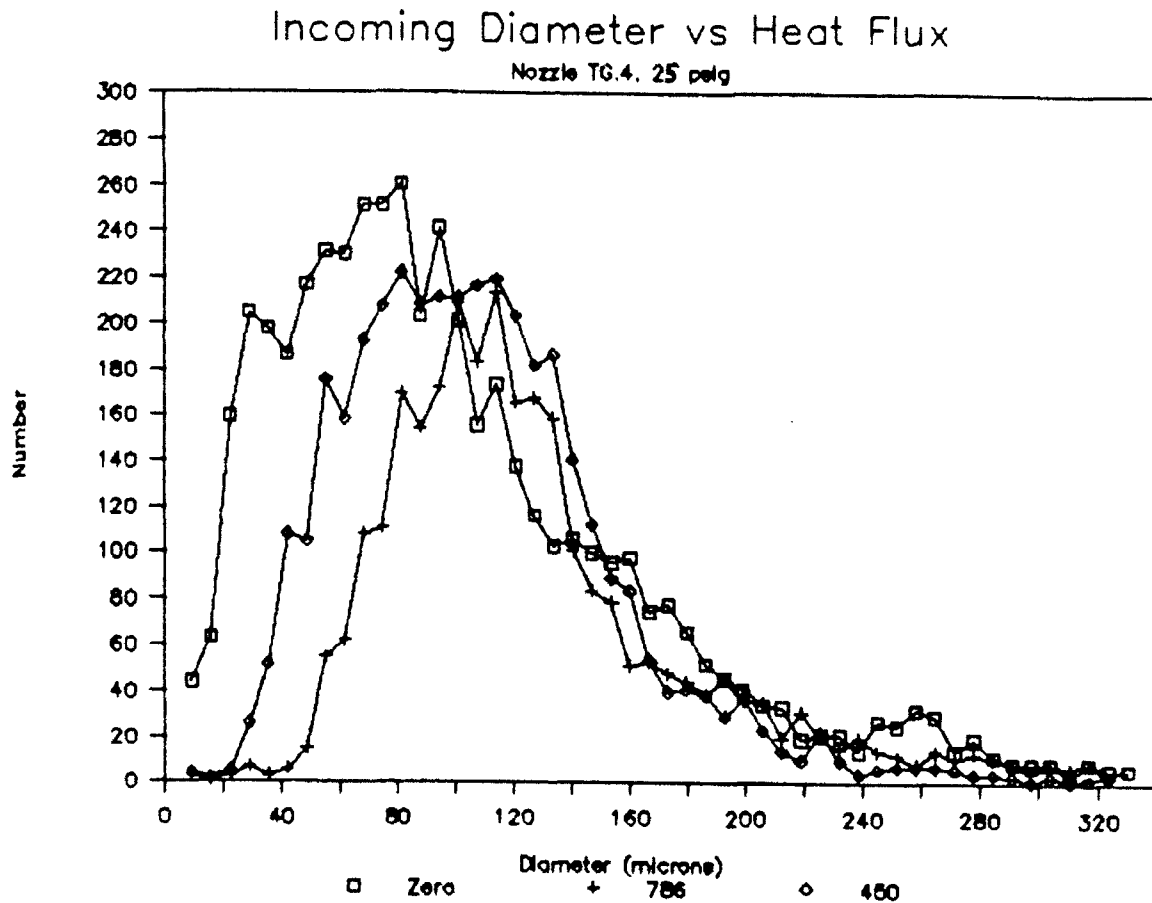


Figure 2.3.3: Incoming droplet diameter distribution

Outgoing Diameter vs Heat Flux

Nozzle TG.4, 25 psig

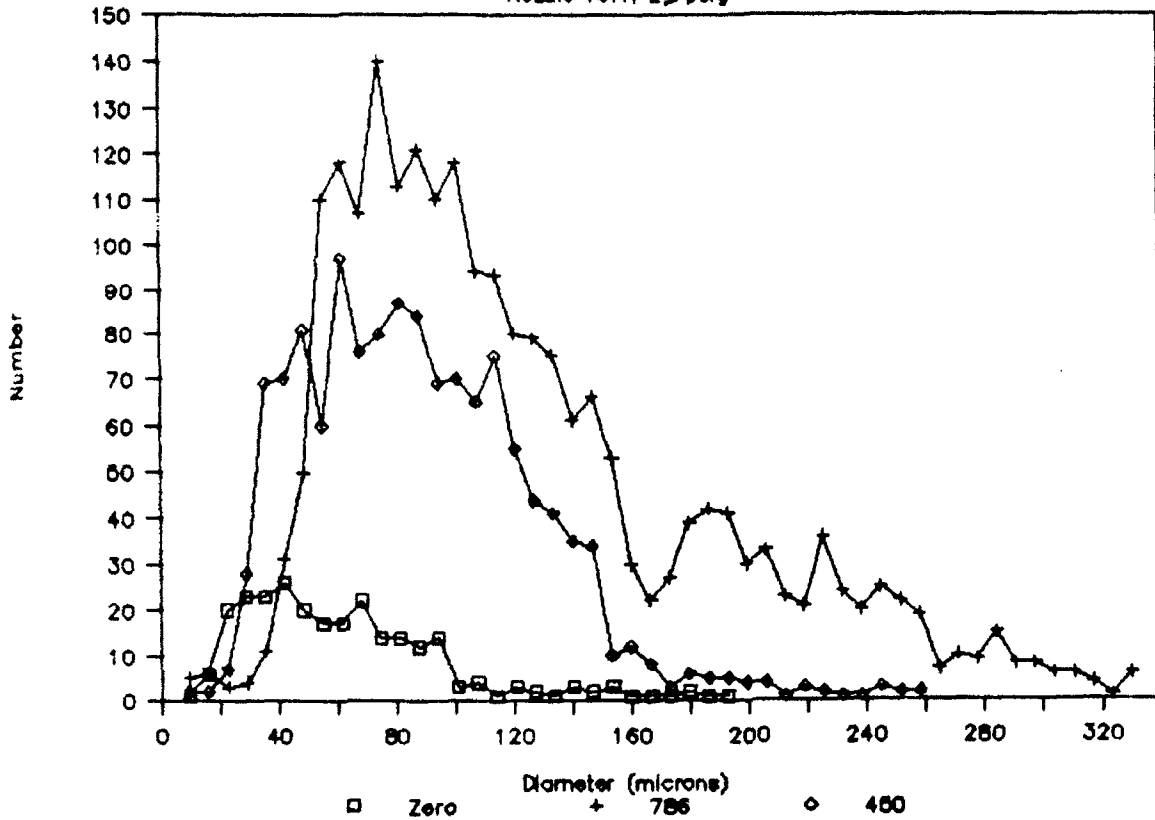


Figure 2.3.4: Outgoing droplet diameter distribution

The size range of entrained droplets can be predicted by balancing the drag on the droplet with its momentum. Equation 2.3.1 below indicates that the smaller the droplet diameter, and the lower its initial velocity, the more easily it becomes entrained in the escaping vapor:

$$(u \cdot v) = (u \cdot v_0) \exp(-18\mu_v t / \rho_l d^2) \quad (2.3.1)$$

Equation 2.3.1 was integrated between the nozzle exit and the surface and then used to plot Figure 2.3.5, which shows the prediction for the size and velocity range of droplets that would be entrained in the escaping vapor at a heat flux of 786 W/cm^2 . It was assumed that the

initial droplet velocity was equal to the average measured at zero heat flux. The volume mean diameter from the PDPA measurements was used. The vapor escape velocity was calculated from the assumption that 350 W/cm^2 was removed through phase change. The figure shows fairly good agreement with the size range entrained according to the PDPA measurements plotted in Figure 2.3.3.

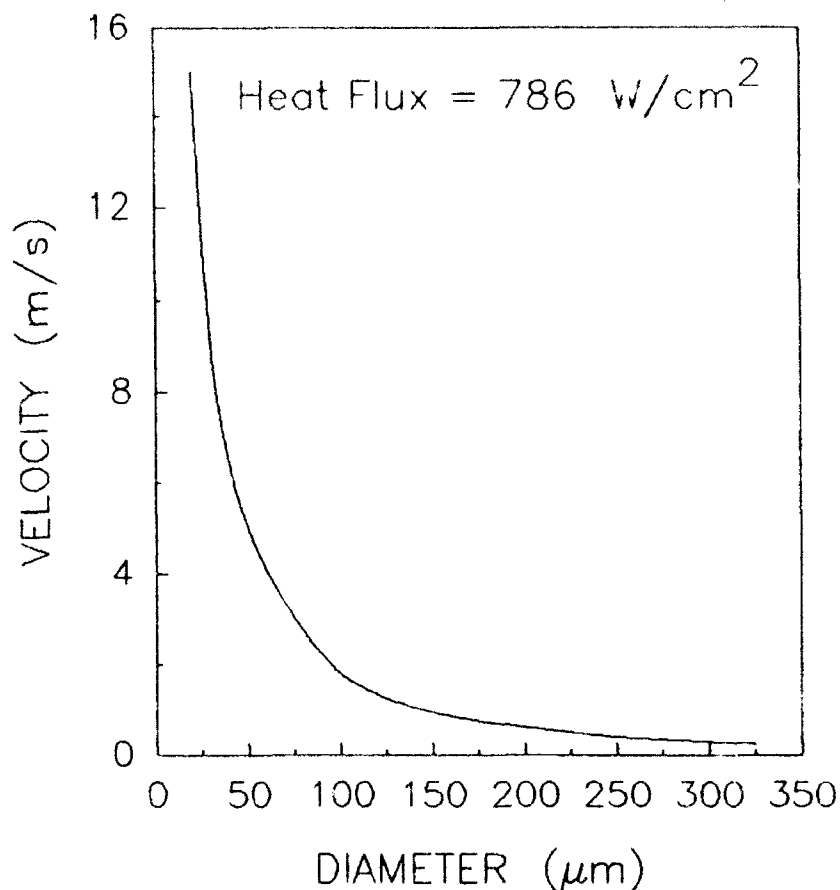


Figure 2.3.5: Droplet entrainment prediction:

Figure 2.3.4 shows the outgoing diameter distribution. The curve for the no heat flux case indicates that 1.8 percent of the impinging spray is splashed from the surface. Splashing occurs because the kinetic energy of some droplets is much higher than can be absorbed through changes in surface energy and viscous dissipation. As the heat flux to the surface is increased, the percentage of fluid which comes back off of the surface increases rapidly. At a heat flux of 450 W/cm^2 ,

the percentage has increased to 24.8 percent. At a heat flux of 786 W/cm², 87.4 percent of the impinging fluid is coming back off of the surface. This is because as the surface temperature increases, nucleation sites become activated on the surface within the thin film. This increases the instability in the liquid film and causes more splashing. Also, when vapor bubbles burst within the film, liquid is ejected from the film.

Droplet expulsion from vapor bubbles growing in a thin film has been observed and investigated in References 8,9, and 10. Toda and Monde also observed that droplet nucleation was responsible for the destruction and entrainment of the liquid film in their investigations of spray cooling [1,6]. In Reference 8, it was noted that in falling film cooling, the critical heat flux occurred in some cases due to a liquid deficiency resulting from droplet expulsion. A correlation relating the vapor generation rate and the liquid film thickness to the mass flow rate of liquid expelled from the film was given:

$$\dot{m}_e = 477(q/\lambda) \left[\frac{(q/\lambda)^2 \delta}{\sigma \rho_v} \right] \quad (2.3.2)$$

This correlation indicates that the mass flux of liquid expelled is dependent on the heat flux (removed by nucleation) and the liquid film thickness. Using equation 2.3.2, the mass flux expelled was plotted against the heat flux removed by nucleation for various values of film thickness in Figure 2.3.6. The vertical lines in the figure give the estimated range of the experimental results (liquid film thickness estimated to be between 100 and 200 μ m). The estimation in the heat flux removed by nucleation is calculated as follows:

1. Assume the heat flux at the surface can be separated into three parts: the heat removed by forced convection, the heat removed through nucleation, and the heat removed by evaporation from the upper liquid/vapor interface.
2. The heat transfer coefficient for the forced convection is assumed to remain constant as the surface temperature

increases. It can be calculated at a surface temperature of 99 °C assuming no evaporation occurs ($h = q/(99 - T_f)$). Since at the CHF, the majority of the coolant is expelled, it is difficult to estimate how close to the saturation temperature it gets before it is expelled. Assuming that 50 percent gets heated all the way, at the critical heat flux, approximately 350 W/cm² of the 786 W/cm² heat flux is removed by forced convection. Of course, this may not be very accurate considering the difficulty in the estimation.

3. Since the fluid is subcooled, very little heat is removed by evaporation at the upper/liquid vapor interface (unlike the saturated fluid cases presented later). This is because fluid must be very close to the surface to be heated to the saturation temperature. Therefore, only a fraction of what is evaporated will be due to superheat fluid which is pushed to the upper liquid/vapor interface by impinging droplets. Assuming less than 100 W/cm² is evaporated directly from the liquid/vapor interface, this leaves a heat flux of approximately 350 W/cm² which is removed by nucleation.

As seen in the figure, the prediction for mass flux of liquid expelled lies between 1.2 and 4.1 g/(s cm²) if a range of ± 50 W/cm² is assumed. The actual mass flux expelled as measured by the PDPA system is 1.8 g/(s cm²). This is 87.4 percent of the impinging volume flux at the center of the surface given in Figure 2.3.2. This comparison indicates that the correlation gives a good rough estimate of the fluid expelled if the liquid film thickness and the heat removed by nucleation are known. The correlation appears to approximate the experimental data within the error associated with the estimation of the heat flux removed by nucleation. The correlation may not be very accurate because the instability of the liquid/vapor interface created by the impinging droplets enhances expulsion. This would not occur in the falling film heat transfer case for which the correlation was derived.

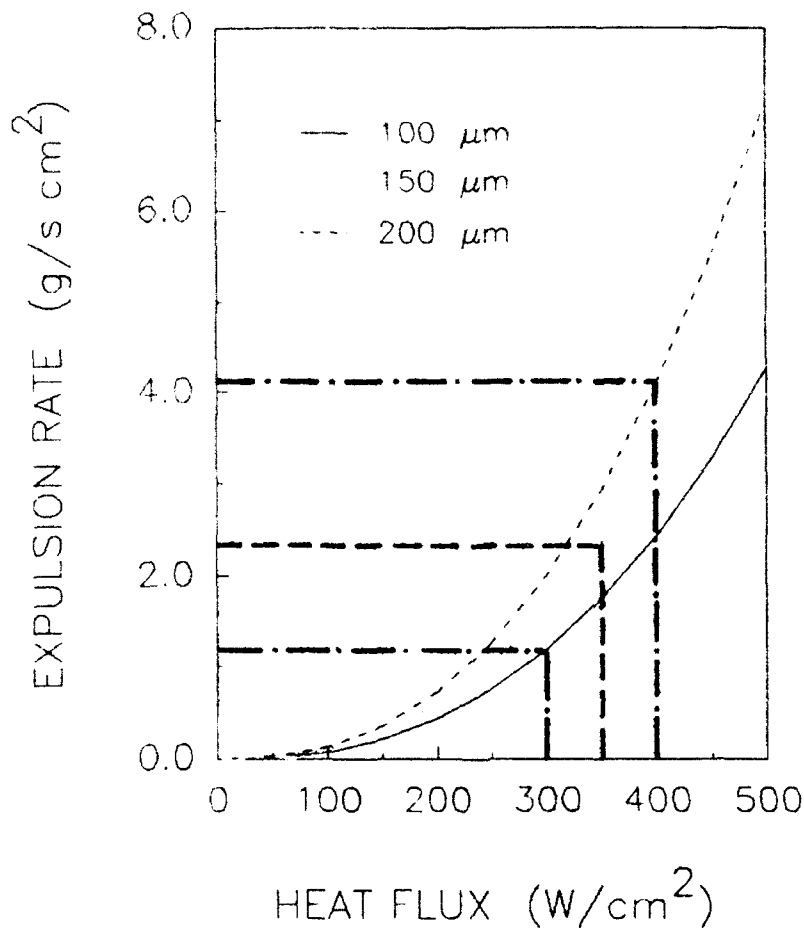


Figure 2.3.6: Droplet expulsion rate prediction

References 9 and 10 report on the phenomena of expulsion resulting from vapor bubbles bursting in a thin film. Both papers describe two separate mechanisms of droplet generation. As the vapor bubble bursts, droplets may form from the thin liquid film (bubble dome), and become entrained in the escaping vapor as it rushes out. Then, as fluid rushes in to fill the cavity created when the vapor rushes out, it collapses on itself creating a liquid jet which spouts from the surface. In many cases, this jet is unstable and a droplet forms. The references indicate that for very large vapor bubbles, the first mechanism dominates. But for small bubbles, the second mechanism dominates. Reference 9 gives a figure which plots the ratio of liquid mass expelled to vapor mass generated against the diameter of the vapor bubble. For bubbles as small as 1 mm, 10 grams of liquid are ejected for every gram

of vapor generated. For spray cooling, the vapor bubbles are generally smaller than 1 mm, but the surface is also much more unstable due to the droplet impingement. The previously described estimation of the heat flux removed by bubble nucleation can be used to calculate the vapor mass generated. The measured fluid mass expelled is about 11 times the vapor mass generated, assuming a nucleation heat flux of 350 W/cm^2 .

The above discussion indicates that the CHF for lower flow rate cases can be caused by a liquid deficiency resulting from droplet expulsion. Using the laser phase Doppler measurements, one can determine the potential heat removal capability of the spray. This includes the total latent and sensible heat content. The sensible heat content is estimated as described above (the portion removed by forced convection). The latent heat removal capability is defined as the total amount of heat that could be removed, if all of the coolant not expelled from the surface is evaporated. As the heat flux to the surface is increased, the expulsion rate increases as shown in Figure 2.3.4. Therefore, the latent heat removal capability of the spray decreases as the heat flux to the surface is increased. The sensible heat removal capability is much more difficult to estimate. As the heat flux is increased, so does the surface temperature, indicating an increase in sensible heat removal. However, fluid is also expelled from the surface. Therefore, it has less time to absorb heat resulting in reduced sensible heat removal. If it is assumed that all of the liquid not expelled is raised to the saturation temperature, and all of the liquid expelled is raised 50 percent of the way to the saturation temperature, an estimate of the sensible heat removal capability is obtained. Of course the 50 percent criterion is quite arbitrary, but should be reasonable.

Figure 2.3.7 shows the heat removal capability of the spray calculated from the PDPA measurements and the above assumptions plotted against the heat flux. The curve labeled "Total" is the sensible plus latent heat removal capability. The line labeled "Limit" is the line which indicates where the heat removal capability is equal to the heat flux. Where the total heat removal capability intersects the line, the CHF is expected to occur. The last data point on the curve was taken at a heat flux of 786 W/cm^2 . The actual critical heat flux was 814 W/cm^2 .

It appears, that if the trend of the heat removal capability curve continues, that a CHF of approximately 800 W/cm^2 is predicted. Within the limits of the experimental error, and the uncertainty in the estimation of the sensible heat removal capability, the CHF is accurately predicted by this type of comparison. This indicates that when the coolant flow rate drops below the flow rate expelled due to nucleating bubbles, the CHF results from a deficiency in liquid supply.

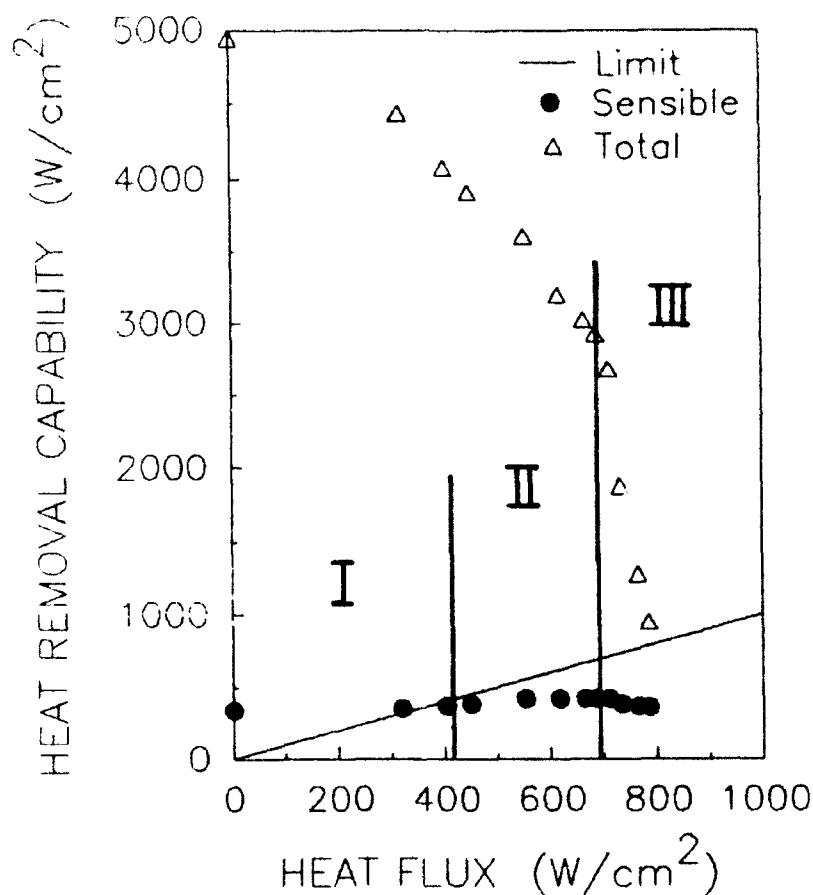


Figure 2.3.7: Heat removal capability vs. heat flux

Also, notice that three different regions are labeled on the graph in Figure 2.3.7. These same three regions were also labeled on the heat flux versus superheat graph presented in Figure 2.3.1. This shape of curve is characteristic of all the cases in which the liquid is subcooled. It appears that region I heat transfer is dominated by

forced convection. As seen in Figure 2.3.7, the sensible heat removal capability of the spray is sufficient to remove the entire heat flux. As the heat flux is increased, more heat is transferred through evaporation, and consequently, the heat transfer is more efficient. This causes the slope of the heat flux versus superheat curve to increase. The division between region two and three is placed at the location where the efficiency begins to decrease, as seen in Figure 2.3.1. On Figure 2.3.7, this is seen to be the point at which the mass flux expelled increases very rapidly, diminishing the heat removal capability of the spray. If the heat transfer coefficient is dependent on the flow rate, as fluid begins to be expelled, the flow rate, and consequently, the heat transfer coefficient both decrease.

Considering the results of the above analysis, one can reanalyze the results presented in Figure 2.2.1. It has been determined that nucleation is responsible for the expulsion which causes the transition to critical heat flux. If this is true, then one would expect a higher flow rate to yield a higher critical heat flux. As mentioned previously, as the flow rate is increased the CHF does increase. It is also noted that the temperature at which the CHF occurs increases as well. This is because more fluid must be expelled to cause the CHF. Therefore, since the surface roughness conditions do not change, the surface temperature must increase to activate more nucleation sites and increase the growth rate of the bubbles on the surface. The trends in the experimental data agree well with the proposed mechanisms causing critical heat flux.

The above analysis indicates the importance of obtaining detailed measurements. The heat transfer and fluid flow are very complex. Without these measurements, it is very difficult to interpret the data, or understand the physical phenomena. The preceding analysis provides strong evidence that the nucleation within the film is responsible for transition to critical heat flux. The droplet expulsion also has a strong influence on the heat transfer efficiency when subcooled fluid is used. The preceding analysis will be referenced in relation to the continued experimentation and analysis presented in later chapters.

CHAPTER 3: IMPROVED APPARATUS DESCRIPTION

The preliminary experiments and analysis gave much insight into understanding the spray cooling process. However, they also identified many areas for further experimentation. It was decided that greater variation in flow rate and spray characteristics should be investigated, as well as the effects of subcooling, noncondensable gases, and surface characteristics.

Also, certain problems with the initial apparatus were discovered; mainly, because of the high thermal mass, accurate determination of the critical heat flux was difficult. For very high heat fluxes, the temperature of the heater block approached the melting point of copper. Therefore, a new apparatus was designed using finite element analysis to minimize the thermal mass and the maximum temperature in the heater block. The new apparatus also featured power control based on temperature rather than heat flux. The apparatus was designed to fit into a closed system environment to facilitate study of noncondensable gases and liquid subcooling. This section describes the new apparatus design and its benefits. A section is also presented on the development of a new technique for droplet diameter and velocity measurement. The results obtained with the new apparatus are presented and analyzed based on the findings previously presented in this report and new measurements of the spray characteristics in following sections.

3.1: EXPERIMENTAL DESCRIPTION

The experimental system block diagram is presented in Figure 3.1.1. The test chamber provides a closed-system, single-component environment for the spray cooling tests. Water is drawn from the test chamber reservoir and pumped through the preheat chamber to the spray nozzle. The description of the specific components is given in the three following subsections.

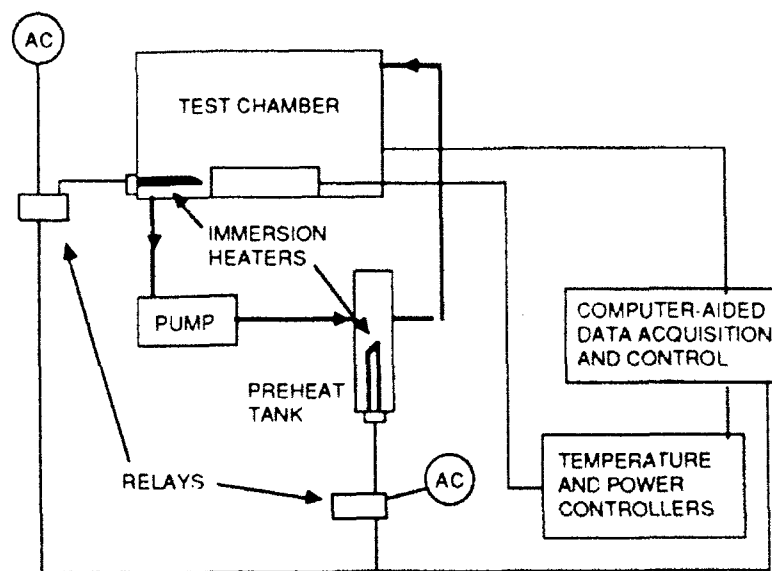


Figure 3.1.1: Experimental setup block diagram

3.1.1: Test Surface/Heater Block Design

Owing to the large thermal gradients required to drive large heat fluxes through any surface, the apparatus was carefully designed so as to arrive at temperatures within the body which maintained the physical and chemical integrity of the system. Copper was selected as the heater block material because of its high thermal conductivity. After careful review of several methods of providing high heat flux, it was decided that tungsten-in-quartz radiant heat lamps would provide the best performance.

The design of the test surface/heater block is presented in Figure 3.1.2. The heater block is placed in a brass box and surrounded by ceramic fiber insulation. The sprayed surface was sealed using a machinable glass ceramic insulator and high temperature silicon rubber sealant. The brass block was flanged so that it could be mounted in the test chamber described later.

The three high power (40 W/cm) tungsten-in-quartz heat lamps inserted into cylindrical chambers within the copper heater block provided a total heat input of 1500 Watts. This system, i.e., the tungsten filament, which can be viewed as a line element radiative heat

source, (temperature = 2,200 °C, $0.5 \leq \lambda \leq 4.5 \mu\text{m}$), enclosed within a cylinder closed at its ends, constitutes a black body. Thus, all the radiative energy is absorbed into the copper base of the heated surface. These radiation lamps have a fast thermal response (99 percent rated power within 3 secs), can withstand high temperatures by virtue of their sealed quartz envelope, and provide a high radiative heat flux.

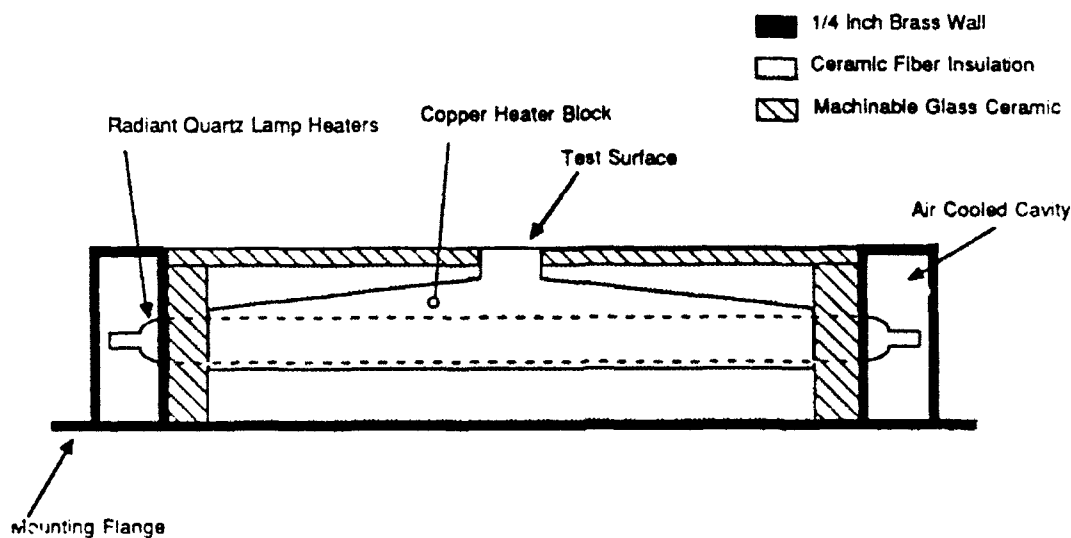


Figure 3.1.2: Test-surface/heater-block design

Before fabrication of the heated surface, an ANSYS finite element analysis of the steady-state heat conduction in the heater block was performed on the prototype. The goal of the analysis was to minimize the maximum temperatures and reduce the thermal mass. The lower temperatures not only preserve the physical and chemical integrity of the body, but also in conjunction with the lower thermal mass provide quicker heating/cooling transients.

The overall size of the heater block is dictated by the size and number of radiation lamps desired. For three lamps with a heat length of 12.5 cm, the required size of the plan section of the body is approximately 12.5 cm by 7.5 cm. Figure 3.1.3 provides the results of the finite element analysis for a surface temperature of 150 °C and heat

flux of $1,000 \text{ W/cm}^2$. This is a symmetrical quarter section of the model heater block designed with a square crown of 1-cm edge and 7-mm height. Two constantan films of $127\text{-}\mu\text{m}$ thickness are located 4 mm and 6 mm above the body surface. At locations above 3 mm, flat isotherms are observed. Therefore, the thermocouple for the final design should be located above this height. The results indicate a maximum temperature of 567°C at the lower most corner of the block. Experiments performed with a shortened crown of height 4.06 mm and a single constantan film, gave temperatures which corroborate well with the numerical predictions.

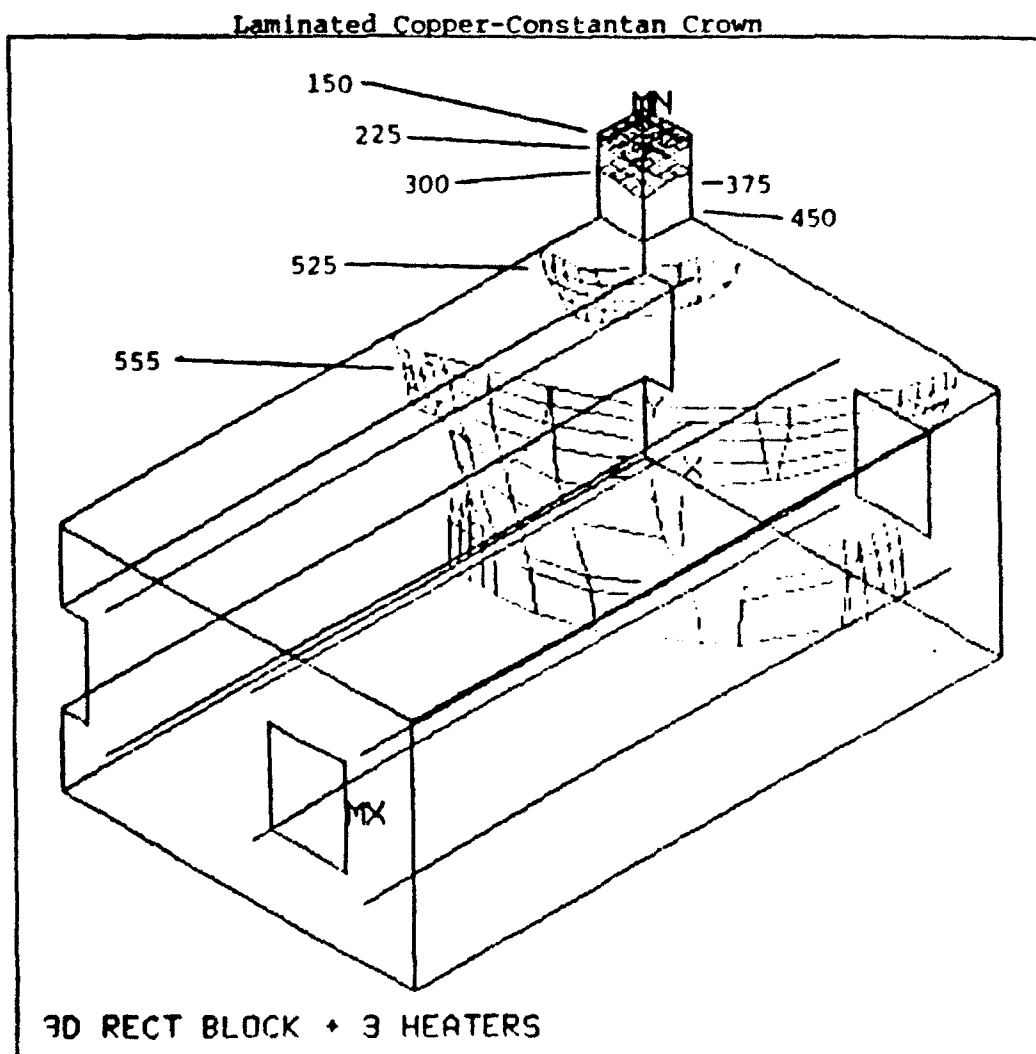


Figure 3.1.3: Finite element analysis results

For temperature measurement, an integral thermocouple design was developed as shown in Figure 3.1.4. The thermocouples are formed by silver-soldering a constantan film between the copper heater block and a 508- μm -thick copper film which forms the sprayed surface. Thus two thermocouple junctions are formed which are separated by an accurately known distance (164 μm thickness of the constantan film). The junctions are located in a region where the isotherms have flat profiles as indicated by the finite element analysis. The heat flux can then be determined using Fourier's law of heat conduction:

$$q = -k \frac{\Delta T}{\Delta x} \quad (3.1.1)$$

At a desired heat flux of 1,000 W/cm², in a copper body of uniform cross section, the temperature gradient using equation (3.1.1) is:

$$\frac{\Delta T}{\Delta x} = 25.4 \text{ } ^\circ\text{C/mm} \quad (3.1.2)$$

This requires the size of the thermocouple junction to be of the order of 40 μm for a temperature measurement resolution to be within 1 $^\circ\text{C}$. Second, a standard uncertainty analysis implies that the prediction of the heat flux is also dependent on the accurate measurement of the distance between the two thermocouples. Therefore, the integral thermocouple design provides better performance than the common method of temperature measurement using fine thermocouples because the wire sizes required are too fine at such high temperatures, being more susceptible to standard wire errors, corrosion and failure [11]. Also, with standard type thermocouple probe, uncertainty in the placement of the probe gives further uncertainty in the heat flux calculation.

The integral thermocouple construction, shown in Figure 3.1.4, is bonded together using silver solder, (Harris 50-003-1/4, 50% Ag + 15.5% Cu + 16.5% Zn + 18% Cd, liquidus 635 $^\circ\text{C}$), selected because of the high temperatures expected within the copper block. Constantan has a low thermal conductivity, (21.12 W/m $^\circ\text{K}$), thus the thinner the film, the lower the temperature rise across it. Second, the film thickness measurement, Δx , when accurately determined, reduces the uncertainty in

the heat flux prediction.

Because there is heat flow across the laminate thermocouple junction, and the silver solder layer has finite thickness, we cannot assume the junction to be isothermal. Hence, the standard copper-constantan thermocouple calibration is invalidated. Therefore, the thermocouple measurements taken during the experiments are corrected as described in Appendix B before plotting the results presented later.

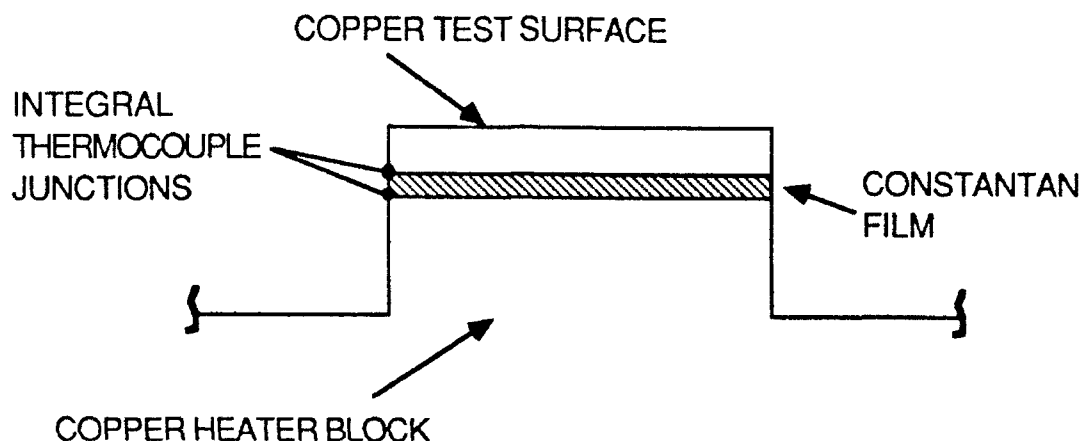


Figure 3.1.4: Integral thermocouple design

3.1.2: Test Chamber Design

The test chamber presented in Figure 3.1.5 is constructed of brass plate which is bolted together and sealed with epoxy. The heater-block/test-surface assembly is simply bolted up into the bottom of the chamber as shown. Three glass windows are located on the front and side walls to facilitate observation. The expandable columns are Neoprene bellows. These columns were flange mounted to the top of the test chamber at the base, and to a counterweighted plate at the top. Purge valves at the top of the columns were used to bleed the air from the system. The columns were very effective in maintaining constant pressure within the system. As transients in vapor generation occurred, due to cycling of the reservoir heater or increases in the surface heat flux, the columns move up or down to change the system volume. As long

as the columns remained between the maximum and minimum heights, the pressure remained constant to within 0.25 psig.

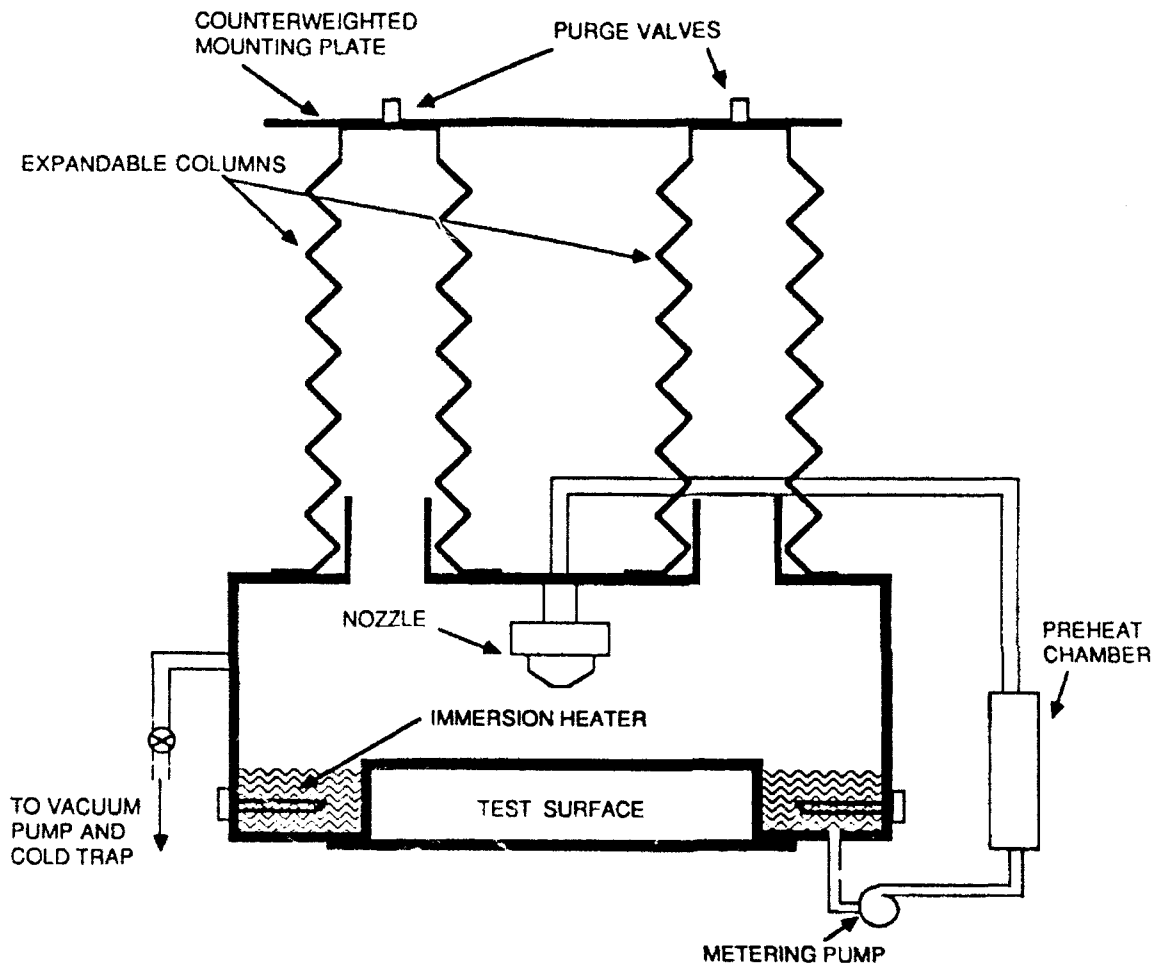


Figure 3.1.5: Test chamber design

The reservoir immersion heater was computer controlled based on the liquid temperature. The control was very effective in keeping the temperature within 0.5 °C of the set point value at all times. The liquid in the reservoir was pumped through a preheat chamber to the nozzle. The preheat chamber also contained a computer controlled immersion heater to ensure that the fluid sprayed onto the surface was at saturation. The preheat chamber also served to damp the pressure oscillations generated by the diaphragm pump to ensure that the nozzle

operated at relatively constant pressure.

The temperature of the vapor space was monitored to ensure that the majority of the air was removed from the system. As the test chamber was heated up, the air/water vapor mixture was forced through the purge valves on the tops of the expandable columns by applying pressure to the upper plate. This continued until the vapor temperature approached the saturation value. At this time, the purge valves were closed and a cold trap was evacuated with a vacuum pump. The pump was then isolated from the cold trap. A valve between the cold trap and the test chamber was then opened and the contents of the vapor space were drawn into the cold trap. This served to remove any remaining air from the system.

3.1.3: Data Acquisition and Control

The data acquisition and control system consists of two parts as shown in Figure 3.1.1. The temperature and power controllers are used to control the heat input to the heater block. The computer-aided data acquisition and control is used to record all pressures and temperatures and maintain the reservoir and preheat chamber at the set point temperatures.

The temperature controller shown in Figure 3.1.1 is programmable, uses a PID (proportional, integral and derivative) scheme, and performs a maximum of six cycles a second. The controller monitors the temperature of the upper thermocouple junction, maintaining it to within 1 °C of the set point by sending a 4 - 20 mAmp control signal to the Phase-Angle SCR power supply. The SCR power supply regulates the power to two of the quartz lamps by varying the phase angle on each ac cycle proportional to the control signal. Thus the power is varied between 0 and 1000 watts. A second ancillary variable transformer power supply is manually set to supply a base heat input of up to 500 watts to the third heater. If the temperature of the surface overshoots, as when the critical heat flux is surpassed, an alarm disconnects the power to all the heaters via relays. The power to the lamps along with the temperatures are continuously indicated by the panel meters.

The computer-aided data acquisition system features a high speed high resolution A/D converter, four input channels, and a six thermocouple isothermal input connector with cold junction compensation.

The thermocouple input connector uses channel one of the four input channels. The two pressure transducers which measure the nozzle and chamber pressures are read on channels two and three. Channel four was unused. The six inputs on the thermocouple input connector were connected to the two integral thermocouples in the heater block, the vapor space, the liquid reservoir, the preheat chamber, and the end of one of the heaters. All readings were monitored on screen continuously and recorded at 10-second intervals.

The readings for the two integral thermocouples are later corrected (As described in Appendix B) and used to calculate the heat flux and surface temperature. The vapor space temperature was monitored to ensure that the air was properly purged from the system. The temperature of the heater end was monitored to ensure that the air cooling was effective. If the heater ends get too hot, the heater may fail. The readings for the reservoir and preheat chamber were used for control as described below.

To control the temperatures in the reservoir and the preheat chamber, a zero or 5-volt signal, depending on whether the temperature is below or above the set point respectively, is sent to an appropriate pin on LPT1. The corresponding wires from the output cable are connected to the inputs of solid-state control relays. The relays are capable of switching up to 10 amps at 120 V. These relays are connected to the power leads for the immersion heaters in the reservoir and preheat chamber.

3.2: DROPLET DIAMETER AND VELOCITY MEASUREMENT

The droplet diameter and velocity distributions for the nozzles used in the experiments were measured so that the effects of the spray characteristics on the heat transfer could be identified. This section describes the new techniques and the results obtained.

3.2.1: Measurement Techniques

The measurements were conducted using a new technique which utilizes a digital video and image analysis system and laser sheet lighting. The technique is similar to that developed jointly by Cal Tech and the Jet Propulsion Laboratory [12]. The main difference is that they used a standard camera and a pulsed light source. The technique described here utilizes a special camera in which the shutter is triggered electronically. This allowed the use of a much less expensive argon ion laser for the light source. The camera resolution of the University of Kentucky system is also better than the Cal Tech/JPL system. This allowed more accurate determination of the droplet size and velocity.

The digital video camera used is manufactured by Xybion Electronics. The camera features electronic gating (shuttering) capability and an image intensifier with a gain of 25,000. The electronic gating was triggered using a custom designed logic control unit also designed by Xybion. The unit allowed the number of exposures to be adjusted between 1 and 9, and the time between exposures to be adjusted between 5 and 500 μ s. The time the shutter remained open was also adjustable between 10 ns and 10 ms. The extremely short exposure times were possible because of the high gain on the image intensifier. This allowed the droplets to be essentially frozen in the video frame.

To measure the droplet velocity, the number of exposures was set at 6 per video frame. The time between exposures was set at 20 μ s which was suitable for the droplet velocity range. The shutter speed was kept at 0.1 μ s to ensure that the droplets are essentially frozen during each exposure. The short exposure time and the small field of view (3mm x 3mm) limited the number of droplets present in each video frame. This is necessary to identify the trajectories of individual droplets.

After filming the spray for a few minutes at the desired nozzle operating conditions, the videometric image analysis system is used to calculate the droplet velocity. The time between exposures is accurately measured using an oscilloscope connected to a gate timing readout on the camera. This value is entered into the analysis software. The software is calibrated by filming a known measurement scale. The optical configuration used (200-mm lens with an expandable bellows) resulted in a horizontal and vertical resolution of 8.5 and 10.0 μm per pixel, respectively. The uncertainty in the resolution is estimated to be less than 0.5 μm (See Appendix A). The software is then used to input the positions of the droplets shown in a given trajectory (multiple exposures of the same droplet). The droplet velocity is then automatically calculated.

The size of the droplet is calculated by defining an area which encloses a given droplet. A pixel intensity histogram is then conducted for the region defined. The histogram gives the number of pixels contained in the droplet area. The area of each pixel, determined from the calibration, is then multiplied by the number of pixels contained in the droplet to give the droplet cross-sectional area. This is then recorded and used to calculate the diameter. In this manner simultaneous measurements of the droplet diameter and velocity are taken. To calculate an area average diameter, the region is defined around a number of droplets. The uncertainty in the droplet diameter results from light scattering. To be conservative, the diameter is assumed to be accurate to within 2 pixels, or approximately 20 μm .

3.2.2: Measurement Results

The results of the droplet diameter and velocity measurements obtained by the techniques previously described are presented in this section. The measurements are then used to help explain the observed critical heat flux phenomena.

The accuracy of the droplet diameter measurements was verified by comparing the droplet diameter distribution to the previous laser phase doppler analysis (described in Chapter 2) of the same nozzle operating at the same pressure.

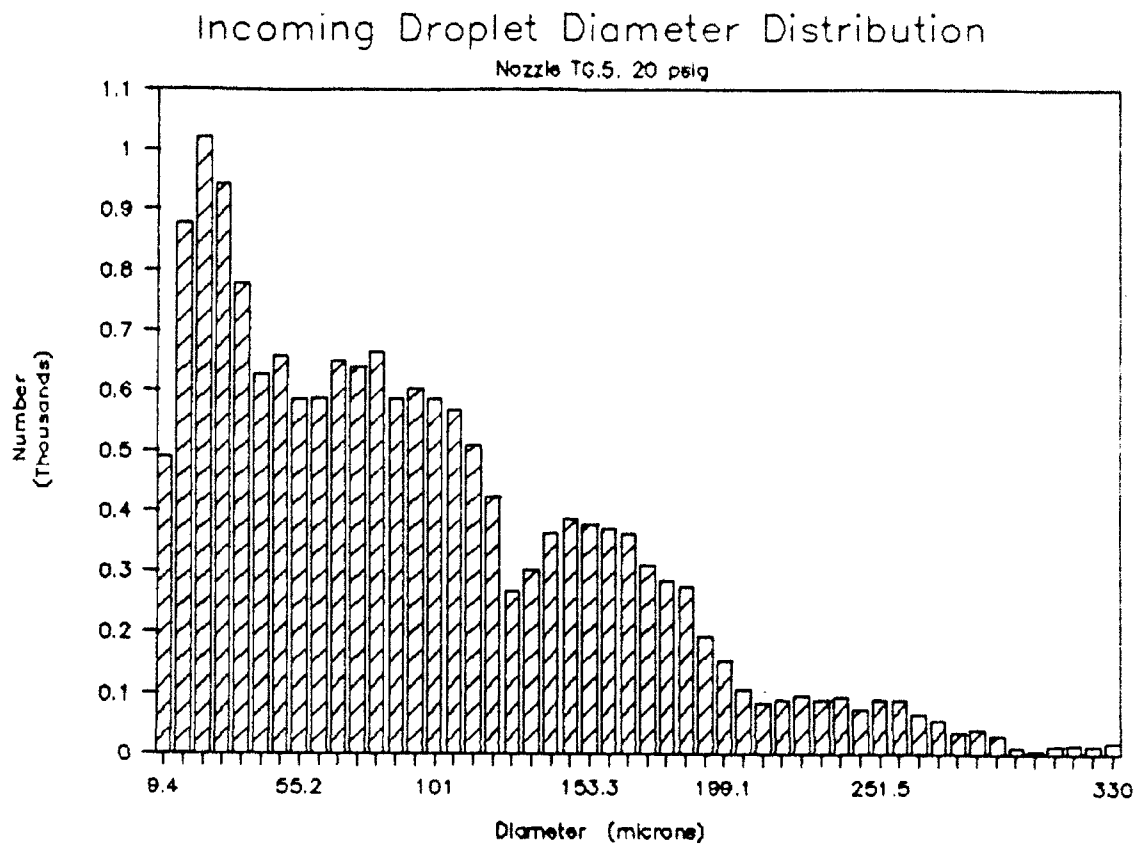


Figure 3.2.1: Droplet diameter distribution, PDPA measurement

Figure 3.2.1 is a stacked-bar graph showing the droplet diameter distribution at different radial positions within the spray for nozzle TG.5 operating at 20 psig. The distributions are based on 5,000 samples at each radial location given. Figure 3.2.2 is the droplet diameter distribution measured using the digital video and image analysis system with the technique described in Section 3.2.1. Even though the largest number of droplets have diameters less than 100 μm , Figure 3.3 indicates that these droplets do not contribute greatly to the overall volume flow rate. Also, these small diameter droplets become easily entrained in the escaping vapor and do not provide effective heat transfer, as shown in Figure 2.3.3. For this reason, it was decided that the digital video measurements should concentrate on droplets greater than 100 μm in size. A comparison of the distributions given by

the two techniques exhibits the same trends. Both show a minimum occurring at 120 μm . The maximum occurs at about 140 μm and then the number density trails off and flattens out at about 200 μm . The distribution is flat until about 250 μm and then it decreases further. The digital video measurements do not reflect the larger diameter measurements because of the very low probability and the small number of samples taken. This comparison indicates that the technique provides relatively accurate measurement capability.

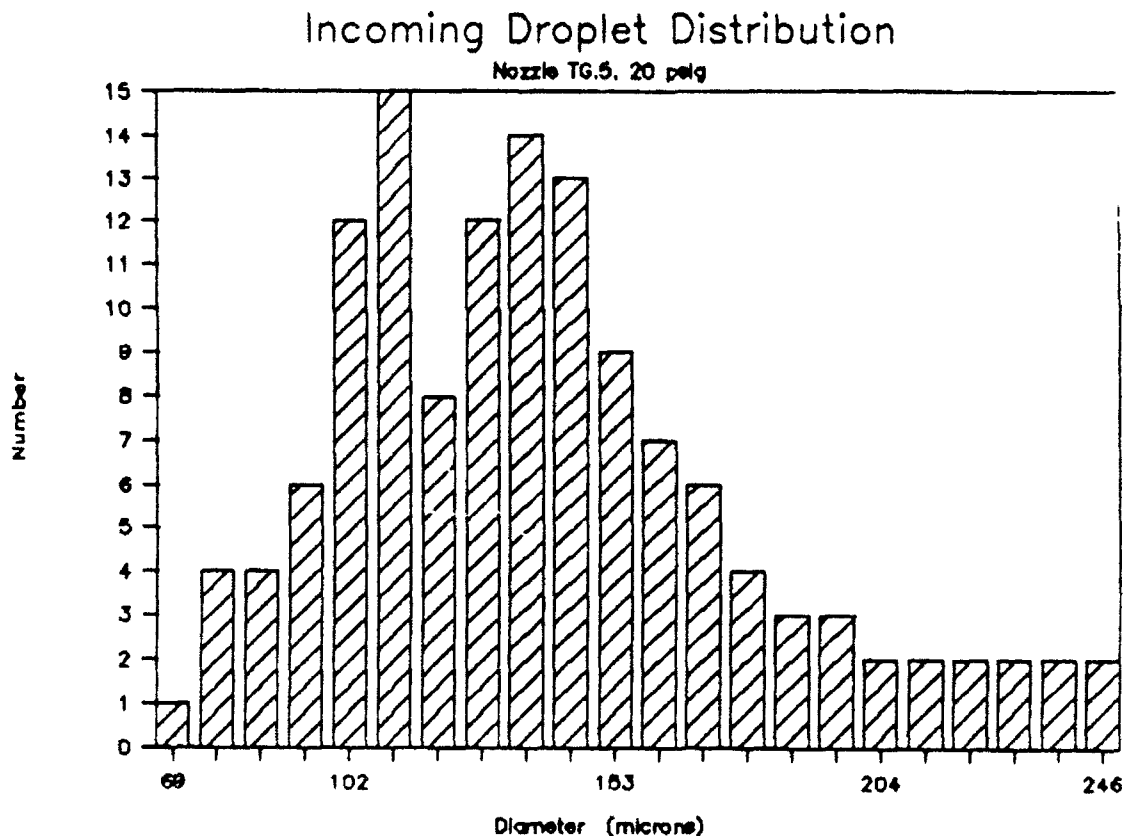


Figure 3.2.2: Droplet diameter distribution, digital video measurement

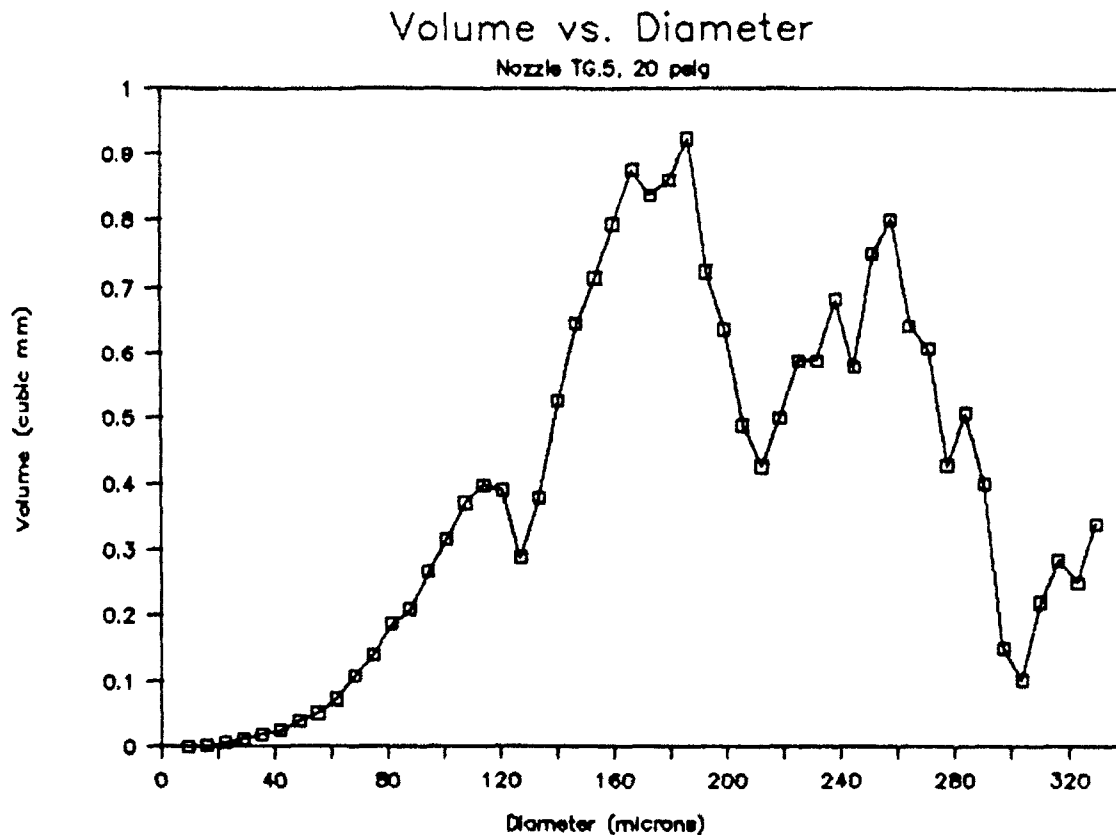


Figure 3.2.3: Volume vs. diameter

Figure 3.2.4 shows the velocity distribution for the same nozzle. The distributions for all the nozzles were the same shape, with the maximum standard deviation less than 2.0 m/s. The simultaneous droplet diameter and velocity measurements indicated that the velocity did not vary greatly with droplet diameter. However, as vapor generation increases with heat flux, the smaller droplets decelerate rapidly. The laser phase Doppler measurements of the velocity (not shown) have the same profile but have lower values. This is because the measurements were taken further from the nozzle exit. The error associated with the digital video measurements is maximum at the lowest velocity. However, the maximum error is less than 10 percent based on the assumption that the time between exposures is accurate to within 1 μ s, and the distance between images of the same droplet in a trajectory is accurate to within

± 2 pixels ($20 \mu\text{m}$).

Table 3.1 gives the area averaged droplet diameter and velocity for the nozzles used in the experiments as a function of the flow rate. The average velocity is based on a minimum of 20 measurements. The diameter given is an area averaged diameter of over 100 droplets.

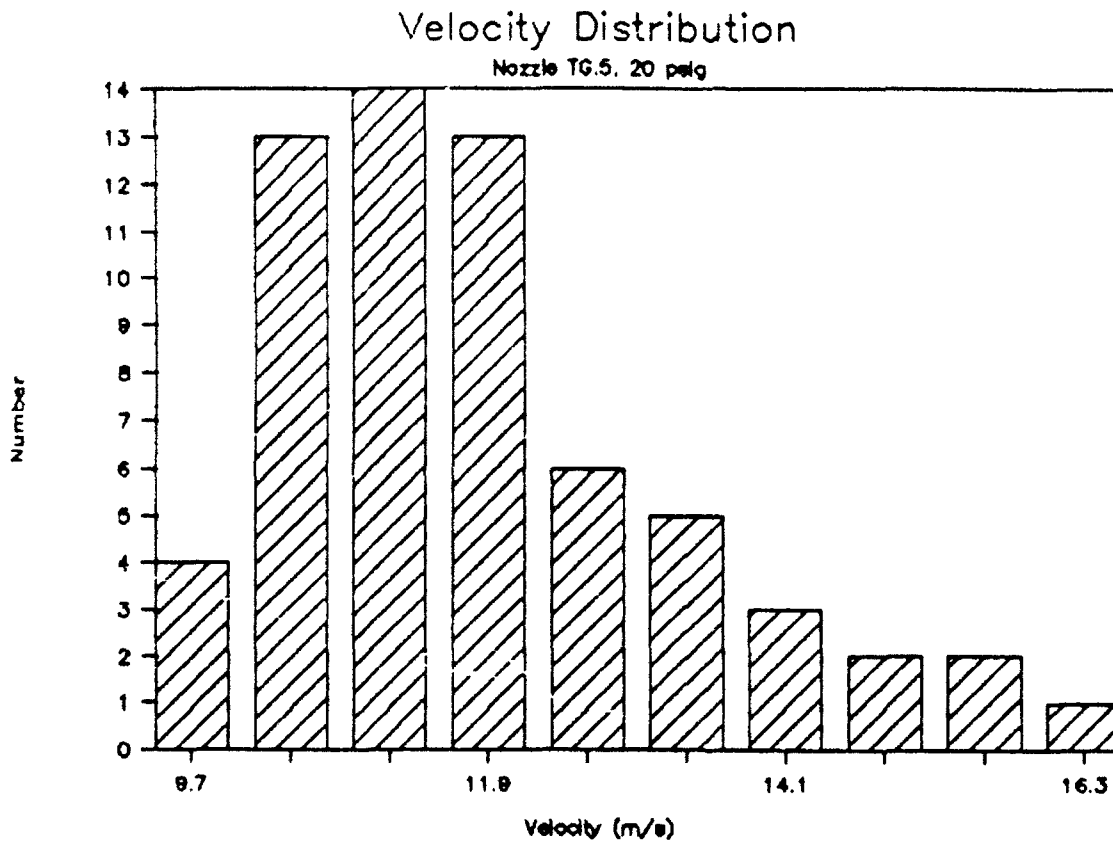


Figure 3.2.4: Velocity distribution

Table 3.1: Droplet diameter and velocity measurement results

Orifice Dia. (mm)	Flow rate cc/s	Diameter μm	Velocity m/s
0.51	4.5	123.5	14.4
	5.2	122.6	16.9
	6.7	118.0	20.2
0.61	5.2	126.9	12.0
	5.9	126.7	12.9
	6.7	125.5	13.4
0.69	5.2	132.1	10.5
	5.9	130.5	10.8
	6.7	129.4	11.2
0.76	5.2	136.0	8.7
	5.9	135.8	9.3
	6.7	134.7	10.0

The apparatus described in this chapter was used to obtain the experimental results presented next in Chapter 4. The diameter and velocity measurements described provide useful insight for the analysis of the results. They are also useful as an analysis tool for the phenomenological modeling presented in Chapter 5.

CHAPTER 4: EXPERIMENTAL RESULTS

In this chapter, the experimental results obtained with the new apparatus described in Chapter 3 are presented. The chapter consists of an introduction, a description of the experimental procedure, and the experimental results. The in-depth analysis and phenomenological modeling of the results are presented in Chapter 5. The results are compared to those of previous researchers in Chapter 7. The uncertainty analysis for all the experimental measurements is presented in Appendix A.

4.1: INTRODUCTION

The apparatus described in the previous chapter was used to perform extensive testing. The goal of the experiments was to develop a fundamental understanding of spray cooling heat transfer. To obtain this understanding, it is necessary to determine how the spray characteristics affect the heat transfer results. Tests were conducted with a very smooth surface in a single-component, closed-system. Therefore, the effects of the spray characteristics could be isolated from the effects of fluid subcooling, noncondensable gas, and the surface roughness conditions.

The spray characteristics were varied by changing the nozzle orifice diameter and flow rate. The average droplet diameter and velocity were measured for most of the cases as described in Chapter 3. The measurement results are given in Table 3.1. This information is used to draw preliminary conclusions. Additional experimentation and modeling are presented in Chapter 5 to provide more detail and further substantiate these conclusions.

Experiments were also conducted to determine the individual effects of subcooling, noncondensable gases, and surface roughness conditions. The results of these experiments are also presented in this section.

4.2: EXPERIMENTAL PROCEDURE

The procedures presented in this section refer to the tests conducted with the apparatus described in Chapter 3. As mentioned, the surface was polished to a mirror finish prior to testing. To do this, the surface was first sanded with progressively finer grit papers. Then, alumina polishing powders of 1.0 and 0.3 μm were used to complete the polishing. Between individual runs, the surface was not cleaned or polished in any way. Although some oxidation occurred, the results were repeatable over a long period of time, as presented later. Therefore, the variation in the results is caused by variation in spray characteristics rather than any changes in the surface or environmental conditions.

The experiments were all conducted according to the following procedure. Prior to each test the desired nozzle was installed. Next, the test chamber was heated to the saturation temperature. The air was then purged from the system as described in Section 3.1.2.

After the entire system was purged, the desired nozzle flow rate was set using the micrometer dial on the diaphragm pump. To obtain flow with sufficient momentum, the flow rate was only varied between 60 and 100 percent of the maximum pump capacity. Since the pump is a positive displacement metering pump, the flow rate was nearly the same for each micrometer position regardless of the nozzle orifice size. This allowed comparison of the heat transfer results obtained using different nozzles at the same flow rate. The actual flow rates were measured as a function of nozzle orifice size for each micrometer position. The measurements were taken using a graduated cylinder and a stop watch. Table 4.1 gives the volumetric flow rate in cc/s averaged over five runs for the different nozzle orifice sizes at the various micrometer positions used in the experiments. The uncertainty associated with the measurement technique is estimated to be approximately 0.1 cc/s. However, pump fluctuations during the actual experiments may increase the uncertainty slightly. The nozzles used for the experiments were Spraying Systems Company nozzles TG.3 through TG.7 (Lower number means smaller orifice diameter).

Table 4.1: Nozzle Volumetric Flow Rates (cc/s)

Micrometer Position	Nozzle Orifice Diameter (mm)					Average
	0.51 TG.3	0.56 TG.4	0.61 TG.5	0.69 TG.6	0.76 TG.7	
60 %	4.33	4.56	4.44	4.49	—	4.45
70 %	5.16	5.25	5.14	5.21	5.27	5.21
80 %	5.93	5.75	6.01	5.93	6.07	5.94
90 %	6.65	6.36	6.72	6.66	6.79	6.74
100 %	7.33	7.32	7.45	7.46	7.50	7.41

After setting the flow rate, the set point on the temperature controller was programmed to the desired surface temperature. The auxiliary heater power level was also set using a rheostat. As the heater block and test surface temperature went up, the power to the heaters was continually adjusted to maintain the surface temperature at the set point. The set point was indexed as desired until the CHF was identified. The apparatus was then cooled down again and the flow parameters were adjusted for a new test.

The data acquisition system recorded all the important data as the heat flux to the surface was increased. The resulting data file was input into a computer program which corrected the thermocouple temperature readings as described in Appendix B and calculated the surface temperature and heat flux. This file was then used to plot the heat flux versus surface temperature curves which are shown in Section 4.3 and Appendix C.

4.3: TEST RESULTS

Over 200 experiments were performed with the new apparatus. Three different types of nozzles were investigated. However, only one type of nozzle proved to be suitable for spray cooling. The other nozzles did not provide a uniform spray distribution and consequently, CHF and efficiency were both very low. This section presents the results obtained with the best spray nozzles. Even these nozzles showed nonuniformity in the spray cone which adversely affects the heat transfer results, and makes analysis difficult. The uniformity

of the spray cone is of utmost importance to obtaining high efficiency and high critical heat flux. A set of test results for the saturated, single-component, closed-system tests with the mirror finish surface are presented in Appendix C, Figures C.3.1 through C.3.5. The results cover the entire operating range of the available nozzles over the range of the pump capability. For these tests, the nozzles and flow rates presented in Table 4.1 apply. Specific cases will be presented in this section to illustrate the various effects of the spray conditions.

Regardless of the nozzle orifice size, it is apparent that both the critical heat flux and the heat transfer coefficient increase with increasing volumetric flow rate. The best example of this is presented in Figure 4.3.1 plotted for nozzle TG.5. In this case, when the flow rate is increased from 60 percent of maximum to the maximum, the heat transfer coefficient is increased by 24 percent and the critical heat flux is increased by 21 percent.

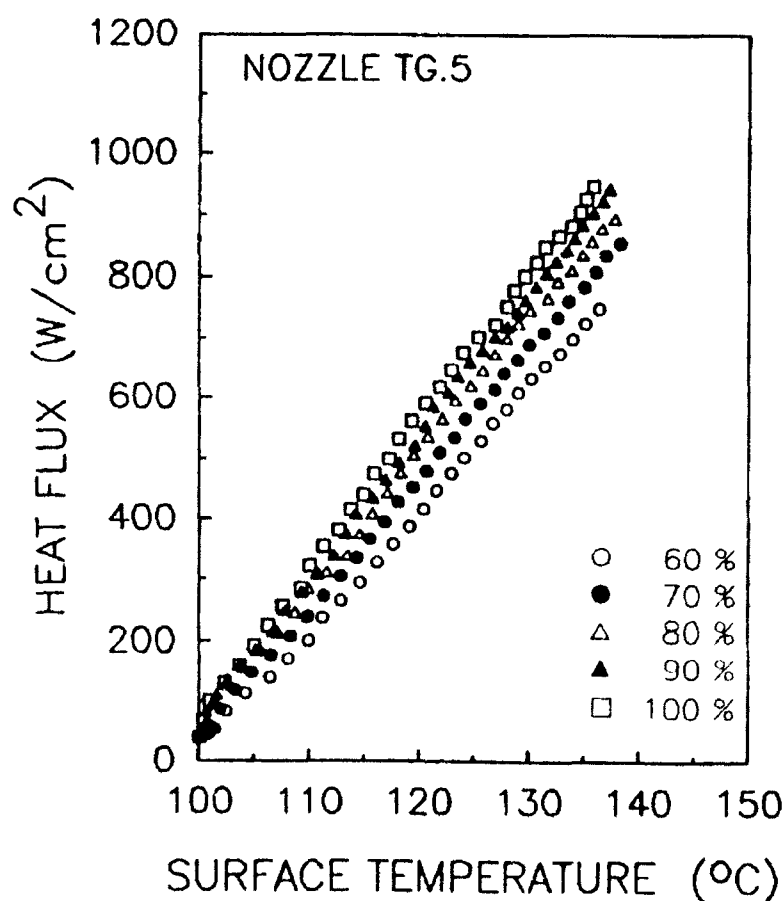


Figure 4.3.1: Effects of flow rate, nozzle TG.5

However, not all nozzles demonstrate the same degree of improvement because the changes in flow rate have different effects on the spray characteristics. Figure 4.3.2 shows that for nozzle TG.7, the heat transfer coefficient hardly changes even though the CHF shows comparable improvement. This is best explained by describing the fundamental heat transfer mechanisms.

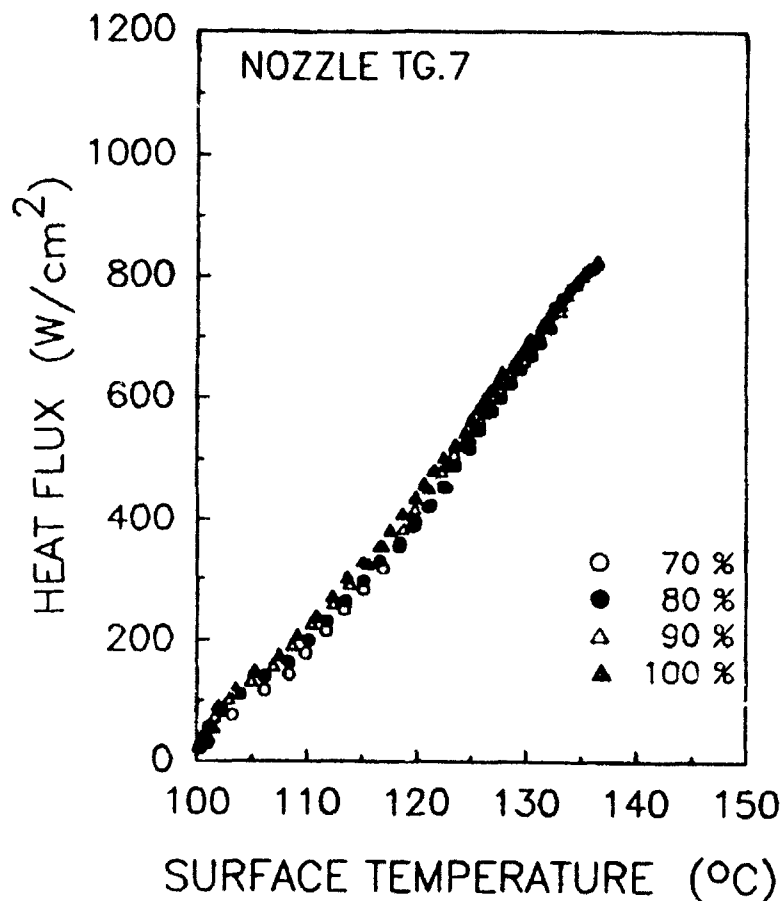


Figure 4.3.2: Effects of flow rate, nozzle TG.7

Recall from the introduction that three mechanisms for critical heat flux transition were postulated depending on the flow rate. The very low flow rate dropwise evaporation cases are discussed in Chapter 6. The low flow rate flooded surface cases were discussed in Chapter 3. The closed-system tests correspond to the high flow rate mechanism. For these cases, the CHF occurs when the vapor generation rate on the

surface becomes so high that a vapor blanket forms in a given region in the time interval between droplets impinging in that region. The higher the impingement frequency, the shorter the time between droplet impingement. The impingement frequency is directly proportional to the flow rate and inversely proportional to the cube of the average droplet diameter. Since the average droplet diameter decreases with increasing flow rate for a given orifice size (See Table 3.1), the impingement frequency always increases with increasing flow rate. It is also evident from Table 3.1 that the change in droplet diameter does not vary significantly from nozzle to nozzle. Hence, one would expect all nozzles to show comparable increases in impingement frequency with increasing flow rate. Therefore, one would also expect comparable improvement in CHF. The reason that the improvement is not always the same for different nozzles is that the liquid film thickness, and the spray cone angle and uniformity also change with increasing heat flux. For example, some nozzles become hollow in the center as the flow rate is increased. This diminishes the impingement frequency in the center leading to early transition to critical heat flux. Also, with some nozzles, the liquid film thickness increases by a greater amount as the flow rate is increased. The liquid film thickness affects the region of influence of each impinging droplet. As the liquid film thickness increases, higher droplet momentum is required to destroy the growing vapor bubbles to suppress transition to a nonwetting surface condition.

The heat transfer coefficient for these cases is dictated by the very complex heat transfer within the liquid film. Heat is transferred by bubble nucleation, as well as evaporation from the upper liquid/vapor interface. The amount of heat transferred by nucleation is dependent on the surface roughness conditions and the surface temperature. Since the surface roughness does not change from test to test, a comparison of the heat transfer at one given temperature should isolate the contribution of the effects of nucleation. Therefore, the changes noted in heat transfer coefficient are due to changes in how efficiently heat is transferred from the surface to the upper liquid/vapor interface where evaporation is occurring. Estimations of the film thickness indicate that straight conduction heat transfer cannot account for the high heat fluxes observed. This indicates that impingement phenomena dominate

the heat transfer within the liquid film. Consider Figure 4.3.3. There exists a very thin layer of fluid (microlayer) next to the surface which is superheated by conduction from the surface. As a droplet impinges, its high momentum forces fluid out from underneath it. This creates a situation in which the hot fluid from the superheated layer is mixed with the bulk of the liquid film. When the superheated fluid comes near the liquid/vapor interface, evaporation occurs.

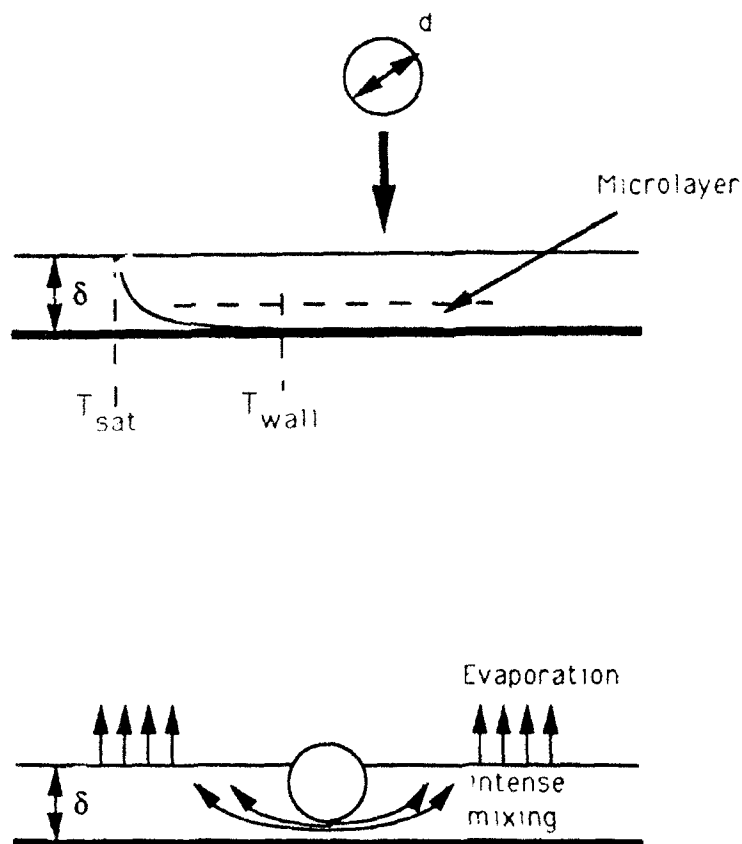


Figure 4.3.3: Impingement induced mixing

Therefore, one would again expect that the heat transfer coefficient would increase with increasing mass flow rate since the mixing is enhanced by the higher impingement frequency. However, as the mass flow rate is increased, the film thickness, δ , also increases. Therefore, the droplets must have greater momentum to provide the same

mixing. Referring again to Table 3.1, it is evident that with the larger orifice diameter nozzles, the droplet momentum does not increase as much with increasing flow rate as it does for the smaller orifice diameter nozzles. In addition, the film thickness likely increases more. Therefore, nozzles which have a large increase in droplet momentum in comparison to the increase in film thickness will show more improvement in heat transfer efficiency. This explains why Figure 4.3.1 demonstrates marked improvement in efficiency while Figure 4.3.2 does not. Again, it should be mentioned that the uniformity of the spray cone plays a key role. If the spray cone is hollow in the center, the film thickness increases at a spot where the impingement frequency is low. This reduces the heat transfer efficiency in this portion of the surface.

Figure 4.3.4 shows the results for all the nozzles operating at the maximum pump flow rate. As seen, even though the flow rate is the same, the efficiency and the critical heat flux vary significantly. As the orifice diameter is increased, the impingement frequency and momentum are reduced. The lower impingement frequency would indicate that the CHF should be lower. This trend is supported by the data except for nozzles TG.4 and TG.6. Both of these nozzles exhibited a narrow spray cone which was hollow in the center. This caused early transition to critical heat flux. In fact with nozzle TG.4, a stable nonwetting region was observed to form in the very center of the spray. The data showed that this caused the average surface temperature to jump by 6 °C. Then as the heat flux was increased a little more, the whole surface became nonwetting. The other three nozzles had wider spray cones, but nozzle TG.3 was also somewhat hollow in the center. When the uniformity of the spray cone is considered, the data are still explainable by the theories described.

As mentioned, the larger the orifice diameter, the lower the average droplet momentum. Since the flow rate is the same, one would expect the liquid film thickness to increase with decreasing momentum. Also, since the impingement frequency decreases, less mixing would occur. Therefore, one would also expect the efficiency to decrease with increasing orifice diameter. This trend is exhibited except for nozzle TG.5. This nozzle unexpectedly demonstrates the highest efficiency.

However, observations indicated that the spray cone for this nozzle was the most uniform out of all the nozzles. Therefore, these results are not surprising and again emphasize the extreme importance of spray cone uniformity.

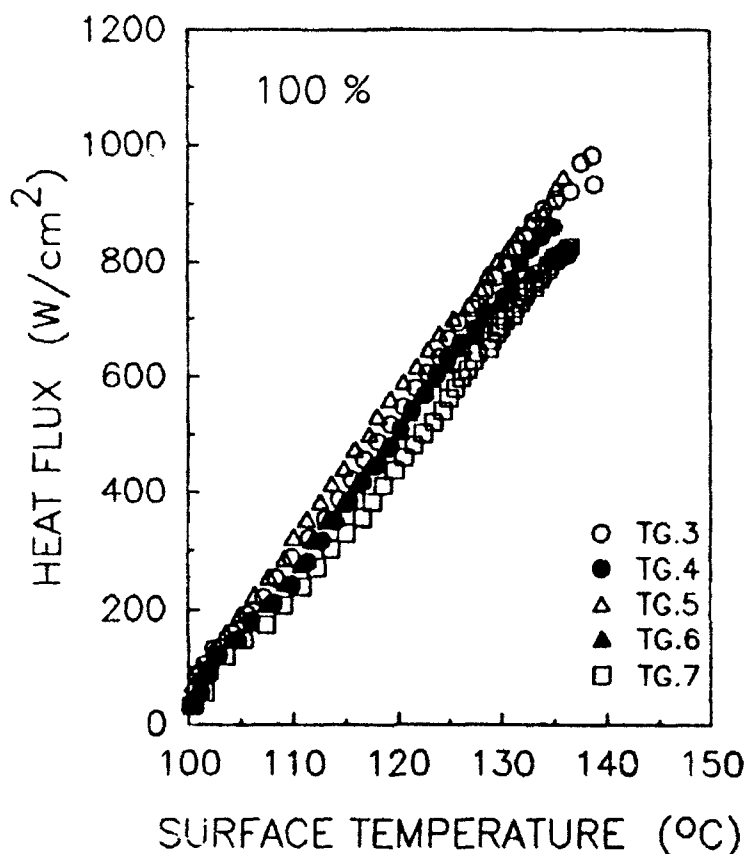


Figure 4.3.4: Effects of orifice diameter, maximum flow rate

If the above theories concerning the mechanism for critical heat flux are correct, the data should collapse when the CHF is plotted against the impingement frequency. However, since the spray cone is not uniform there is significant scatter. To try to reduce the scatter, the spray cone for each nozzle at each operating flow rate was viewed by illuminating its cross section with a laser sheet light. A factor, χ , was defined which is simply a visual judgment of the uniformity of the spray cone. It is calculated as the ratio of the area of high intensity laser light to the total surface area. The laser light only appears to have high intensity in sections of the spray where the volume flux (impingement frequency) is high. Figure 4.3.5 shows the critical heat flux for all the data plotted against the product of the impingement

frequency, \bar{n} , and the uniformity factor, χ . The curve shows that the phenomena are reasonably approximated. There is still significant scatter in the data. This is partially due to the method for estimating χ . When the spray cone is hollow, the area of high intensity is still nearly equal to the surface area. However, the small hollow region may burn out causing early transition to critical heat flux. Therefore, the CHF is lower than expected. Also when the spray cone is narrow, χ is very small. However, a narrow spray cone does not affect the heat transfer as adversely as a hollow cone, since fluid flows radially outward on the surface. Therefore, the CHF is higher than predicted by the theory. A more accurate curve could be plotted if the impingement frequency could be accurately measured as a function of radial position within the spray cone. Even with the inaccuracy in the method of determining the proper factor on the x-axis, the critical heat flux is predicted by the solid line to within 50 W/cm^2 with 95 percent confidence.

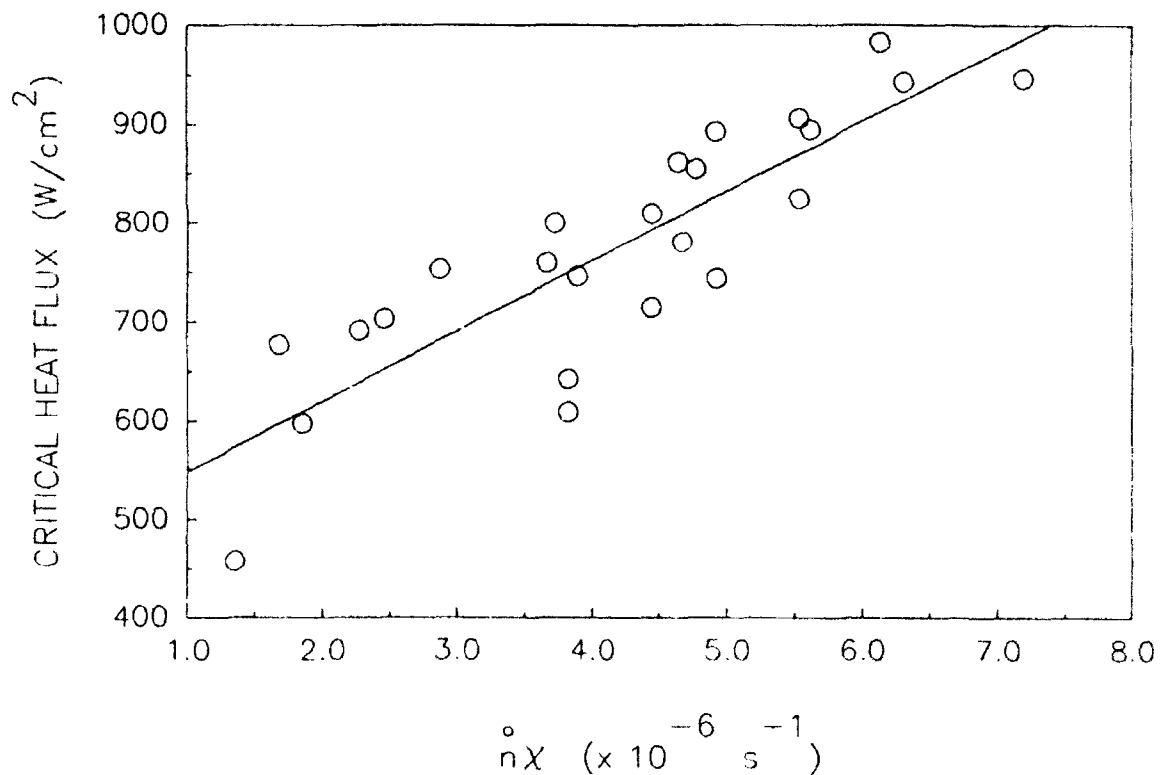


Figure 4.3.5: CHF vs. impingement frequency

More detailed analysis and additional experimentation were conducted to verify the above conclusions. This is presented in Chapter 5.

After completing the tests with the saturated fluid in a single-component, closed-system additional experimentation was conducted to determine other important factors. It must be shown that the data are repeatable over a long period of time. Otherwise, some of the differences observed in the experimental results presented above could be attributed to changes in the surface characteristics. To ensure that this was not the case, the first tests conducted immediately after polishing the surface were repeated after all of the other tests were run. The result is shown in Figure 4.3.6. As indicated in the figure, the data were very repeatable over the testing period. Even though the critical heat flux was surpassed 25 times in between the tests conducted, and the surface showed evidence of oxidation, there was no significant change in the results. Therefore, the surface conditions do not play a role in the variation in results. However, if testing continued for a much longer time period, the continual burnout may eventually cause degradation which would change the surface wetting and nucleation characteristics. In fact, previous tests conducted in air with the preliminary apparatus did show variation over time. The higher thermal mass of the apparatus caused the surface temperature excursion to be 200 °C greater than with the closed-system apparatus. Also, in the closed-system test, since the air was purged from the system, the oxidation problem is less severe.

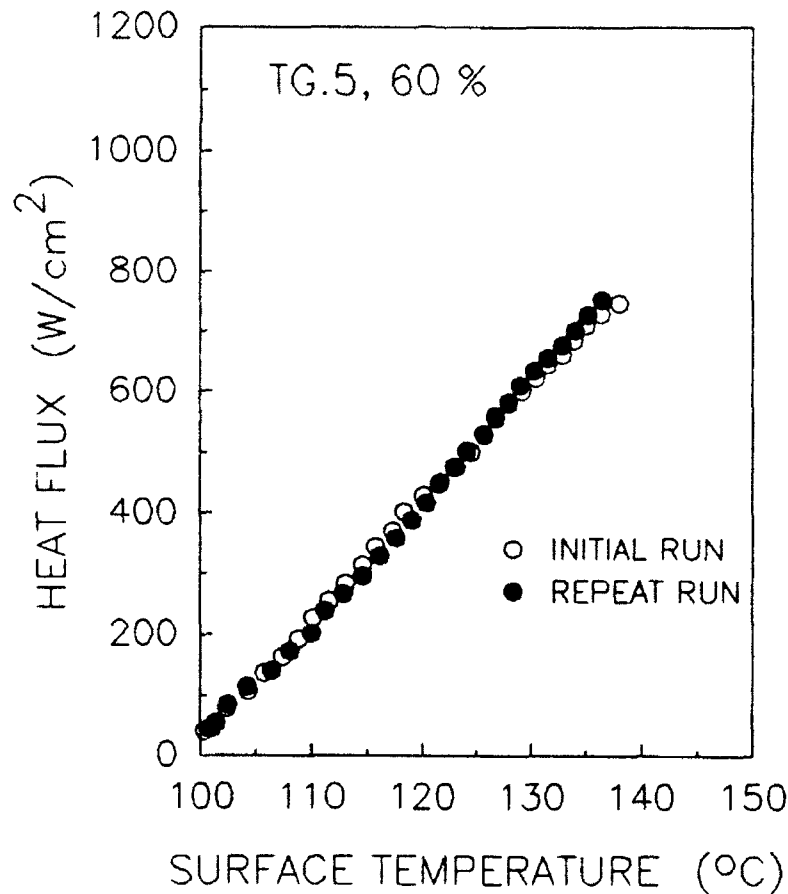


Figure 4.3.6: Data repeatability

The above tests served to isolate the effects of changes in the spray characteristics. There were no changes in the environment, surface conditions, or test procedures. This allowed easier analysis of the data because the effects of several important parameters could be eliminated. The next step is to determine the effects of those other important parameters, including noncondensable gases, liquid subcooling, and surface roughness.

To determine the effects of noncondensable gases, the liquid was heated to the saturation temperature, but the air was not purged. Consequently, the partial pressure of the vapor in the system was less than 1 atmosphere. Thus, evaporation and condensation occurred at a lower saturation temperature. Since fluid is evaporating from the upper liquid/vapor interface, air is swept away. Therefore, the partial

pressure is nearly 1 atmosphere right at the liquid/vapor interface. The results indicated that the heat transfer was essentially the same, except that the surface temperature at any given heat flux was approximately 1 °C lower for the tests with air present. This is shown in Figure 4.3.7. From this, it is evident that the noncondensable gases have little effect on the evaporation heat transfer. However, it was observed that the gases severely hampered the condensation within the system. Not only was the temperature at which condensation occurred significantly lower (approximately 5 - 10 °C), but the condensation heat transfer coefficient is also reduced due to binary diffusion. Therefore, it is apparent that for effective closed-system operation, it is necessary to remove all noncondensable gases.

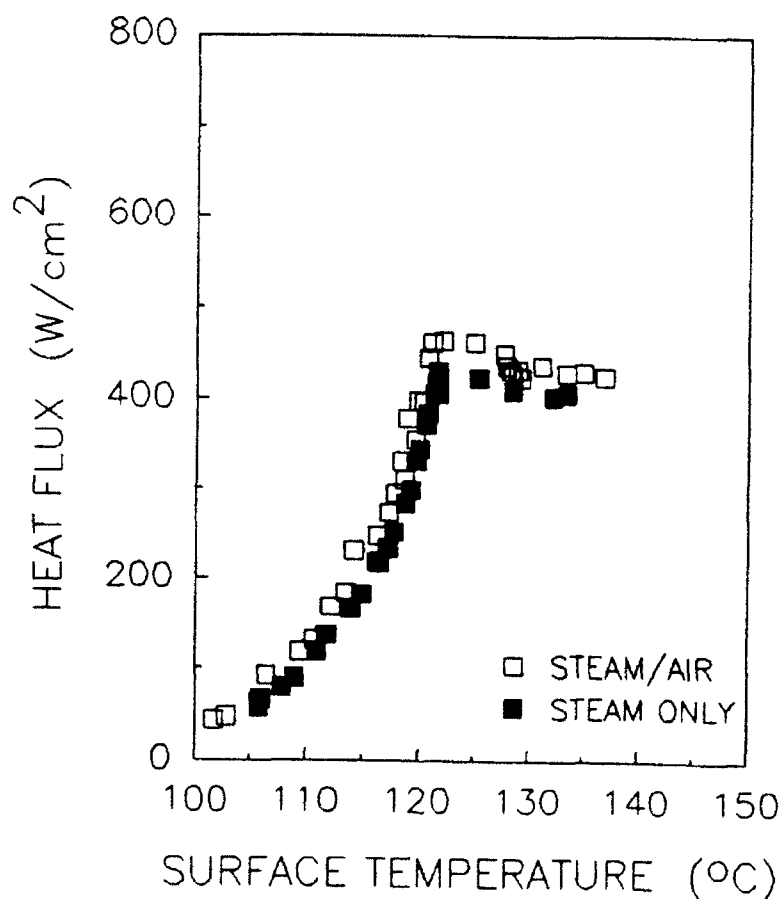


Figure 4.3.7: Effects of noncondensable gases

Figure 4.3.8 is plotted to show the effects of liquid subcooling. These tests were conducted in an open system with the same nozzle operating conditions and surface conditions. The liquid subcooling provides a much greater heat flux at low superheat. At a surface temperature of 100 °C very little evaporation occurs. Therefore, forced convection to the subcooled fluid is responsible for the excess heat removal seen. Notice too, that these curves have the same shape as the subcooled liquid tests presented in Chapter 2. The changes in slope indicate that the same mechanisms for heat removal are important. As the surface temperature increases, the percentage of heat removed by evaporation increases. Comparing the subcooled cases to the saturated case indicates that the degree of improvement in heat flux decreases as the surface temperature goes up. This is thought to be due to the fact that the subcooling suppresses the mechanism of evaporation from the upper liquid/vapor interface, which is a significant heat transfer mechanism in cases with saturated fluid. Also, the shape of the temperature profile of the superheated layer changes due to the fluid subcooling. Thus, a higher superheat is required to activate the same number of nucleation sites. Also, the bubble growth rates may be reduced.

If the heat transfer coefficient is independent of the difference between the fluid temperature and the surface temperature, the data indicate that as much as 60 percent of the heat could be removed solely by forced convection for the 50 °C subcooling case. For the 25 °C subcooling case, 45 percent could be removed through sensible heat. However, as seen in Chapter 2, a large percentage of the flow rate may be expelled by nucleating bubbles. This also diminishes the effects of liquid subcooling.

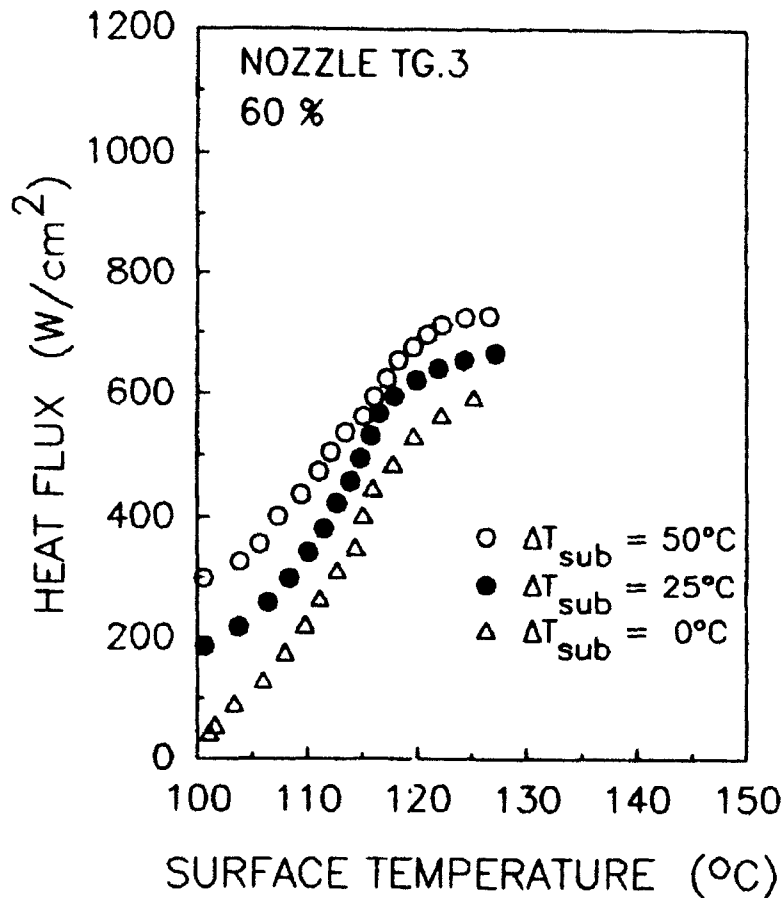


Figure 4.3.8: Effects of liquid subcooling

The effects of surface roughness were investigated by comparing the results for a surface polished to mirror finish as previously described, with the results of a surface sanded with 400 grit paper. The comparison is presented in Figure 4.3.9. As seen in the figure, the critical heat flux for the smooth surface is significantly higher than it is for the rough surface with all else remaining the same. Also, the heat transfer coefficient for the rough surface is slightly better than for the smooth surface. This figure provides further support for the theory that the CHF results when the vapor generation rate at the surface becomes too high. Since the rougher surface provides a greater number of nucleation sites at a given surface temperature, the vapor generation rate should be higher. Therefore, it is expected that the CHF should occur at a lower temperature. The efficiency is improved for

the rough surface because nucleation is much more efficient due to microlayer evaporation. Analysis of these results will be presented in greater detail in the following section.

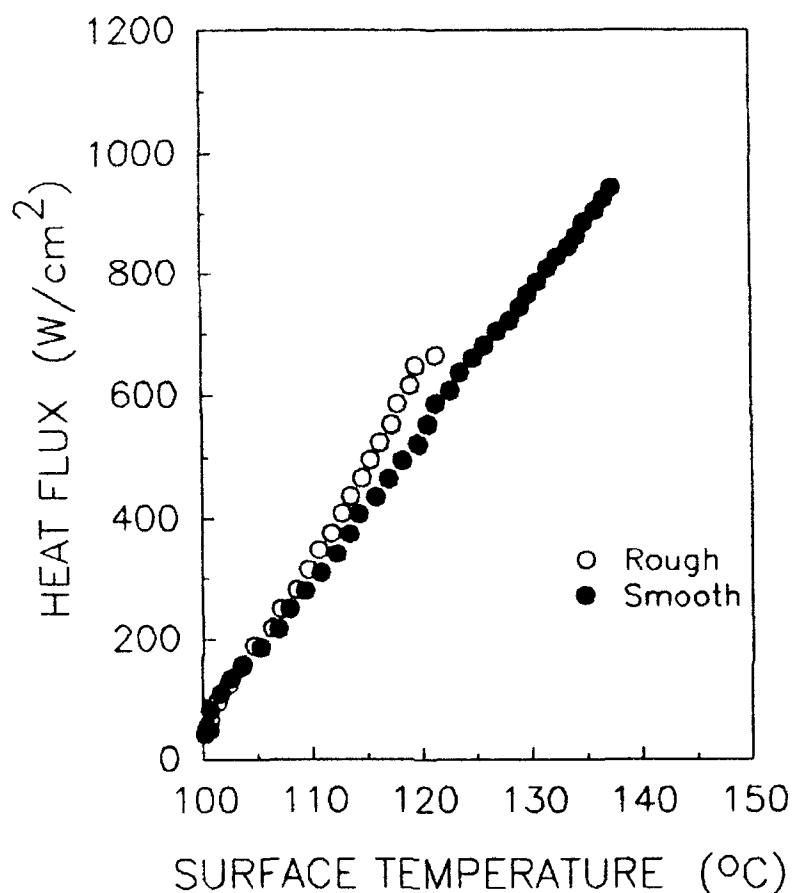


Figure 4.3.9: Effects of surface roughness

The experimental results have indicated that the spray characteristics exert a strong influence on the heat transfer results. At a constant flow rate, the heat transfer coefficient is seen to vary by as much as 15 percent with changes in the spray conditions. The critical heat flux is seen to change by as much as 300 W/cm^2 . For the same spray conditions, changes in surface conditions also greatly change the heat transfer. The CHF is as much as 300 W/cm^2 lower when the surface is rough. More detailed analysis of the reasons for the differences is presented in the following chapter.

CHAPTER 5: PHENOMENOLOGICAL MODELING AND ANALYSIS

In this section phenomenological modeling is presented to describe the physical phenomena associated with high-heat-flux spray cooling so that a more fundamental understanding can be obtained. Additional experiments were performed to provide more detailed data to aid in the analysis. These experiments are described in conjunction with the modeling they pertain to. The goal of the modeling is not to provide a predictive tool, but to explain the trends observed in the experiments and more accurately describe the important factors governing spray cooling heat transfer. A predictive model is not possible with the present knowledge because the phenomena are too complex and uncertainty in many important parameters is high. There are many factors for which it is impossible to determine governing analytical relationships at this point.

The modeling and analysis are divided into two parts, one concerning the effects of the spray characteristics, and one concerning the effects of the surface conditions. Then, an explanation is provided to describe how these two parts interact with each other, and the resulting effects on the critical heat flux and the heat transfer coefficient.

To determine the effects of the spray characteristics, the following questions must be answered:

1. What are the droplet diameter, velocity, and volume flux distributions resulting from a given flow rate and nozzle orifice size?
2. What percentage of the impinging spray is splashed from the surface, and what is the resulting liquid film thickness?
3. How do the impinging droplets interact with the liquid film? How do the impinging droplets affect the heat transfer in areas, such as mixing, secondary nucleation, nucleation frequency, etc.?

To determine the effects of the surface conditions, the following questions must be answered:

1. How does the surface roughness and the surface temperature relate to the number of active nucleation sites on the surface?
2. What are the bubble growth rates? How much heat is removed through bubble nucleation at the surface?
3. What is the mechanism by which vapor bubbles break, and how do the bubbles interact with the liquid film?

Finally, the relationships between the above factors must be defined so that the spray cooling process may be well understood. For example, bubble generation frequency in pool boiling has been extensively researched, but the flow situation is much simpler. The bubble departure frequency is controlled by a balance of the various forces on the vapor bubble. However, in spray cooling, the droplet impingement will affect the bubble lifetime, since the droplets have high enough momentum to break the bubbles and displace the vapor. This is one example of the difficulty in modeling such a complex phenomenon. The interaction between the impinging droplets and the nucleating bubbles makes it difficult to isolate various important effects.

5.1: EFFECTS OF SPRAY CONDITIONS

In this section, the effects of the spray conditions are analyzed and modeled so that the heat transfer may be better understood. Recall from Chapters 2 and 3 that two different methods were used to provide information concerning the spray characteristics. In Chapter 2, a description of the laser phase Doppler system measurements was given. These measurements were very detailed, but were conducted for a much lower range of flow rate, and are not generally applicable to the experimental cases presented in Chapter 4. It was not possible,

unfortunately, to repeat these measurements during the closed-system, high flux testing because the system was no longer available.

Therefore, new measurement techniques were developed. These are described in Chapter 3. The new techniques have many limitations and cannot provide the same amount of information and detail as a laser phase Doppler system. The techniques were also very time consuming. However, useful information is provided which will be discussed here.

Recall that the results of the droplet diameter and velocity measurements were presented in Table 3.1. These measurements cover the majority of the nozzles and flow rates used in the experiments presented in Chapter 4. The average droplet diameter and velocity for the cases not measured can be estimated by interpolating from the table, since the trends are well defined. For a given flow rate, as the orifice size is decreased, the droplet velocity increases and the droplet diameter decreases. The trends in the droplet diameter measurements, although anticipated, are probably attributable more to coincidence than the accuracy of the measurement technique. The velocity measurements are fairly accurate (See Appendix A). Despite the limitations in the data, useful information can still be obtained.

For example, one of the most important factors is the droplet impingement frequency. The impingement frequency has a profound effect on the efficiency because droplet impingement enhances mixing as discussed in Chapter 4, in relation to Figure 4.3.3. The impinging droplets also destroy nucleating bubbles and expel the vapor, thus preventing the formation of a vapor barrier. Therefore, the impingement frequency also has a profound effect on the critical heat flux. In order to calculate the impingement frequency, the average droplet diameter must be known:

$$\bar{n} = \frac{6Q}{\pi d^3} \quad (5.1.1)$$

Ideally, a complete distribution of the droplet diameters should be used to sum the droplet volume. This is because the area average diameter (presented in Table 3.1) skews the average towards larger droplets. Even though the much smaller droplets do not contribute significantly to

the volume flow rate, their interaction with the nucleating bubbles and the mixing with the liquid film is still important. Even though there is high uncertainty in the impingement frequency calculation (approximately 50 percent), this method provides useful insight and can be used for comparison.

The droplet velocity is also very important to the mixing phenomena. The higher the velocity is, the deeper the penetration into the liquid film. This will force more superheated fluid from the sublayer into the surrounding fluid thus improving efficiency. Also, an impinging droplet can break nucleating bubbles over some radius about the point of impact. The higher the momentum of the droplet is, the larger the radius influenced by the impact. These effects will be discussed in greater detail in Section 5.3.

The spray characteristics also govern the thickness of the liquid film covering the surface. The thickness of the liquid film is an important factor affecting both the efficiency and the critical heat flux. To calculate the film thickness, it is necessary to determine both the momentum and the mass flow rate of the fluid flowing on the surface. The mass flow rate is not the same as the mass flow rate of the spray because fluid is splashed from the surface by the impinging droplets, and expelled from the surface by bursting vapor bubbles. Also, the momentum of the film cannot be estimated from the momentum of the spray because there is no way to estimate the viscous dissipation.

Preliminary modeling attempts to determine the liquid film thickness indicated that approximately 99 percent of the incoming droplet kinetic energy is dissipated in mixing with the liquid film. The kinetic energy is proportional to the velocity squared. The velocity of the impinging droplets is approximately 10 m/s, while the velocity of the liquid flowing on the surface is only estimated to be 1 m/s (kinetic energy 100 times less). Therefore, since mixing is the dominant effect, there is no reasonably accurate way to describe the problem analytically. However, some basic conclusions can be drawn by examining the governing equations.

If the mass flow rate and the momentum of the liquid flowing on the surface are known, the liquid film thickness and velocity can be easily determined. Obviously, as the momentum is increased for a given mass

flow rate, the velocity of the film increases. Therefore, the film thickness decreases.

Recall from Table 3.1, that as the nozzle orifice size is decreased for a given mass flow rate, the droplet velocity increases much more than the droplet size decreases. Therefore, in general the average momentum of droplets increases. From the above discussion, one would expect the film thickness to decrease. However, there are many other factors to take into consideration. Such as, even though smaller droplets have higher momentum, the drag on the droplet as it enters the film has greater effect. Also, the number of droplets impinging the film increases. This increases the amount of mixing that occurs. The conclusion is that it is not readily apparent how the changes in the impinging droplet flow field relate to the momentum of the film flowing on the surface. Therefore, it is necessary to determine more detailed information than knowledge of the the droplet diameter and velocity distributions provide.

First, the percentage of the impinging spray which is splashed from the surface must be determined. To accomplish this, a simple experiment was conducted. A diagram of the experimental apparatus is presented in Figure 5.1.1. The purpose of the experiment is to separate the fluid which is splashed from the surface from that which is flowing on the surface. The diameter of the post was matched to the size of the heated surface. The nozzle was located above the post at the same position as in the experiments. The graduated cylinder is used to determine the flow rate of the liquid film which is then compared to the total flow rate exiting the nozzle.

The results of the experiment are presented in Figure 5.1.2. The percentage of the spray which is splashed is plotted against the flow rate exiting the nozzle. The curve given is the average of the results for all of the nozzles. The curves for the individual nozzles did not vary from this by more than 20 percent, so using the average provides a reasonable approximation.

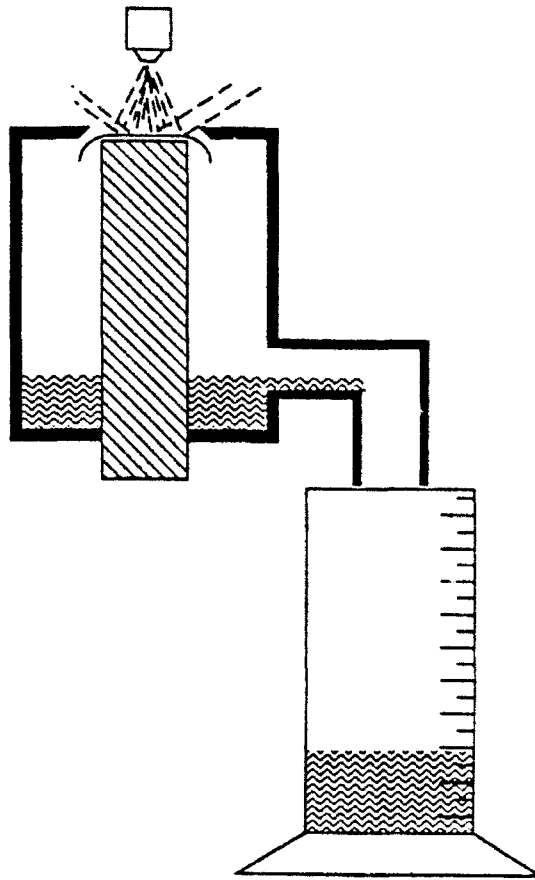


Figure 5.1.1: Splashing measurement apparatus

Of course, the results from this experiment do not include the fluid which is expelled by nucleation during the heat transfer experiments. From the results presented in Chapter 2, this amount can be significant, approximately 10 times the mass flow rate of vapor generated through nucleation.

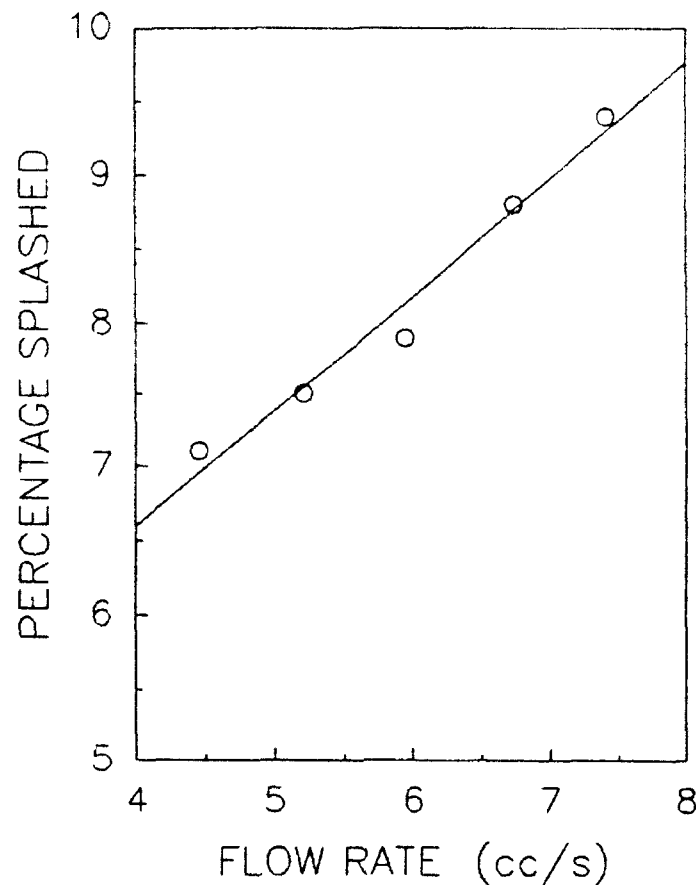


Figure 5.1.2: Splashing measurement results

The next step in determining the film thickness is to determine the momentum of the film flowing on the surface. Since analytical techniques were not suitable because of the uncertainty in the shear term (associated with the droplet impingement), another experiment was conducted. The experiment is designed to analyze the hydraulic jump phenomena associated with the impinging spray.

Hydraulic jump phenomena have been extensively investigated. A general summary and description of the phenomena are presented in Reference 13. References 14 and 15 refer specifically to radial hydraulic jump which is applicable to the present case. With the impinging spray, the hydraulic jump occurs at some radial position greater than the radius of the spray cone. As the fluid flows radially outward from the center, the velocity of the fluid decreases only

slightly due to shear losses, but the radius increases. Since the mass flow rate does not change, the film thickness must decrease to conserve the flow area. Therefore, the Froude number:

$$Fr = v/\sqrt{g\delta} \quad (5.1.2)$$

increases. Upstream of the jump, the Froude number becomes supercritical ($F \gg 1$), and downstream it is subcritical ($F \ll 1$). Across the jump, momentum is conserved, but energy is dissipated. Since the momentum is conserved, by measuring the conditions downstream of the jump, where the flow is quiescent and not affected by the impinging spray, one can ascertain the the momentum of the film exiting the spray cone. Referring to Figure 5.1.3, consider the following governing equation assuming shear loss to be negligible across the jump:

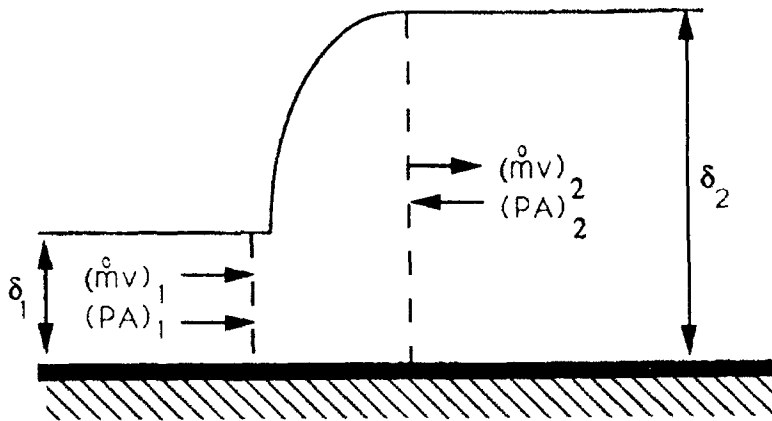


Figure 5.1.3: Hydraulic jump control volume

$$(\rho_l v)_1 + (PA)_1 = (\rho_l v)_2 + (PA)_2 \quad (5.1.3)$$

$$\dot{m} = \rho_l A v, \quad A = 2\pi r \delta, \quad P = \frac{1}{\delta} \int_0^{\delta} \rho_l g y dy = \frac{1}{2} \rho_l g \delta$$

However, since $\dot{m}_1 = \dot{m}_2$ the equation can be simplified. Upon examination of the above equations, it becomes obvious that $(PA)_1 \ll (PA)_2$ and $(\dot{m}v)_1 \gg (\dot{m}v)_2$ if $\delta_2 \gg \delta_1$. In the case of spray cooling, δ_1 is approximately 100 - 400 μm and δ_2 is on the order of 3000 to 4000 μm . Therefore, the error associated with the simplification is about 10 percent. Substituting in all of the appropriate relationships, equation (5.1.3) becomes:

$$v_1 = \frac{\pi \rho_l g \delta_2^2 r}{\dot{m}} \quad (5.1.4)$$

The film thickness, δ_1 , is then found through the definition of the mass flow rate:

$$\delta_1 = \frac{\dot{m}}{2\pi r \rho_v v_1} \quad (5.1.5)$$

The above analysis indicates that a simple experiment may be utilized to obtain a "ballpark" estimate of the liquid film thickness. The apparatus designed to do this is presented in Figure 5.1.4. A plexiglas plate was threaded into a large diameter brass pipe with a knife edge machined on its rim. The depth of the fluid, δ_2 , was then controllable by adjusting the position of the plexiglas plate. Then, under the desired spray conditions, the radius at which the jump occurs, and thickness, δ_2 , were measured. The radius was measured to within ± 2 mm using fine grid paper taped to the bottom of the plexiglas plate. The film thickness was measured using a traversing measuring scope and a needle pointer. The measurement scope had a resolution of 10 μm , but due to flow fluctuations, the actual uncertainty is probably closer to 200 μm .

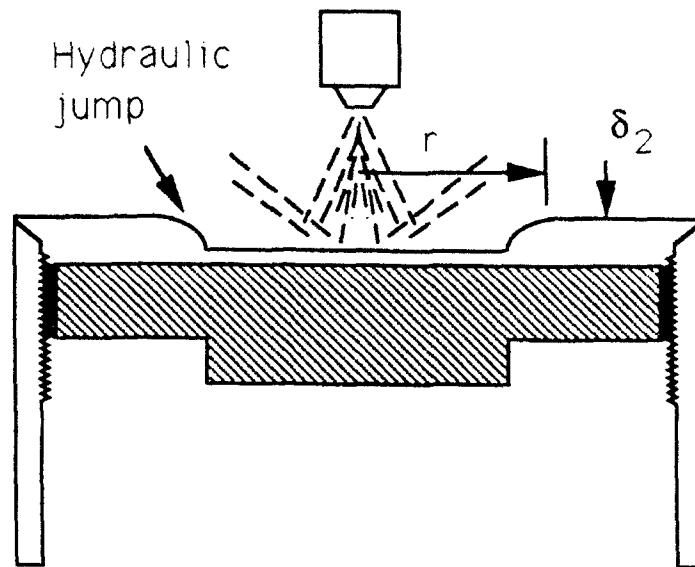


Figure 5.1.4: Hydraulic jump measurement apparatus

The measurements conducted in the experiment yield a film thickness estimate at the edge of the jump. The film thickness at the edge of the spray cone can also be estimated if shear loss is neglected. Since there is no way of determining the momentum and mass flow rate of the film in the spray cone, the estimate at the edge is assumed to apply. However, in many cases, nonuniformity in the spray cone has demonstrated that the film thickness can vary significantly inside the spray cone. In cases where the spray cone is somewhat hollow, liquid is seen to build up in the center and then periodically dissipate. Since it is impossible to account for all of these factors, the results of this film thickness estimation are useful only to explain the trends observed in the experimental data.

The results of the film thickness determination are presented in Figure 5.1.5. The flow rate given is the flow rate at the nozzle exit, though the flow rate used in the calculation was adjusted based on the percentage of the spray which was splashed (presented in Figure 5.1.2). The results indicate that the film thickness does not change significantly with the different nozzle orifices, especially at low flow rate, except for the nozzle with the largest orifice diameter. This

nozzle had very low momentum. In fact at the lowest flow rate, tests were not conducted because the hydraulic jump was right on the edge of the spray cone, and periodically, fluid would collapse onto the test surface. With the other nozzles, since the majority of the impinging droplet momentum is dissipated by mixing with the liquid film, not much difference exists.

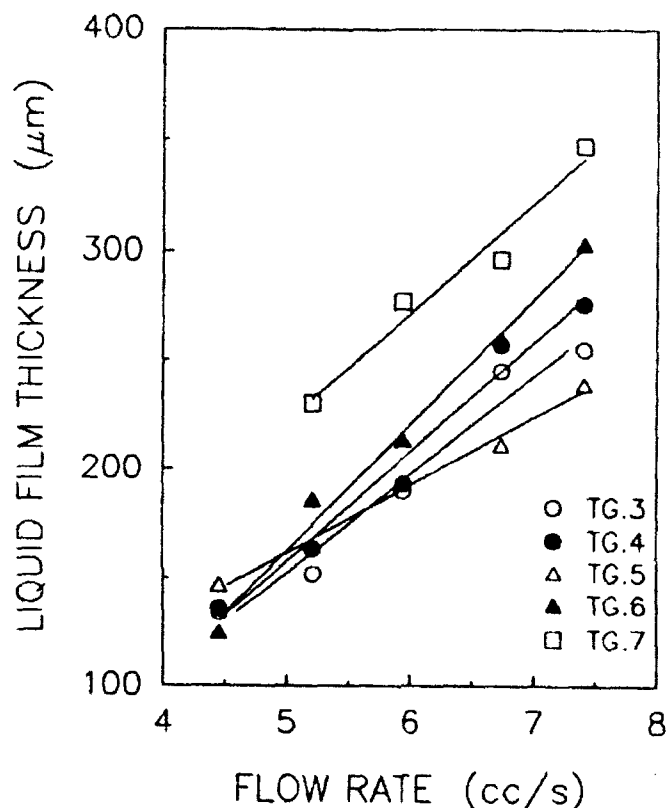


Figure 5.1.5: Film thickness estimation results

Of course, the film thickness measurements here are obtained under a quite different flow situation than would be encountered during the actual experiments. This is due to the fact that nucleation phenomena can have a significant effect. A large percentage of the flow can be expelled from the surface due to breakage of the vapor bubbles within the liquid layer as discussed in Chapter 2. This reduces the film mass flow rate, therefore decreasing the film thickness. On the other hand, the generation of vapor within the film displaces liquid, therefore thickening the film. Also, the shear losses would increase due to increased mixing and fluid changing path to flow around nucleating

bubbles. This would also have the effect of increasing the thickness of the liquid film. Therefore, it is not apparent exactly how the thickness changes with the addition of the heat transfer situation. However, the estimates presented here are still thought to provide a reasonable approximation. Also, the trends in the film thickness would probably not change significantly. Therefore, the results are very useful as an analysis tool.

The last important factor to be discussed concerns how the spray characteristics interact with the liquid film. It has already been mentioned that the impingement enhances mixing as shown in Figure 4.3.3. Another factor which may be important concerns secondary nucleation. It has been reported, that when droplets impinge the liquid film, in thin film boiling systems, vapor is entrained into the liquid film [16,17]. Observations indicate that vapor is pushed into the film and can serve as a nucleus for a new bubble. In spray cooling, since the impingement frequency is so high, this secondary nucleation could play a major contributing role. The most important influence concerns how the spray affects the nucleating bubbles. These effects are discussed in Section 5.3 after the nucleation phenomena are explained.

5.2: EFFECTS OF SURFACE CONDITIONS

Recall from Chapter 4 that the surface roughness can have a profound effect on the heat transfer. Figure 4.3.9 compared the results for smooth and rough surfaces for the same spray conditions. This section describes how the surface conditions affect the heat transfer so these results can be more accurately described.

First, it is necessary to determine how many active nucleation sites result from a given surface roughness and surface temperature. Active nucleation site density has been extensively studied as it relates to pool boiling phenomena [18-22]. Brown was able to show that the active nucleation site density was well correlated to the minimum cavity radius by the power law:

$$(N)_{r_c} \propto (1/r_c)^m \quad (5.2.1)$$

where r_c is the minimum cavity radius which will support a nucleating vapor bubble according to static equilibrium criterion [18]. The constant of proportionality and the power m are empirically determined based on the fluid and the surface roughness conditions. The minimum cavity radius is determined for a given superheat using the Clausius-Clapeyron equation such that the saturation pressure of the vapor in the bubble matches the required capillary pressure based on the cavity radius:

$$r_c = \frac{2\sigma T_{\text{sat}}}{\rho_v \lambda (\Delta T)} \quad (5.2.2)$$

Corty and Foust used this same relationship and investigated different fluid/surface material and roughness combinations [19]. They showed that a wide range of data was well correlated by a relationship of this type, but none of the correlations they presented were for surface roughnesses comparable to the present research. Gaertner [20] and Kurihara and Myers [21] investigated the size distribution of active nucleation sites using a statistical approach with the theory of thermal fluctuations. They found that the size distribution is well represented by a Poisson distribution. Shoukri and Judd also used the power law relationship but studied much smoother copper surfaces with water [22]. This research was thought to be most applicable because, curves were presented for surface roughness conditions comparable to the present research.

The paper by Shoukri and Judd was used to plot Figure 5.2.1 which shows the active nucleation site density plotted against the surface temperature for two different surface roughnesses. The curve labeled Rough, is plotted for a 0.4- μm centerline average roughness and the curve labeled Smooth, is for a 0.1- μm surface. The surface preparation procedures are described in the paper and closely match the procedures used in the spray cooling tests. The figure shows that the rough surface has significantly more active nucleation sites at any given

surface temperature. There may be some difference in the actual number of sites in the present experiments, due to different surface roughness and different shape of the thermal boundary layer, but Figure 5.2.1 can be used to analyze the experimental data. This analysis will be presented after a description of the bubble growth rates.

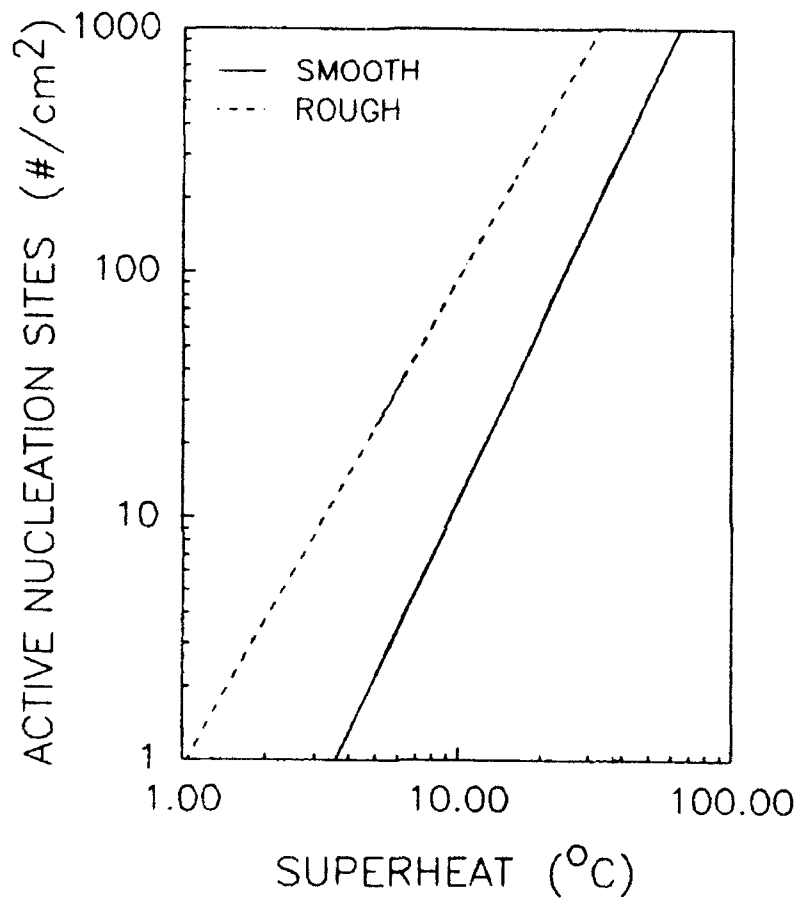


Figure 5.2.1: Active nucleation site density

The next step is to determine how fast a bubble will grow once a site has been activated. The higher the surface temperature, the more heat transferred to the growing vapor bubble. Bubble growth rates have been extensively studied in conjunction pool boiling. One of the earlier works was presented by Forster and Zuber who defined to separate regions of interest over the lifetime of the bubble [23]. The initial bubble growth is controlled by inertia and the latter growth is

controlled by diffusion. They only formulated a solution for the latter growth region. Sernas and Hooper performed an extensive study on initial vapor bubble growth using high speed photography techniques [24]. However, the results are only applicable for bubble radius greater than 150 μm . This is the problem, in analyzing bubble growth rates for spray cooling. In pool boiling, the period of bubble growth below 150 μm contributes very little to the overall heat transfer since bubbles generally grow to at least 2 millimeters before departure. Therefore, the earlier region of bubble growth is rarely investigated. In spray cooling, because the film is so thin, and the bubble lifetime is controlled by the impingement phenomena, the region of interest is generally confined to bubbles less than 300 μm in size. It is very difficult to experimentally verify bubble growth rates in this very early region, and no literature was found. Mikic et al. do provide an analytical solution for bubble growth from a superheated wall that describes both inertia and diffusion controlled growth [25]. In spray cooling, growth is mostly inertia controlled until the later stages. Therefore, the transition region, in which both inertia and diffusion effects are important, is relevant.

The complete development will not be presented, but the equation governing the bubble growth is given below:

$$R^+ = 2/3[(t^+ + 1)^{1.5} - (t^+)^{1.5} - 1] \quad (5.2.3)$$

where: $R^+ = \frac{AR}{B^2}, \quad t^+ = \frac{A^2 t}{B^2}, \quad A = \left[\frac{\pi \Delta T \lambda \rho_v}{7 T_{\text{sat}} \rho_l} \right]^{1/2},$

$$B = \left[\frac{12}{\pi} Ja^2 a_l \right]^{1/2}, \quad Ja = \frac{\Delta T c_l \rho_l}{\lambda \rho_v}$$

This equation is used to plot the bubble growth rate as a function of time for different surface temperatures in Figure 5.2.2.

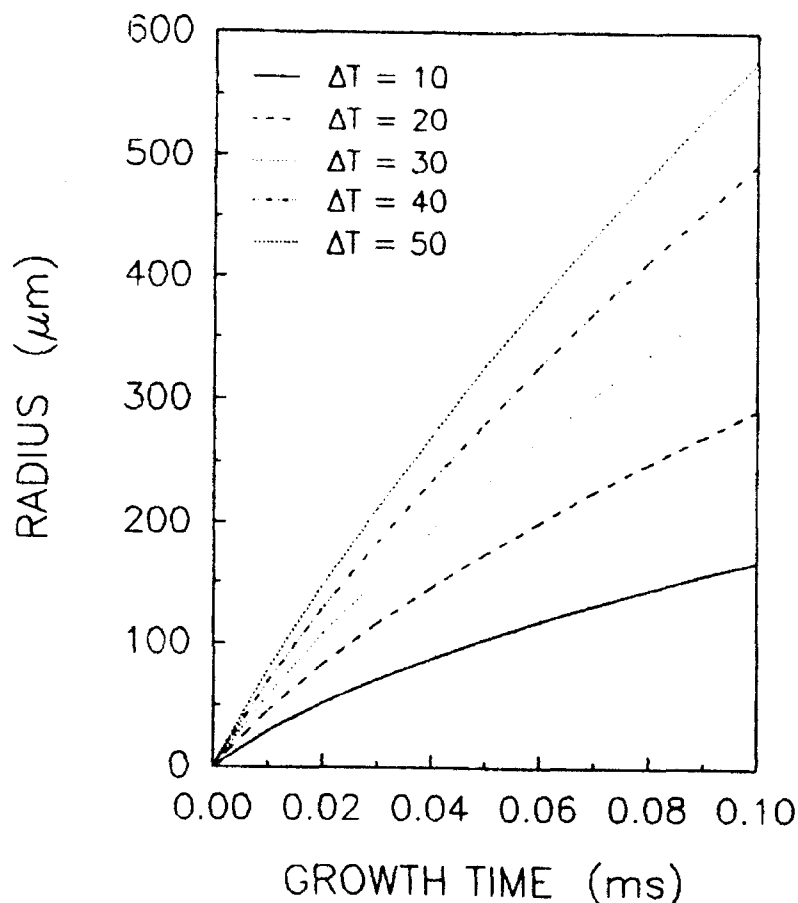


Figure 5.2.2: Vapor bubble growth rates

From Figures 5.2.1 and 5.2.2 it is easy to see why nucleation begins to have such a profound effect on the heat transfer as the surface temperature is increased. Both the number of nucleations sites and the bubble growth rate increase rapidly with increasing temperature. The vapor generation rate is proportional to the number of nucleation sites, and the bubble radius to the third power. Since the mass of fluid expelled due to nucleation can be as high as 10 times greater than the mass flow rate of vapor generated, the liquid film on the surface can be highly disrupted by nucleation. In fact, as seen in Chapter 2, this fluid expulsion can result in transition to the CHF in lower flow rate cases. The relationship between nucleation and the CHF for the high flow rate cases will be described in Section 5.3.

Now that some theory concerning the rate of bubble growth is

available, it must be determined how long a bubble grows. If a force balance is conducted, similar to what is done to determine bubble departure dynamics, it is evident that surface tension forces dominate. If the bubble radius is always assumed to remain below 300 μm , the surface tension force is on the order of 10^{-5} N. The buoyancy force and the liquid inertia force are on the order of 10^{-7} N. Therefore, it is evident that at that small size, the dynamic forces on the bubble are not sufficient to break the bubble. If a bubble grows such that it forms a hemisphere above the liquid film, the surface tension forces cause fluid to drain from the liquid dome. This can cause the bubble to break at the apex. However, the time required for this to happen is far longer than the period of bubble growth. The conclusion is that bubbles only break when a droplet impinges in its general vicinity. The instability created, or the direct impact, is sufficient to rupture the liquid film, allow the vapor to escape, and rewet the nucleation site. This indicates that the impingement phenomena and the bubble nucleation phenomena control the critical heat flux phenomena. Unless the impingement frequency is high enough, there is no mechanism available to break the bubbles. If this is the case, the vapor generated at the surface forms a vapor barrier when the bubbles grow together and conglomerate.

Bubbles which break at the surface may also be another source for secondary nucleation. Mesler and Mailen [26] and Bergman and Mesler [27] have reported that new bubble nuclei are formed when a bubble bursts in a thin liquid film. There is no way to predict the exact relationships, but increased nucleation sources should contribute to the critical heat flux phenomena.

5.3: ANALYSIS

The previous two sections described phenomena relating to the effects of the spray and surface conditions. In this section, these results are used to describe how the individual effects relate to each other to influence the heat transfer efficiency, and the critical heat flux. The analysis is used to provide more detailed explanation of the

experimental results already presented.

5.3.1: Critical Heat Flux

It was previously postulated that the critical heat flux for the high flow rate cases occurs when the impingement frequency is no longer sufficient to maintain the liquid film on the surface. The nucleation site density and the bubble growth rates become so high that a vapor is formed in a given region in the time interval between successive impinging droplets.

Many researchers have investigated critical heat flux in various types of thin film boiling systems. Ueda et al. reported that the CHF occurs, in high-flow-rate falling film heat transfer, when the vapor generation rate becomes sufficiently high that the film separates from the surface [8]. For lower flow rates they concluded that the CHF resulted from fluid deficiency caused by droplet expulsion as discussed in Chapter 2. Toda and Uchida observed similar CHF phenomena in their study of liquid film cooling using a plane wall jet [28]. Several researchers have noticed the same mechanisms for CHF in jet impingement cooling [29,30,31]. These works indicate that the CHF occurs when the liquid film lacks sufficient momentum towards the surface to overcome the vapor trying to escape the surface. Thus, it is deflected from the surface and a vapor barrier is formed.

In Chapter 4 it was shown that, in general the critical heat flux increases with increasing impingement frequency. However, Figure 4.3.5 still showed significant scatter. The scatter can be explained when more detailed information is examined as it relates to the postulated mechanism for transition to critical heat flux. It has been mentioned several times that the critical heat flux is related to the relationship between the impinging spray and the nucleation phenomena. While vapor generated at the surface tends to cause the formation of a vapor barrier, the droplet impingement tends to destroy nucleating bubbles, expel the vapor, and rewet the nucleation sites. In Section 5.1, it was shown that as the flow rate is increased, the impingement frequency also increases. In Section 5.2, it was shown that as the surface temperature increases, the amount of vapor generated at the surface also increases. Since the spray characteristics do not change as the surface temperature

is increased, one would expect the vapor generation effects to overcome the impingement effects at some point. The key is determine what that point is.

It has been stated that droplets impinging the liquid film have sufficient momentum to rewet nucleation sites and expel the vapor from a certain region surrounding the point of impact. Assume this region has a diameter of some factor, β , times the droplet diameter before impact. This factor, β , would be influenced by the droplet momentum and the film thickness. The higher the momentum, the larger the range of influence. The thicker the film, the smaller the range of influence. The exact relationships or values for the parameter, β , cannot be determined but above statements reasonably describe the trends. Assuming β is known, the average time it takes the impinging droplets to rewet all the nucleation sites (average bubble lifetime) could be calculated:

$$t_{ave} = \frac{A}{\bar{n}(\beta d)^2} \quad (5.3.1)$$

This assumes that the impingement frequency, \bar{n} , is uniformly distributed. The surface area, A , divided by the area influenced by a given impact, gives the average number of droplets which must impinge the surface to reinitialize all the nucleation sites. Then dividing by the impingement frequency gives the average bubble lifetime. The above equation indicates that the higher the impingement frequency, the shorter the average life time of the bubbles growing on the surface. The same is true for the (βd) product.

Now, if the average bubble lifetime is known, Figures 5.2.1 and 5.2.2 can be used to determine the vapor generation rate at a given surface temperature. At the desired surface temperature Figure 5.2.1 is used to determine the number of active nucleation sites per unit area, N . Figure 5.2.2 is used to determine the average radius to which bubbles grow before being destroyed by an impinging droplet. Then the vapor generation rate at the surface is given by:

$$\dot{m}_v = \frac{4}{3}\pi N A_s \rho_v \frac{(r_{ave})^3}{t_{ave}} \quad (5.3.2)$$

This relationship does not account for the two sources of secondary nucleation previously mentioned. Therefore, the vapor generation rate is likely underpredicted. The heat removed through nucleation can be estimated by multiplying the latent heat of vaporization, λ , by the mass flow rate of vapor generated.

Figure 5.3.1 shows an estimation for the heat flux removed by nucleation for a range of impingement frequency, for an average droplet diameter of $125\ \mu\text{m}$, and β equal to 8. The figure shows that as the impingement frequency is increased, the heat removed by nucleation at the surface is decreased. Similarly, Figure 5.3.2 shows that at constant impingement frequency, increasing β also reduces the heat removed by nucleation.

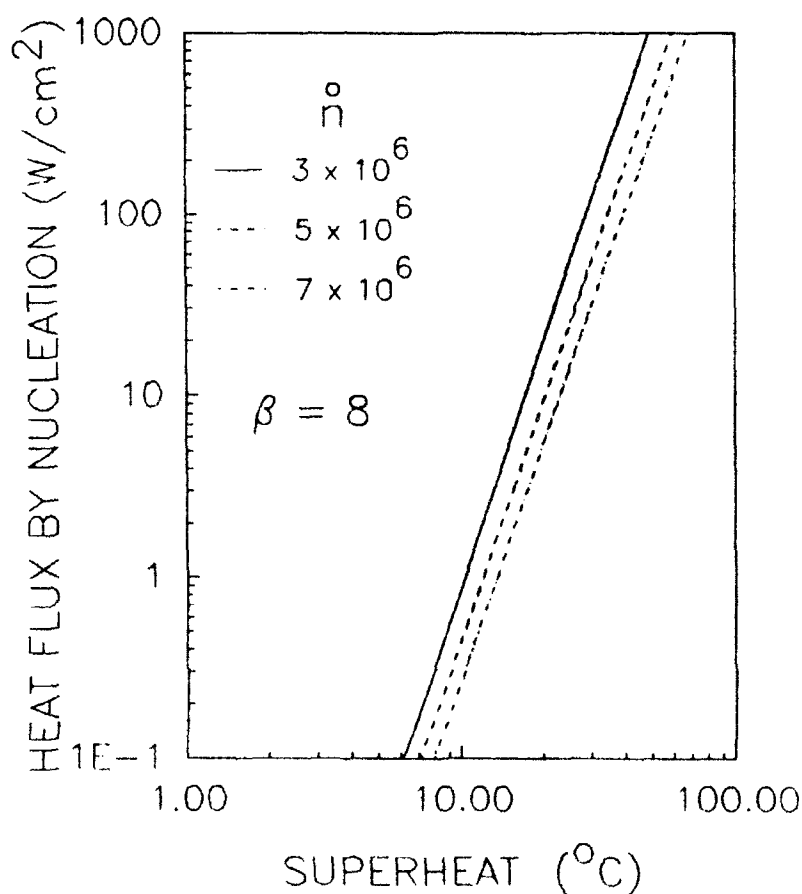


Figure 5.3.1: Heat flux from nucleation, impingement frequency effects

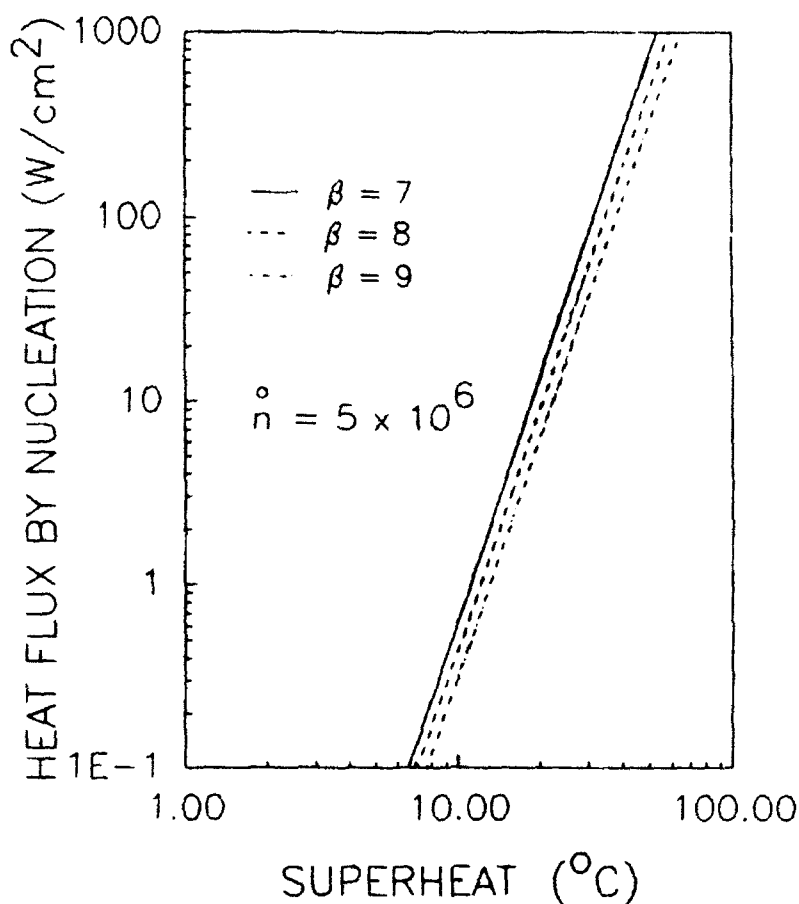


Figure 5.3.2: Heat flux from nucleation, effects of β

From Figures 5.3.1 and 5.3.2, it is apparent that it is possible for the effects of increasing impingement frequency to be offset by decreasing β . For any given nozzle, as the mass flow rate is increased, the impingement frequency, the liquid film thickness, and the average droplet velocity all increase. Therefore, it is not immediately clear how the heat flux removed by nucleation will be affected. The smaller the orifice diameter, the larger the increase in droplet velocity with increasing flow rate. This indicates that β should decrease less for smaller orifice nozzles. Again it should be mentioned that these plots do not include the effects of secondary nucleation, which could be significant.

With the above analysis, the trends in the experimental data presented in Chapter 4 can be explained. All the data used to perform

the following analysis are presented in Table C.1 in Appendix C. Several conclusions can be drawn which are well supported by the data. Since the bubble growth rate and the number of active nucleation sites are functions of the surface temperature, it makes more sense to compare the surface temperature at CHF rather than the CHF itself. For example, for two different cases, if the impingement frequency is the same, and the liquid film thickness and average droplet momentum are comparable, one would expect the CHF to occur at the same surface temperature. This is indeed the case with nozzles TG.3 and TG.4 both operating at 60 percent of the maximum flow rate. The film thickness and impingement frequency are approximately $135\ \mu\text{m}$ and $4.4 \times 10^6\ \text{s}^{-1}$, respectively (see Table C.1). The CHF is shown to occur at $130\ ^\circ\text{C}$ in both cases. Comparing TG.3 at 90 percent flow with TG.5 at 100 percent flow shows the same result. The film thickness and impingement frequency for these case are approximately $240\ \mu\text{m}$ and $7.2 \times 10^6\ \text{s}^{-1}$.

If the impingement frequency is the same for two different nozzles, the case with higher β will have a higher surface temperature at CHF. For example, nozzle TG.3 and TG.4 have approximately the same impingement frequency at 70 percent flow. However, the film thickness is seen to be greater, and the droplet velocity is lower for nozzle TG.4. Therefore, β should be lower for nozzle TG.4, indicating CHF should occur at a lower temperature. This is true as the CHF occurred at $130\ ^\circ\text{C}$ for TG.4 and 135°C for TG.3. The same trend is demonstrated by comparing nozzles TG.5 at 80 percent, and TG.6 at 90 percent. Similarly, if the film thickness is nearly the same, the nozzle with the higher impingement frequency and droplet momentum will have a higher surface temperature at CHF. This is shown by comparing nozzle TG.5 at 80 percent with Nozzle TG.6 at 90 percent and nozzle TG.3 at 100 percent with TG.4 at 90 percent. For both of these cases, the CHF is delayed to a higher temperature for the nozzle with the highest impingement frequency and droplet momentum.

Even though the above trends are predicted by the modeling and represented in the data, there are many cases that are contradictory to the trends. Again, it appears that the uniformity of the spray cone plays a predominant role in these cases. Recall that if the spray cone is hollow in the center, this increases the film thickness and decreases

the impingement frequency. Both of these effects cause CHF to occur at a lower temperature. An example of the dependence on spray cone uniformity is shown by comparing nozzles TG.4 and TG.5 at 80 percent flow. The film thickness was estimated to be approximately $193\text{ }\mu\text{m}$ for both cases. However, the impingement frequency and the average droplet momentum are both higher for nozzle TG.4. Therefore, one would expect that the CHF would occur at a higher temperature for nozzle TG.4, but the opposite is true. Experimental observations indicated that the spray cone for nozzle TG.4 was hollow in the center while TG.5 had the most uniform spray cone of all the nozzles. It was observed that at about $132\text{ }^{\circ}\text{C}$, the center of the surface dried out. Then there was a very small area in the center which was above the Leidenfrost point and was nonwetting. The rest of the surface was still in the wetting range because the spray characteristics were good. This caused the average surface temperature to jump to $136\text{ }^{\circ}\text{C}$. From this point, just a small increase in surface temperature caused the entire surface to transition.

Reanalyzing Figure 4.3.9 may provide additional insight since the spray characteristics do not change. The differences in the heat transfer results are attributable only to nucleation and bubble growth phenomena. Recall that the CHF occurred for the rough surface at a surface temperature of $21\text{ }^{\circ}\text{C}$ while the smooth surface did not jump until $38\text{ }^{\circ}\text{C}$ under the exact same spray conditions. Since the spray conditions are the same, one would expect the CHF to occur when nearly the same amount of vapor is being generated at the surface by nucleation. Calculations using nucleation and growth models presented indicate that, at the CHF, the rough surface nucleation heat flux is about 90 W/cm^2 . The smooth surface heat flux is about 130 W/cm^2 . Figure 5.2.1 indicated that at the CHF there were approximately 456 nucleation sites on the rough surface and only 235 on the smooth surface. So even though the heat flux by nucleation was lower, the vapor generation was much more evenly distributed over the surface area. The bubbles on the rough surface grow at a much slower rate and consequently only reach an average radius of $90\text{ }\mu\text{m}$. On the smooth surface the bubbles reach an average radius of $125\text{ }\mu\text{m}$. Its possible that the CHF occurs when bubbles adjacent to each other begin to conglomerate to form a vapor barrier. If this is true, then the projected area of the vapor bubbles may

provide a better comparison. Indeed, the smooth and rough surfaces both indicate that the projected area of the vapor bubbles covering the surface is 0.11 cm^2 under the above assumptions. Since the surface is 1 cm^2 in diameter, this does not seem like enough vapor to blanket the surface. However, this estimate does not include secondary nucleation as mentioned previously. If many more bubble nuclei are formed by droplet impingement and bursting vapor bubbles, the amount of nucleation may be significantly higher. It has been reported that as many as five bubble nuclei can form from one impinging droplet [17]. During the average bubble lifetime, even if only one nucleus is formed from each impinging droplet, this could provide about 150 additional bubbles. It has also been reported that as many nuclei are formed when a vapor bubble bursts in a thin film [27]. This indicates that the number of sites may again be doubled by this mechanism.

Considering all of the mechanisms for nucleation it is easy to see why transition to CHF occurs so rapidly. As the temperature goes up, the number of active sites increases rapidly. Since these sites can potentially create new sites by the secondary bursting mechanism, the amount of vapor generated at the surface increases drastically. Also, if two smaller bubbles growing next to each other combine, the new bubble radius is larger. This indicates that the saturation pressure associated with the new bubble would instantly drop. This may cause a very rapid increase in growth rate because the fluid in contact with the bubbles interface, which was superheated to the level dictated by the smaller radius, is suddenly exposed to a lower saturation temperature at the interface. Therefore, as soon as adjacent bubbles begin to touch, the growth rate increases rapidly and a vapor barrier is formed.

5.3.2 Heat Transfer Efficiency

The previous section described how the spray characteristics and surface conditions interacted in relation to critical heat flux phenomena. However, only the trends in the surface temperature at the CHF were described. To determine the heat flux at a given temperature, the heat transfer coefficient must be determined. This section describes the relationships between the heat transfer coefficient and the spray and surface conditions.

Figure 5.3.3 shows the heat transfer coefficient plotted against the flow rate for all of the closed-system, single-component tests with the smooth surface (data given in Appendix C). At first glance there does not appear to be any trend. However, the graph corresponds very well to the observed characteristics of the spray cone. For example, nozzle TG.3 showed the most variation in spray cone shape as the flow rate was increased. At low flow rate the spray cone was fairly narrow (did not cover the entire surface). As the flow rate was increased, the spray cone angle also increased, providing a more uniform distribution of higher momentum droplets. Consequently, as seen in the graph, the heat transfer coefficient improved rapidly. Then, as the flow rate continued to increase, the spray cone began to hollow out in the center. This reduced the rate at which the heat transfer coefficient improved. Nozzles TG.4 and TG.6 both had very similar spray cone shape. They were both fairly narrow, and hollow in the center. The shape did not change much with increases in the flow rate. Both of the curves for these nozzles exhibit the same slope. The curve for nozzle TG.4 though has much higher values because the impingement frequency is higher, the droplets have higher momentum, and the film thickness is lower. Nozzle TG.7 shows the lowest improvement in heat transfer coefficient with increasing flow rate. Recall, as described in Chapter 4, the momentum of the droplets barely increases. Therefore, as the impingement frequency and the film thickness go up (with increasing mass flow rate), the effects offset each other resulting in only slight improvement. Nozzle TG.5 had the most uniform spray cone, and the spray angle was well matched to the surface size. The shape hardly changed as the flow rate was increased. The graph shows that the curve for this nozzle had the highest slope.

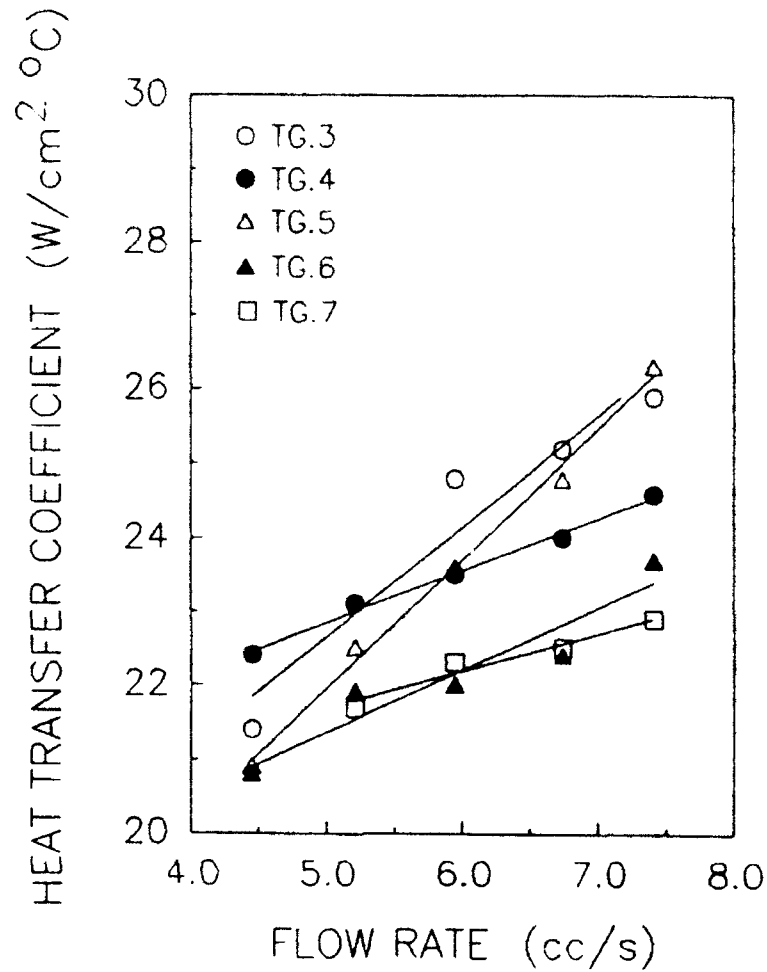


Figure 5.3.3: Heat transfer coefficient vs. nozzle flow rate

The slope of the graphs of heat transfer coefficient versus flow rate can be explained by examining how the important parameters change with increasing flow rate. The heat transfer coefficient should be directly proportional to the impingement frequency and the droplet momentum since the heat transfer is dominated by mixing. It should be inversely proportional to the film thickness for the same reason. Therefore, the highest improvement in heat transfer coefficient should occur in cases where the increases in impingement frequency and droplet momentum outweigh the increases in the liquid film thickness. Using Table C.1 in the Appendix, the relative increases in the important parameters can be calculated to indicate the expected trends in the improvement of the heat transfer coefficient with increasing flow rate.

For example, if:

$$h \propto \frac{d^3 v n}{\delta} \quad (5.3.3)$$

one can estimate the improvement in heat transfer coefficient since all the parameters on the RHS are given in Table C.1 as functions of the nozzle and flow rate. When this is done, the trends in percentage improvement are exactly predicted even though the actual percentage improvement is not predicted. This is probably because the exact relationships between the above parameters are very complex and cannot be well defined. For example, even if two droplets have the same momentum, if one droplet is smaller than the other it will be decelerated more rapidly upon entering the film. Therefore, it may not be as effective at forcing fluid out from the superheated sublayer as the larger droplet. Also, other parameters may be important which are not included, such as the liquid film velocity. The spray cone shape and uniformity are also not taken into account. As mentioned earlier, in the description of Figure 5.3.3, the shape and uniformity of the spray cone may have the greatest influence.

All of the above discussion on heat transfer efficiency was under the assumption that the nucleation conditions on the surface did not change. The discussion of the trends concerned only how the mixing would be affected by changes in the spray characteristics. Since the efficiency is also dependent on the percentage of heat removed by nucleation, these effects should also be investigated. Since heat transfer to a nucleating bubble is very efficient, it is expected that the more nucleation occurring, the higher the heat transfer coefficient. This is because of the very efficient microlayer heat transfer associated with nucleation.

In pool boiling, the surface roughness has been shown to play a significant role in the heat transfer efficiency. In general, the rougher the surface, the higher the heat transfer coefficient [18-22]. Recall that in Figure 4.3.9, when the rough surface heat transfer case is compared to the smooth surface case, the same is shown to be true. At low surface temperature, when there are very few active sites for

both cases, the efficiency is the same. As the surface temperature increases, the number of nucleation sites on the rough surface increases at a higher rate resulting in improving heat transfer coefficient.

The analysis presented in this section has effectively described the physical phenomena and explained the observed trends in the experimental results. This analysis also enables explanation of the wide variation in the results of previous researchers mentioned in Chapter 1. Comparison of the present research with that of previous researchers is presented in Chapter 7. Even though a much greater understanding has been achieved, there are still many important parameters whose effects are not well defined. There is also significant uncertainty associated with many of the approximations made in the analysis. Recommendations for future research that will further improve understanding are given in Chapter 8.

CHAPTER 6: DROPWISE EVAPORATION

In spray cooling, when the impinging spray is very light, the surface is not completely covered with fluid. As the small drops impinge, they flatten out and form very thin disk-shaped wet patches which undergo evaporation from the upper liquid/vapor interface. Very little nucleation is observed to occur in these cases.

This chapter describes theoretical and experimental investigation into this type of low surface saturation spray cooling, beginning with a brief introduction. A two-dimensional transient conduction model is presented which calculates the temperature profiles in the surface beneath the evaporating droplet. This model is extended to predict the surface temperature which will result from a given heat flux, percent of wet surface area, and average impinging droplet diameter. The model shows good agreement with experimental results.

6.1: INTRODUCTION:

In certain applications of spray cooling, it is desirable to vaporize all of the fluid which is sprayed onto the surface. This is true in cases where excess fluid removal is difficult due to large surface areas or other factors. In these cases it is necessary to provide the proper spray characteristics or droplet conglomeration will occur, the heat flux will drop, and the surface will become flooded. It is also desirable to determine the conditions which provide the most efficient heat transfer for a given heat flux.

It is hypothesized that several factors significantly affect the heat transfer efficiency. For example, it is obviously better to have several small droplets evenly spread over the surface than one large droplet in the center. This is true for several reasons. First, the smaller droplets will form thinner disks on the surface thus minimizing the temperature drop required to conduct the heat through the droplet to the upper liquid/vapor interface where evaporation occurs. Also, at the perimeter of the droplets, where the liquid/vapor interface contacts the solid surface, the heat transfer is very

efficient. When several small droplets exist, as opposed to one large droplet of the same combined fluid volume, the perimeter-to-volume ratio is much higher. Also, in the larger droplets, if the conduction drop through the droplet is very high, nucleation will occur in the droplet. Nucleation can result in fluid being ejected from the surface due to the rapid vapor expansion in the nucleating bubble. This would result in reduced liquid supply which in turn would lower the heat flux. Another factor which indicates that the smaller droplets would provide more efficient heat transfer results from the conduction in the solid surface itself. If the heat is conducted to several small patches evenly distributed on the surface, instead of one large patch, the temperature gradients in the solid surface are reduced.

This discussion indicates that modeling of the heat transfer in the solid surface and the droplet can aid in determining the best method to efficiently cool a surface using low surface saturation spray cooling.

In this type of spray cooling, which is characterized by dropwise evaporation, predictions of the average surface temperature can be made. In order to accomplish this, it is necessary to define the liquid distribution on the surface. The distribution of liquid on the surface is affected by the average droplet size and velocity, the volume flux and the heat flux. The droplet size and velocity dictate the size of the wet patches which will be formed when a droplet hits the surface and spreads out. For this analysis, the volume flux is matched to the heat flux such that all the liquid is vaporized. This analysis is also restricted to low values of surface saturation, so that droplet conglomeration does not occur.

The following sections describe experimental and analytical investigations into this type of spray cooling.

6.2: EXPERIMENTAL INVESTIGATIONS:

Experiments were conducted with low values of surface saturation to determine the limits on this type of heat transfer. However, the experimental apparatus was designed for the high flux tests as previously described in Chapter 3. The main problem with using the

present apparatus for the low flux tests resulted from the design of the integral thermocouples. Because an extremely thin constantan film is required to minimize the temperature of the heater block for the high flux tests, the temperature drop across the film is too low to provide accurate measurements when the heat flux is low. Uncertainty analysis indicates that at a heat flux of 1000 W/cm^2 , the error is only about 5.3 percent. However, at a heat flux of 100 W/cm^2 the uncertainty is 37 percent (See Appendix A). Therefore, it is difficult to compare the experimental results to the analytical modeling.

With an apparatus more suitably designed for low flux testing (Much thicker constantan film), the methods described would provide excellent results. Because of the high experimental uncertainty, only a few cases were run and compared to the model predictions. However, Bonacina et al. have conducted many experiments which are suitable for comparison [3]. These experiments compare very favorably with the model predictions as discussed later.

To compare the experiments to the model predictions, it is necessary to measure several parameters. These are, the average droplet size and velocity, the percent of wet surface area, the heat flux to the surface, and the average surface temperature.

The average droplet diameter and velocity are used to calculate the Weber Number as:

$$We = \frac{\rho dv^2}{\sigma} \quad (6.2.1)$$

After Kurabayshi et al., the Weber number is used to determine β , the droplet spreading ratio (spot diameter to drop diameter ratio) [32].

Then for these experiments, the average droplet diameter and velocity were measured using the digital video and image analysis systems as described in Chapter 3, Section 3.2.

The percent of wet surface area was also measured using the digital video and image analysis system. To do this, a thin sheet of light from an argon ion laser was used to illuminate the surface. The sheet light was directed at the surface at a very low angle of incidence. This allows the light to enter the wet patches but not escape. Thus, the wet

patches appear darker than the dry portions of the surface. In order to achieve better measurements, the surface was polished to a mirror finish.

For filming, the exposure time was set to a small fraction of the estimated droplet residence time. The surface was heated up from a flooded condition until a steady state was reached in which the surface was less than 30 percent wet. The heat flux and surface temperature were then recorded. After filming the surface under these conditions, the percent of wet surface area was calculated using the image analysis system. First, the pixel attributes function was used to determine the average intensity of the wet patches. Then a box was drawn around a desired portion of the surface, and a pixel intensity histogram is plotted. The ratio of the number of pixels with intensity equal to or below the average determined value to the number of those above, is equal to the percent of wet surface area. The accuracy of the technique is probably no better than 30 percent because of the uncertainty associated with the choice of the cutoff pixel intensity.

The results of these experiments are presented with those of Bonacina et al. and compared to the predictions of the analytical model in Section 6.5.

6.3: ANALYTICAL MODELING

The experimental results indicate that the heat transfer efficiency varies greatly with changes in the surface saturation and the average impinging droplet diameter. In order to predict the most desirable heat transfer conditions, and the maximum heat flux for a given set of spray conditions, it is desirable to model the heat transfer. This section describes the model developed to predict the surface temperature resulting from a given set of spray conditions and heat flux. This model is then compared to the experimental results with good agreement in the following section.

The model is based on the solution of the transient conduction problem from a heated solid surface to an evaporating droplet. The finite difference equations are solved using the Alternating Direction

Implicit solution scheme (ADI). The model is based on a problem definition similar to that presented by Rizza [33]. However, his results are not presented in a fashion which is easy to use. His model also required the assumption that the thermal capacity of the surface was negligible (which cannot be assumed in many cases). He, therefore, solved the steady-state problem at each time step based on the time dependant droplet geometry. He also neglects the heat transfer resistance within the droplet, which in many cases is the dominant resistance in the system. The model presented here is more accurate and requires fewer simplifying assumptions.

6.3.1: Model Assumptions

The model is based on the following simplifying assumptions:

1. The surface temperature resulting from a multiple droplet spray can be approximated by the temperature of a unit cell. The unit cell is defined by the percent of wet surface area, the average impinging droplet diameter, and the spreading ratio. This assumption introduces some error because the actual droplet diameters vary over a fairly wide range. Also, they are randomly, not uniformly distributed on the surface. These effects should result in underprediction of the actual surface temperature.
2. Vaporization occurs at the upper liquid/vapor interface, and nucleation within the wet patches is neglected. This assumption indicates that the surface temperature under the droplet is greater than the saturation temperature (surface superheat). This model uses a time and shape averaged resistance to determine this superheat.
3. The initial diameter of the impacted droplet is determined by multiplying the average impinging diameter by a constant spreading ratio. The spreading ratio is a function of the impacting droplet Weber number, and the wetting characteristics of the surface/fluid combination [32].

4. The surface saturation is low enough such that droplet conglomeration does not occur. This assumption also requires that no excess fluid is sprayed onto the surface.

6.3.2: Model Approach

The approach to the solution of the model is as follows:

1. First the heat flux, q , average impinging droplet diameter, d , and surface saturation, ϵ , are chosen.
2. Next, the initial radius of the wet spot on the surface, $r_d(0)$, and the radius of one unit cell, R , are calculated based on the selected droplet diameter, surface saturation, and spreading ratio, β :

$$r_d(0) = \beta d/2 \quad (6.3.1)$$

$$R = \frac{d\beta}{\sqrt{8\epsilon}} \quad (6.3.2)$$

3. Since the model (as presented later) is nondimensionalized, the nondimensional parameters to be input must be calculated. These are: the Fourier number, Fo , the dimensionless droplet diameter, δ , the dimensionless heat flux, ψ , and the ratio of the unit cell radius to the plate thickness, R/l :

$$Fo = \frac{a_s t_{res}}{R^2} \quad (6.3.3)$$

Where the residence time is:

$$t_{res} = \frac{(d^3/6)(\rho_l \lambda)}{qR^2} \quad (6.3.4)$$

$$\delta = d/R \quad (6.3.5)$$

$$\psi = \frac{q \, l}{k_s T_{\text{sat}}} \quad (6.3.6)$$

where the plate thickness, l , is assumed to be related to the penetration depth:

$$l = 3\sqrt{a_s t_{\text{res}}} \quad (6.3.7)$$

This assumption indicates that the unit cell radius is related to the plate thickness by:

$$R/l = 1/3\sqrt{Fo} \quad (6.3.8)$$

4. The transient conduction problem for the heat conducted through the solid to the evaporating drop is solved using the governing equations and solution scheme which follow. An average dimensionless surface temperature is predicted which is used with the superheat calculation to predict the average surface temperature.

6.3.3: Governing Equations

The governing equations and the boundary conditions as they apply to the problem depicted in Figure 6.3.1 are presented here. Figure 6.3.1 is representative of one unit cell of the surface containing one evaporating droplet (not shown). The conduction problem is only solved in the solid. This is due to the complex nature of the heat transfer within the droplet.

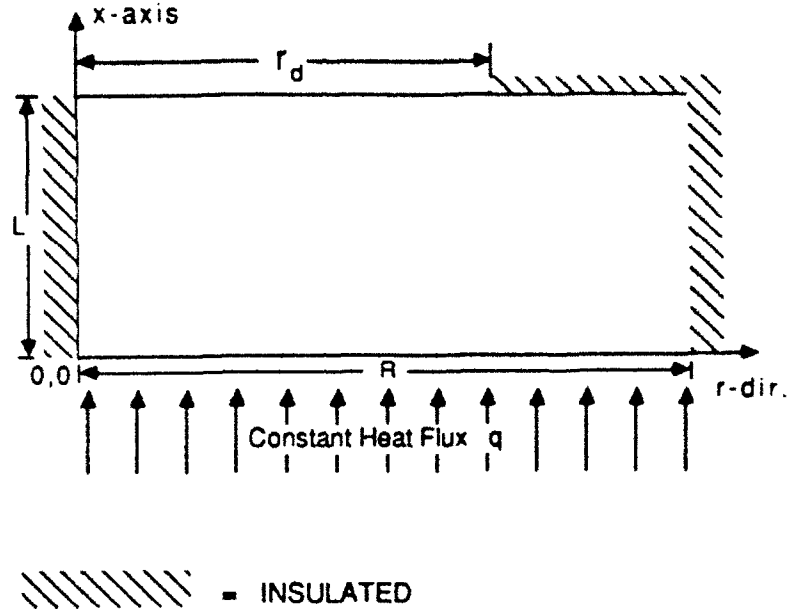


Figure 6.3.1: Model geometry

To account for the surface superheat resulting from conduction through the droplet, a time and shape averaged resistance is used to approximate the surface superheat. After Bonacina et al. [3], the resistance is:

$$R_h = \frac{4/9}{\pi d \beta^2 k_l} \quad (6.3.9)$$

To determine the superheat, this value is simply multiplied by the heat removed by evaporation of the droplet:

$$Q_d = q \pi R^2 \quad (6.3.10)$$

For ease of calculation, the temperature beneath the evaporating droplet ($0 \leq r \leq r_d(t)$, $x = l$) is assumed to remain at the saturation value. Then, the time and area averaged surface temperature is calculated based on the surface temperature profiles predicted from the conduction within the solid. The superheat is then added to this value

to determine the total theoretical average surface temperature. This approach is thought to be acceptable as the model provides accurate predictions of the experimental results as shown later.

The two-dimensional transient conduction equation in cylindrical coordinates is:

$$\frac{\partial^2 T}{\partial r^2} + \frac{1}{r} \frac{\partial T}{\partial r} + \frac{\partial^2 T}{\partial x^2} = \frac{1}{\alpha} \frac{\partial T}{\partial t} \quad (6.3.11)$$

The boundary conditions are:

$$1. \quad \frac{\partial T}{\partial r} = 0, \text{ at } r = 0$$

$$2. \quad \frac{\partial T}{\partial r} = 0, \text{ at } r = R$$

$$3. \quad -k \frac{\partial T}{\partial x} = q, \text{ at } x = 0$$

$$4a. \quad T = T_{\text{sat}}, \text{ at } x = l, r \leq r_d(t)$$

$$4b. \quad \frac{\partial T}{\partial x} = 0, \text{ at } x = l, r > r_d(t)$$

The droplet radius is determined as a function of time by integrating the heat flux at the surface under the droplet and equating it to the evaporation rate.

$$5. \quad \frac{\partial m}{\partial t} \lambda = 2\pi \int_0^{r_d} -k \left. \frac{\partial T}{\partial x} \right|_{x=l} r dr$$

The evaporation rate is then used to determine the decrease in droplet volume. The new radius is determined by assuming that the aspect ratio of the droplet remains constant as the volume decreases.

The governing equation and boundary conditions are then nondimensionalized using:

$$\eta = r/R, \quad \lambda = x/l, \quad \tau = t/t_{\text{res}}, \quad \text{and} \quad \theta = (T - t_{\text{sat}})/T_{\text{sat}}, \quad V = v/R^3$$

The resulting dimensionless equation and boundary conditions are given by:

$$\frac{\partial^2 \theta}{\partial \eta^2} + \frac{1}{\eta} \frac{\partial \theta}{\partial \eta} + \left[\frac{R}{l} \right]^2 \frac{\partial^2 \theta}{\partial \lambda^2} = \frac{1}{\text{Fo}} \frac{\partial \theta}{\partial \tau} \quad (6.3.12)$$

$$1. \quad \frac{\partial \theta}{\partial \eta} = 0, \text{ at } \eta = 0$$

$$2. \quad \frac{\partial \theta}{\partial \eta} = 0, \text{ at } \eta = 1$$

$$3. \quad \frac{\partial \theta}{\partial \lambda} = \psi, \text{ at } \lambda = 0$$

$$4a. \quad \theta = 0, \text{ at } \lambda = 1, \eta \leq \eta_d(\tau)$$

$$4b. \quad \frac{\partial \theta}{\partial \lambda} = 0, \text{ at } \lambda = 1, \eta > \eta_d(\tau)$$

$$5. \quad \frac{\partial V}{\partial \tau} = (\pi/3) \psi \delta^3 \int_0^{\eta_d} \frac{\partial \theta}{\partial \lambda} \Big|_{\lambda=1} \eta d\eta$$

6.3.4: Solution Scheme

The governing equations are solved using the Alternating Direction Implicit solution scheme. The equations are first written in finite difference form using second order accurate central differencing. The finite difference terms at the boundaries are approximated using second order one-sided differences. The equations are written for the first half-time step in the λ -direction (All terms in λ -direction written as unknowns). These equations result in a tridiagonal matrix which is solved using the Thomas Algorithm [34]. These new temperatures are then used in the equations written in the η -direction for the second-half

time step resulting in another tridiagonal matrix. This matrix is then solved to give the new temperature distribution. The heat flux at the surface is then integrated to decrement the droplet radius. The temperatures are then updated and the solution continues. When the drop completely evaporates, a new drop is added and the problem is solved again using the temperature profile at the end of the previous droplet as the initial temperature profile for the new droplet. This continues until the temperature profiles no longer change from one droplet to the next. At this point the surface temperature is integrated over the total area and the lifetime of the droplet and added to the calculated superheat to provide the average surface temperature estimate.

6.3.5: Model Results

The model results were compared to those generated by the ANSYS finite element package for a simplified case. Since it is very difficult to run the problem with time-dependent boundary conditions on ANSYS, it was assumed that the droplet size did not change for the comparison case. It was assumed that the entire heated surface was initially at 100 °C at the onset of heating. The case was run for a plate 1 mm thick and 1 mm in radius with a 0.5 mm radius drop resting on top. For both the ANSYS package and the model, an 11 by 11 grid was assumed. The heat flux to the bottom of the plate was assumed to be 1000 W/cm². The ANSYS results are compared to the model results in Figure 6.3.2 for a time of 0.01 second after the onset of heating. As seen, the maximum variation in the results was less than 2 °C. Both models showed this agreement at all time steps through steady state.

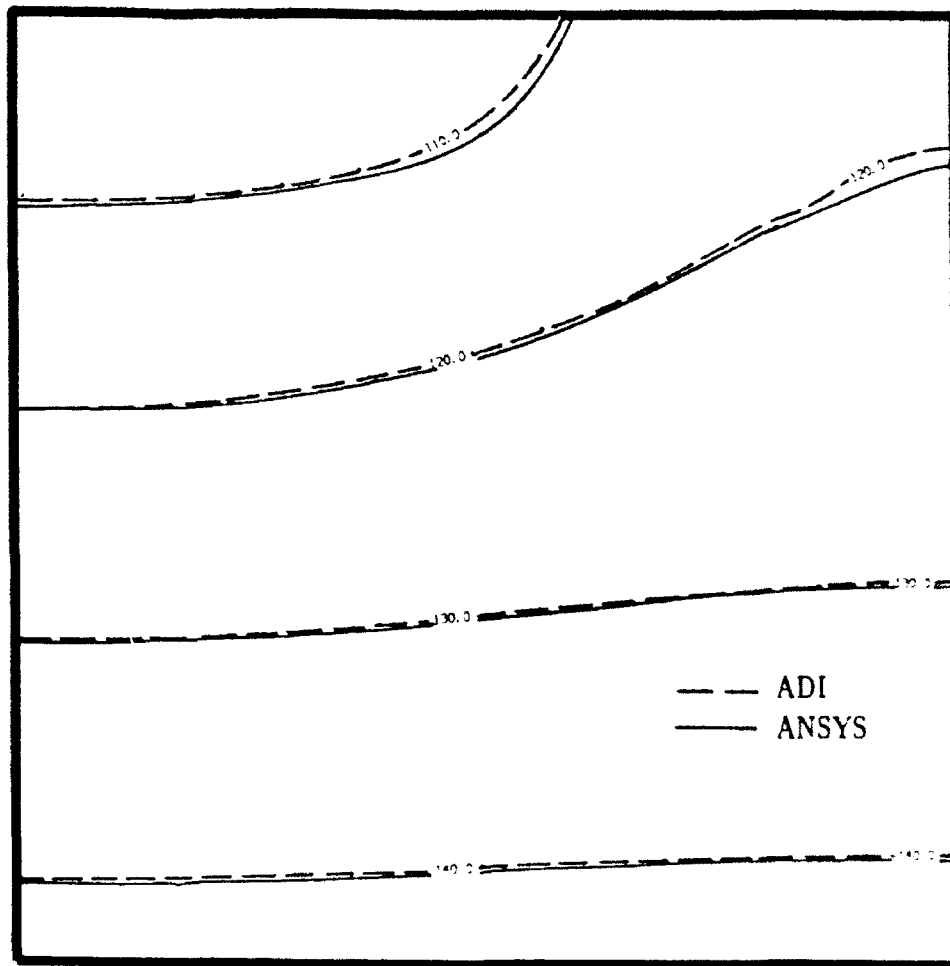


Figure 6.3.2 Model/ANSYS comparison

Before running the cases for comparison with the experiment, a grid study was performed to determine the optimal grid size. Grids of 10 x 10 to 40 x 40 showed little variation in the predicted average surface temperature when the Fourier number was low. However, for high Fourier numbers, the solution became unstable for the course grids. Contour plots are presented in Figure 6.3.3 for a 15 x 15 grid, and a 30 x 30 grid at the end of 20 time steps to show that the results do not change. For this case, $Fo = 1$, $\delta = 0.1$, and $\psi = 0.02$. Even though grids as course as 10 x 10, provided the same results in most cases, all the cases compared to the experiments were run with a 30 x 30 grid to ensure the accuracy of the results, especially for the high Fourier number cases.

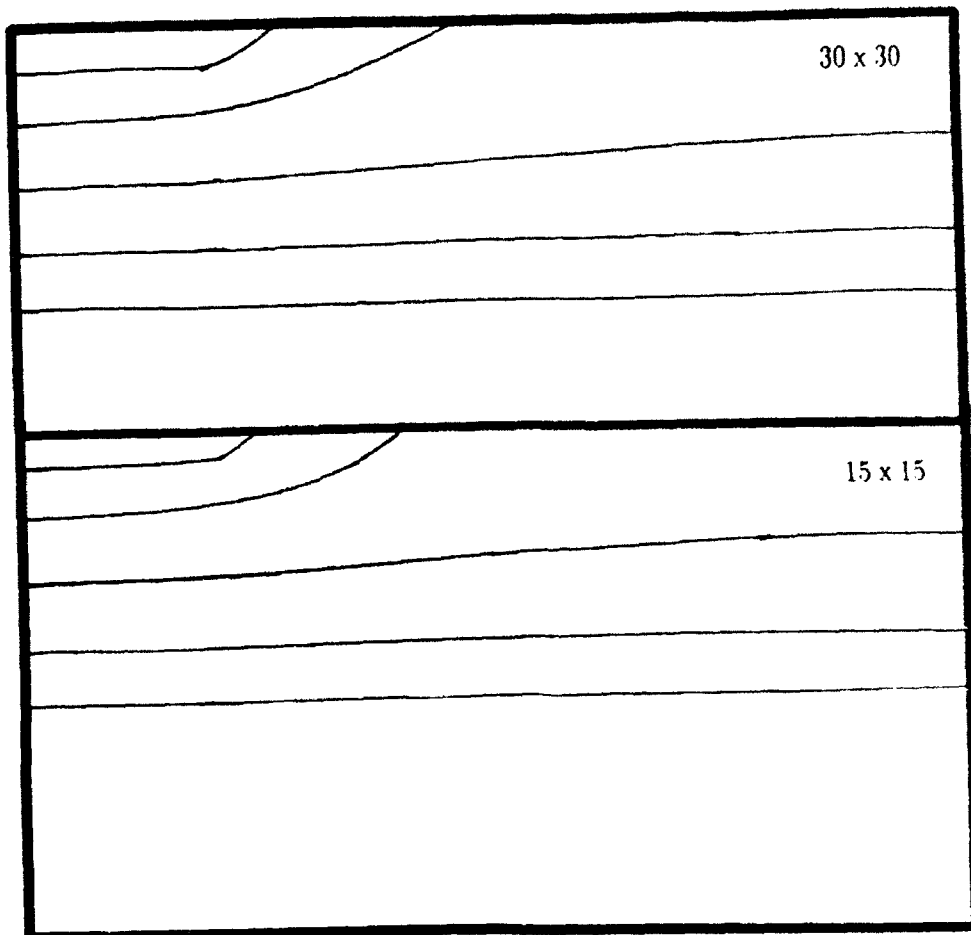


Figure 6.3.3: Grid size comparison

Figure 6.3.4 is plotted to show the dimensionless surface temperature as a function of dimensionless heat flux, for different Fourier numbers and dimensionless droplet diameters. These curves illustrate the extreme importance of the spray characteristics and the liquid distribution on the surface. The results clearly indicate that any changes in surface saturation or droplet diameter have extreme effects on the resulting surface superheat for any given heat flux. It should also be mentioned that the predictions are made under ideal conditions. Any nonuniformity in the liquid distribution on the surface could result in a higher average surface temperature. The same holds true for any variation in droplet diameter.

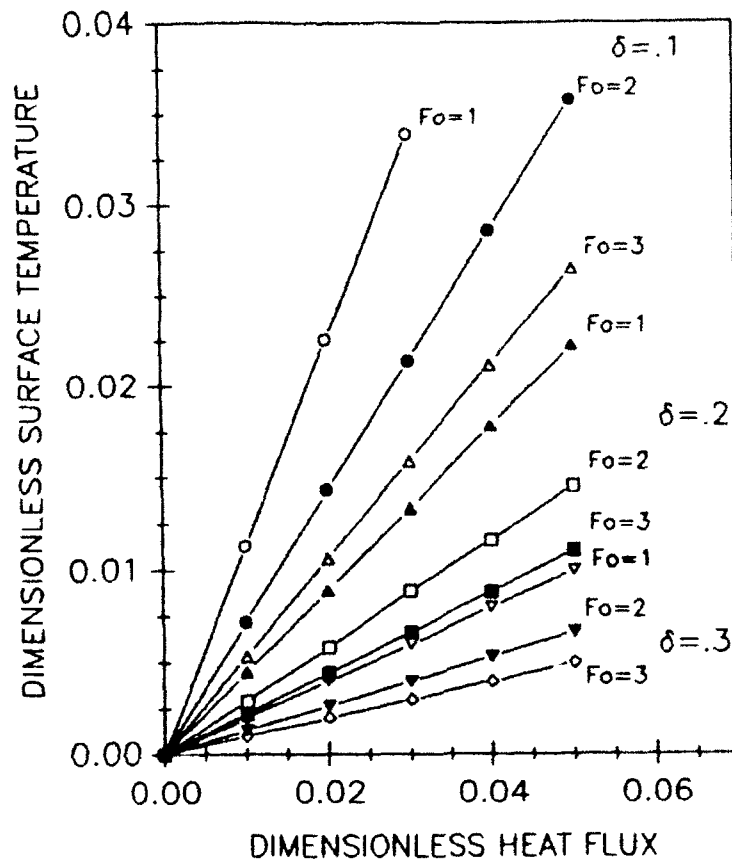


Figure 6.3.4: Dimensionless surface temperature vs. heat flux

These curves can be used to predict the surface temperature for any surface/fluid combination by the following approach.

1. Calculate the Fourier number using equations 6.3.3 and 6.3.4.
2. Calculate the dimensionless droplet diameter using equation 6.3.5.
3. Calculate the dimensionless heat flux using equation 6.3.6
4. Read the value for θ from Figure 6.3.4.

5. Calculate the resistance within the droplet from equation 6.3.9 and the heat transferred to the droplet from equation 6.3.10.
6. The average surface temperature is then given by:

$$T_{\text{surf}} = T_{\text{sat}}(\theta + 1) + R_h Q \quad (6.3.14)$$

For most cases with very high surface thermal conductivity and very low liquid conductivity, the first term in equation 6.3.14 is small compared to the second. Conversely for high thermal conductivity liquids on low thermal conductivity surfaces the second term is small compared to the first.

The main value of the analytical predictions is that they demonstrate the extreme importance of choosing the proper spray characteristics. Spray characteristics should be chosen to provide the smallest possible droplets and the highest possible surface saturation. The liquid should also be distributed as uniformly as possible. The surface saturation must be low enough to avoid droplet conglomeration, and the droplets must be large enough to avoid entrainment in the escaping vapor.

6.4: COMPARISON WITH EXPERIMENTAL RESULTS:

The analytical model predictions are compared to the experimental results presented by Bonacina et al. [3], and to the present experiments. These results are thought to be most applicable because no excess liquid was present and the average surface saturation values were low. The general trends predicted by the model are supported by the experimental data. Table 6.1 shows a comparison of the model and the experimental results. Runs 1 - 8 are the results of Bonacina et al. and runs 9 - 12 are experiments described earlier in Section . The value of ΔT_{exp} was taken from the experimental data. The ΔT_{thr} is predicted by the analytical model. The difference is given in the final column.

Table 6.1: Comparison with experimental data

Run	q W/cm ²	ϵ	d μm	ΔT_{exp} K	ΔT_{thr} K	% Diff
1	49.7	0.045	65	18.0	16.1	10.6
2	64.8	0.188	56	4.5	4.0	9.1
3	109.9	0.195	83	11.9	9.8	17.6
4	142.0	0.054	73	39.4	42.7	8.4
5	215.3	0.196	90	23.9	20.8	13.0
6	141.9	0.049	73	55.4	47.1	15.0
7	168.5	0.081	80	42.8	36.6	14.5
8	209.1	0.128	90	37.7	31.7	15.9
9	60	0.25	124	4.0	5.7	42.5
10	80	0.30	124	5.0	6.3	26.0
11	60	0.30	132	3.0	5.0	66.7
12	140	0.25	132	10.0	14.1	41.0%

The agreement between the model predictions and the experimental data is excellent for the data of Bonacina et al. In general, the surface temperature is underpredicted. This is most likely due to the variation in actual diameters of the individual droplets and nonuniformity in the liquid distribution on the surface.

The comparison between the data from the experiments conducted here is also reasonable. The high surface saturation in these cases results in a very low surface temperature. Therefore, even though the predictions are off by only a few degrees, the percent difference is high. The uncertainty in the experimental data is at least as high as the difference in the model predictions. The complete uncertainty analysis is given in Appendix A.

CHAPTER 7: COMPARISON WITH PREVIOUS RESEARCH

In this chapter, the work of other researchers is compared to the present research. Recall from the introduction that wide variation in the heat transfer results is seen depending on the differences in the spray characteristics. With the knowledge gained from the present research, these works will be readdressed to explain the reasons for the differences.

Very little work has been done in spray cooling with water in the low surface temperature region of interest. More work is available on spray cooling surfaces at temperatures beyond the Leidenfrost point, but this work is not relevant to the present research.

One of the earliest works in spray cooling was done by Toda [1]. In this paper, no prior works in spray cooling are referenced. As mentioned, Toda consistently showed that critical heat fluxes in the 200 to 250 W/cm² range occurred at surface superheats between 30 and 60 °C. Toda stated that at the time of his research there was no accurate way of measuring the droplet velocity. Consequently he used an approximate analytical technique to provide an estimate. According to his estimates, droplet velocities ranged between 50 and 100 m/s. Average droplet diameters were estimated to be between 100 and 200 μm. In this range of droplet diameter and velocity, the Weber number is very high, indicating that droplet disintegration and splashing would definitely be a very important factor. In the present research, with much lower Weber number droplets, up to 10 percent of the fluid was splashed from the surface. Most likely, a much higher percentage was splashed in Toda's research. This may be one of the reasons that a deficiency in liquid supply occurred at a much lower heat flux than with the present research. Also, in most cases, the volume flux of coolant was lower than with the current research.

Based on the findings of the current research, it is believed that the CHF occurred due to a liquid deficiency as described in Chapter 2. The much lower values of CHF are caused by increased splashing and fluid expelled by nucleation. In fact, Toda observed that nucleation was responsible for the destruction of the liquid film. Even though he observed this, he made no conclusions concerning the mechanisms causing

CHF. He did not mention the surface roughness conditions or conduct any study in which the surface conditions were varied.

Toda did attempt to reproduce the heat flux versus superheat curve through analytical modeling. He defined the problem as one of straight conduction in the liquid film, neglecting the influence of impinging droplets and nucleation. To estimate the liquid film thickness, single droplet impingement studies were conducted with low velocity droplets produced with a syringe. A correlation was developed from this study and then assumed to apply to the multiple droplet spray. However, this correlation may be a source of significant error as very thin films are predicted. The present research indicates that the film is much thicker and that straight conduction cannot be responsible for the heat transfer efficiency observed. The present research also suggests that nucleation plays an important role in governing the efficiency. For these reasons, the model of Toda was probably very inaccurate. In fact, after developing the theory, Toda applied empirical constants to match the experimental data. He provided no theoretical basis or explanation of the constants. The reason the definition of the problem as a conduction problem can be used to approximate the data can be seen in Figure 7.1.1. An effective thermal conductivity can be defined as the heat transfer coefficient times the liquid film thickness using Figures 5.1.5 and 5.3.3. As seen, the result is very linear. Using the thermal conductivity of the fluid, and then defining an effective film thickness could still match the experimental data. However, it does not reasonably approximate the physical situation.

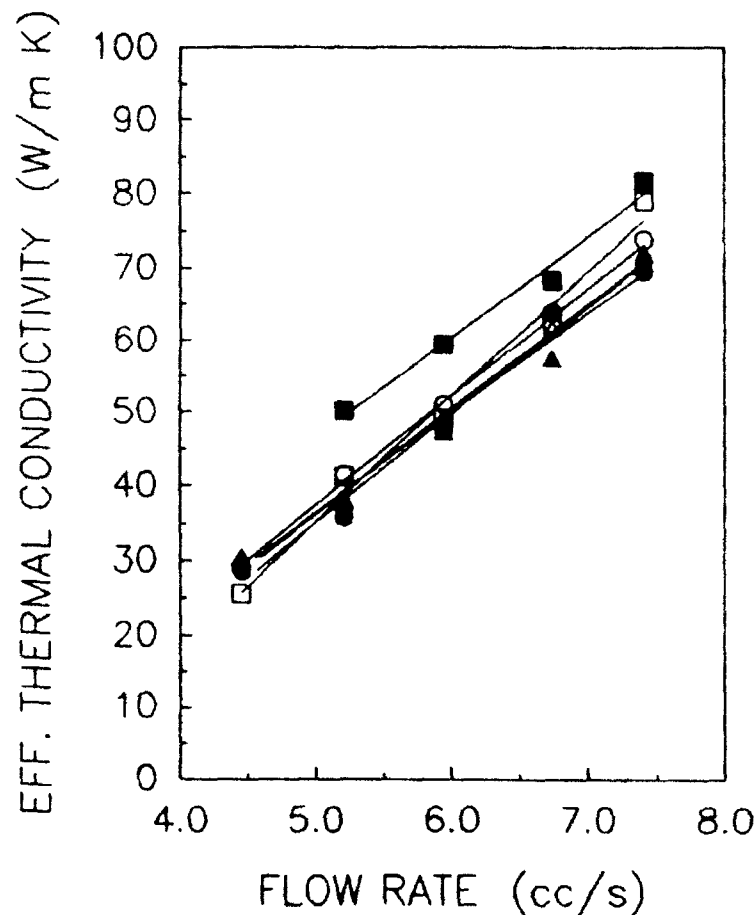


Figure 7.1.1: Effective thermal conductivity

The most comprehensive work in low flow rate spray cooling was conducted by Bonacina et al. in their study of dropwise evaporation [3]. This work has already been discussed in conjunction with modeling presented in Chapter 6. Bonacina was unable to demonstrate heat fluxes very much higher than 200 W/cm^2 due to limitations in the experimental apparatus. The authors postulated, however, that much higher heat removal rates were probably obtainable using the same dropwise evaporation method. The present research tends to indicate that this is not the case for several reasons. First, the average droplet sizes and velocities used in his experiments were approximately 50 to $90 \mu\text{m}$ and 1 to 2 m/s , respectively. These small droplets were ideal for his work because they form very thin wet patches on the surface resulting in very efficient heat transfer. They also have low enough Weber number that no

splashing occurs. However, as the heat flux is increased, these droplets would quickly become entrained in the escaping vapor and never reach the surface as shown in Chapter 2, Figure 2.3.3. To overcome the entrainment problem, and still provide droplets that will not disintegrate upon impact, is very difficult, especially with pressure atomizing nozzles. At any rate, the droplet size and velocity would have to be increased. The modeling in Chapter 6 indicated that if both the heat flux and the droplet size are increased, the surface temperature increases rapidly. The resistance to heat transfer through the droplet to the upper liquid/vapor interface will also increase. This will cause nucleation to occur within the droplet which will cause destruction of the wet patch. Since this will expel fluid, the flow rate will have to be increased beyond what is required for complete evaporation. This will cause droplet conglomeration which intensifies the requirement for excess fluid, thus leading to the flooded surface type spray cooling. Valenzuela has also investigated this type of spray cooling. He postulated, based on modeling and single droplet studies, that the maximum heat flux that could be obtained with no surface flooding was in the 300 to 400 W/cm² range [35]. For his research the droplet diameters and velocities were controlled using piezoelectric drop-on-demand technology.

Monde investigated spray cooling with air atomizing nozzles. The results he obtained were very similar to those presented in the present research [6]. Monde attempted to correlate the data by plotting the critical heat flux against the mass flow rate times an empirical constant. This correlation showed good agreement with the data in the low flow rate region, although there was scatter. The scatter is most likely due to nonuniformity in the liquid supply as was observed in the present research. As the flow rate is increased, the correlation begins to show marked departure from the experimental data. This can be explained considering the present research.

In the low flow rate region, the CHF is caused by liquid deficiency resulting from nucleation within the liquid film. Recall from Chapter 2, that liquid flow rates up to 10 times the mass flow rate of vapor generated through nucleation can be expelled. Monde observed the expulsion resulting from nucleation but did not discuss the possible

effect on the CHF. He did mention that at low heat fluxes very little nucleation was observed. This is probably because the heat transfer was efficient enough that the low heat flux could be totally removed by evaporation at the upper liquid/vapor interface. Consequently, only 20 percent excess fluid was required to remove all the heat at the critical heat flux. As the flow rate is increased, the surface temperature and the heat flux both increase. As the surface temperature increases, the percentage of heat removed by nucleation increases rapidly as discussed in Chapter 5. This causes a proportionately greater increase in flow rate to obtain an increase in critical heat flux. This continues until the until the mechanism for CHF gradually changes to the mechanism described in conjunction with the high flow rate cases. Monde investigates flow rates even higher than those in the present research, but the CHF actually ceases to increase as the flow rate is increased. This is probably because as the flow rate is increased with air atomizing nozzles, the droplets get bigger instead of smaller as with pressure atomizing nozzles. Therefore, the impingement frequency may not increase sufficiently to obtain further increase in CHF.

Pais et al. also investigated spray cooling with air atomizing nozzles [4,5]. This work differs from that of Monde considerably. The main distinction is that Pais et al. used much higher air flow rates and lower liquid flow rates. As a result the droplets had smaller size and higher velocity. Also, the higher air flow rates provided a strong stagnation flow field which served to thin the liquid film and sweep away the vapor. This has the benefit of improving heat transfer efficiency in two ways. The first is that the thinner film provides less resistance to heat transfer to the upper liquid/vapor interface. The second is that the partial pressure of the vapor at the interface is reduced thus lowering the temperature at which evaporation occurs. Consequently, Pais et al. were able to demonstrate a critical heat flux greater than 1000 W/cm^2 with much lower surface superheats. In the latter paper, they investigated the effects surface roughness. When the surface was polished to mirror finish, nucleation was completely suppressed. This reduced the film thickness giving even further improvement in efficiency. Thus, they were able to remove comparable heat fluxes at surface temperatures below 100°C . This provided further

evidence of the effectiveness of vapor removal by the air stagnation flow field. Another reason the air atomizing nozzles provide such high critical heat flux is that the spray cone is much more well suited to spray cooling. Unlike pressure atomizing nozzles, the volume flux is highest in the center of the spray and reduces radially outward. Thus, the critical heat flux transition started at the outer edge and propagated radially inward. As the flow rate is increased, more fluid on the surface flows radially outward thus suppressing transition. With pressure atomizing nozzles, as the flow rate is increased, often times the center of the spray becomes more hollow.

The only real drawback to spray cooling with this type of nozzle is that it is not suitable for application in closed systems. This is because the condensation temperature and heat transfer coefficient are both greatly reduced by the addition of noncondensable gases.

In conclusion, none of the previous researchers have successfully been able to model the complex heat transfer and fluid flow phenomena associated with spray cooling. In fact, none have even attempted to describe the critical heat flux phenomena, other than to state observations. Correlations have been attempted but do not accurately represent the physical phenomena and, therefore, are not applicable over a wide range of spray or surface conditions. The phenomenological modeling and the analysis of the present research have enabled understanding and explanation of the wide range of results.

CHAPTER 8: CONCLUSIONS AND RECOMMENDATIONS

The research has provided an in depth investigation into the spray cooling heat transfer process. This chapter summarizes the important conclusions which can be drawn from the experimental results and analysis. Recommendations for future research are given so that the understanding can be further improved. There is still significant uncertainty in many of the important phenomena. Experiments which may provide clearer understanding and more detailed information are proposed.

8.1: CONCLUSIONS

The main goal of the research was to provide a fundamental understanding of spray cooling surfaces at a temperature between the saturation point, and the Leidenfrost point. The research has focused on identification of the important factors governing the heat transfer process. The main body of the research concerned determining the effects of spray characteristics. However, the effects of surface roughness, noncondensable gases, and liquid subcooling were also investigated.

The research indicated that the heat transfer differs greatly depending on the coolant flow rate. The very low flow rate range, in which the coolant flow rate is matched to the heat removal requirement (no excess fluid), is characterized by dropwise evaporation from isolated wet patches on the surface. This range of interest was investigated in Chapter 6. Analytical modeling was conducted and compared to experimental results with good agreement. It was shown that the heat transfer coefficient was highly dependent on the spray characteristics. To maximize the heat transfer coefficient, it is important to minimize the size of the impinging droplets and maximize the percent of wet surface area. Smaller droplets yield thinner liquid films on the surface for a given volume of fluid. This reduces the resistance to heat transfer within the droplet and improves heat transfer. Also, heat transfer at the perimeter of the droplet, where

the liquid/vapor interface contacts the solid surface is very efficient. Smaller droplets also maximize the perimeter contact area for a given volume of fluid. It is also very important to maximize the percent of wet surface area, while providing a uniform liquid distribution on the surface. This reduces the temperature gradients due to transient conduction in the surface. Since the average surface heat flux is actually removed through the wet patches only, increasing the percent of wet surface area reduces the heat flux to the individual droplets. Therefore, the superheat due to resistance within the droplet is also reduced.

The critical heat flux for these cases is not a well defined concept. Of course, if a quantity of heat is supplied to the surface which is greater than the flow rate can remove if it is completely evaporated, the surface dries out. This is not necessarily the maximum though, because the flow rate can also be increased. As the heat flux and flow rate are increased, the droplet size and velocity must also be increased to avoid entrainment in the escaping vapor. This leads to droplet conglomeration and surface flooding. The surface temperature also increases, thus increasing nucleation within the wet patches. The nucleation causes fluid to be expelled from the surface thus requiring excess fluid to be supplied. Therefore, the critical heat flux does not actually occur but the mechanism of heat transfer changes to the low flow rate flooded surface type heat transfer.

This low flow rate flooded surface range was investigated in Chapter 2. For this study detailed measurements of the spray characteristics were taken using a laser phase Doppler system. These measurements indicated that the critical heat flux results from a deficiency in liquid supply which results from droplet entrainment, splashing, and liquid expulsion. Entrainment occurs when the droplets lack sufficient momentum to overcome the escaping vapor and reach the surface. For the tests conducted here, only a very small percentage of the overall volumetric flow rate was entrained. However, with some nozzles, this may be a dominant effect. The PDPA measurements also indicated that splashing of fluid from the surface occurred. However, when no heat was supplied, the percentage of the volumetric flow rate splashed was also small. Again, with some nozzles, this effect may be

very important as was thought to be the case with the research of Toda [1]. It was seen that droplet expulsion was the dominant effect. When nucleating bubbles burst within a thin liquid film, fluid is expelled from the surface. It was seen that the mass flow rate of liquid expelled can be as much as 10 times greater than the mass flow rate of vapor generated through nucleation. Based upon the PDPA measurements, the heat removal capability of the spray was plotted against the heat flux. This plot indicated that the CHF occurs when the heat flux surpasses the heat removal capability of the spray, not expelled, splashed, or entrained. This work indicated that proper choice of spray characteristics is vital to obtaining high heat flux. The droplet diameter and velocity must be supplied in a range that avoids entrainment and splashing. Since fluid is expelled by nucleating bubbles, it is also suggested that the surface conditions should suppress, rather than enhance, nucleation. This is contrary to efforts directed towards heat transfer enhancement in other areas of phase change heat transfer.

Finally, Chapters 4 and 5 dealt with the high flow rate range of spray cooling. For these tests, the flow rate is increased to a point such that no deficiency can result from expulsion, splashing and entrainment. For these tests, a new apparatus was designed so that various other important effects could be analyzed, such as liquid subcooling, noncondensable gases, and surface roughness. This testing and analysis indicated that the CHF occurs when the vapor generation rate on the surface becomes so high that a vapor barrier is formed in a given region in the time interval between successive impinging droplets. The analysis of the spray characteristics indicated that the CHF is proportional to the impingement frequency. This is because, increasing the impingement frequency decreases the time available for the formation of the vapor barrier.

The research also indicated that the surface roughness plays a dominant role in the heat transfer. Rougher surfaces provide many more nucleation sites at a given surface temperature. Although this improves the heat transfer coefficient, it has a very negative effect on the CHF. This is because the vapor generation rate is proportional to the number of active nucleation sites.

The research also indicated that the heat transfer efficiency is strongly dependent on the spray characteristics. The analysis indicates that mixing caused by droplet impingement is responsible for the very high heat transfer coefficients. This indicates that the efficiency should also improve with increasing impingement frequency. However, efficiency also should decrease with increasing film thickness. The exact relationships between the spray characteristics and the efficiency cannot be well defined, but the trends are well predicted by analyzing the important phenomena.

Phenomenological modeling was conducted to explain the important effects so that the trends in the experimental data could be understood. The modeling predicts the trends in the experimental data very well. Although, many cases which do not match are seen to occur due to nonuniformity in the spray cone.

The modeling and analysis are also used to explain the results obtained by other researchers. No previous researcher has effectively modeled or explained the physical phenomena. This is partially due to the limited scope of the measurements and experiments conducted. The present research has provided much more detailed measurements and analysis than any previous research. The experiments were also conducted over a wider range of experimental conditions. Consequently, a more fundamental understanding of the heat transfer process and the important governing factors has been obtained. Now that this understanding is advanced, more detailed experiments must be conducted under very controlled conditions to provide further verification of the postulated heat transfer mechanisms, and to better define the complex interaction between the impinging droplets and the liquid film. Future research is recommended in the following section to provide further understanding.

8.2: RECOMMENDATIONS

As mentioned, there is still much to be investigated before spray cooling can be completely understood. Future research should focus on more detailed determination of the data which could only be estimated here. The laser phase Doppler measurements of the spray characteristics provided invaluable information. However, measurements were only obtained over a very small range of experimental conditions. These measurements should be repeated over a wider range of conditions. For example, measurements should be taken with saturated closed-system tests. This would eliminate some of the uncertainty in the analysis presented in Chapter 2, and provide more detail for the analysis presented in Chapter 5.

For the Chapter 2 analysis, there would be less uncertainty in the estimate for the percentage of heat removed by nucleation. Also, the bubble nucleation frequency could be estimated using the surface roughness and bubble growth models presented in Chapter 5, and compared to the measured expulsion frequency. This could be done under controlled surface roughness conditions for the same spray characteristics. This would help to determine the validity of the bubble nucleation and growth models.

The laser phase Doppler measurements also give an accurate estimate of the volume flux distribution, and the droplet diameter distribution. From this information, the impingement frequency could be accurately calculated as a function of radial position. This would allow more detailed analysis of the effects of variation in spray cone uniformity which is one of the most important parameters for high efficiency and critical heat flux. This would also allow more accurate definition of the relationship between impingement frequency and critical heat flux.

Another improvement could be made in the area of liquid film thickness determination. It would be ideal if the liquid film thickness as a function of radial position could be measured by a nonintrusive technique. If this was done, as the heat flux to the surface is increased, this would help to determine the vapor generation rate through nucleation. Vapor generated within the liquid film will cause the film thickness to increase. If these measurements were conducted

simultaneously with the PDPA measurements, the expulsion and impingement mass fluxes would also be known. Therefore, an accurate estimate of the liquid film thickness and velocity could also be made.

One of the most uncertain areas is the interaction between an impinging droplet and the vapor bubbles growing within the liquid film. This may best be investigated by single droplet studies with very controlled conditions. The droplet diameter and velocity and liquid film thickness would have to be controlled. Then, the region of nucleation sites which are destroyed by an impinging droplets could be investigated photographically. During actual spray cooling tests it is virtually impossible to photograph the phenomena in the liquid film due to the high vapor generation rate and the liquid droplet spray. The phenomena occur in such short time intervals that very high intensity lighting is required for such short exposure times. The droplets and vapor scatter the light causing the picture to wash out. If new visualization and photography techniques could be developed, the description of the physical phenomena could be greatly improved.

The single droplet type studies could also be used to investigate splashing from the liquid film. As seen from the studies by Toda, the droplet velocity cannot be increased indefinitely without having adverse effect on the heat transfer [1]. After some point, the liquid film cannot absorb the kinetic energy of the droplet upon impact and splashing occurs. More detailed information concerning splashing would help to define the best range of droplet diameter and velocity. The entrainment predictions given in Chapter 2 help to provide the lower limit of diameter and velocity range, but there is still uncertainty concerning the upper limit of the suitable range.

The single droplet studies could also be used to investigate the phenomena of secondary nucleation caused by an impinging droplet. Nucleation could be observed as a function of the liquid film thickness, surface temperature, and droplet diameter and velocity. This type of study would enhance the understanding of the critical heat flux phenomena because a more accurate estimation of the vapor generation rate in the liquid film could be obtained. Similar studies could be conducted to determine secondary nucleation effects resulting from bursting bubbles to further improve the estimate. If new bubbles are

created every time a bubble bursts, this could be the dominate source of bubbles.

It would also be very useful if a technique to measure very localized surface temperature could be developed. The measurements must have very fast response, and resolution as high as $10\text{ }\mu\text{m}$ in order to obtain meaningful data. If this type of measurement could be taken, it would help to determine characteristics of nucleation. It is unknown if the microlayer dries out between bubbles as it does in pool boiling. It is thought that since the bubble growth period is so much shorter that it does not. This type of measurement would also help determine if a bubble waiting period exists as it does in pool boiling. If the microlayer does not dry out, the waiting period may be significantly reduced. Also, it is unknown if impinging droplets completely penetrate the microlayer and force the superheated fluid to mix with the bulk as postulated. If this does happen, detailed temperature measurements would show a temperature depression upon droplet impact.

It would also be very useful if detailed size and velocity measurements of expelled liquid droplets could be related to the size of the bursting bubble, and the thickness of the liquid film. This type of measurement would aid in the development of an expulsion model so that the CHF for lower flow rate cases could be more accurately predicted.

Many improvements in measurement and analysis have been mentioned that would enhance the understanding of spray cooling. However, based on the present analysis and measurements, there are many improvements which could be made with the intent of increasing the critical heat flux and improving efficiency. For example, it has been demonstrated that spray cone uniformity has a tremendous effect on the heat transfer. The nozzles which are currently commercially available are not well suited to spray cooling. After further analysis is used to defined the most ideal spray conditions, nozzles specifically designed to meet the requirements of spray cooling should be designed. The nozzles should maximize the impingement frequency at a given flow rate, while providing droplets in a diameter and velocity range which avoids entrainment and splashing. Care must be taken to ensure that the volume flux is high in the center of the spray. The center is critical because fluid generally flows radially outward. If the volume flux is low, fluid is actually

induced to flow inward. There is no place for it to go so it piles up and then periodically dissipates in an unsteady manner. The increased film thickness and low impingement frequency in the center cause early transition to a nonwetting condition.

The present research has indicated that there are still many areas which need to be further researched to provide a better understanding. The fluid flow and heat transfer phenomena are so complex because of the random nature of the spray and the interrelationships between the nucleation and impingement phenomena. When these relationships are more well defined through future research, it will be possible to provide more accurate predictions of the critical heat flux and heat transfer coefficient which will result from a given set of spray and surface conditions.

9. REFERENCES

1. Toda, S., "A Study of Mist Cooling," Heat Transfer-Japanese Research, Vol. 1 (3), p. 39-50, 1972.
2. Eastman, G.Y., Ernst, D.M., "High Power Density Evaporative Cooling (HIPDEC)," Final Report, Air Force Weapons Laboratory, Kirtland AFB, NM, September 1982.
3. Bonacina, C., Del Guidice, S., Comini, G., "Dropwise Evaporation," Journal of Heat Transfer, Vol. 101, p. 441-446, 1979.
4. Pais, M.R., Tilton, D.E., Chow, L.C., and Mahefkey, E.T., "High-Heat-Flux, Low-Superheat Evaporative Spray Cooling," AIAA Paper AIAA-89-0241, 27th Aerospace Sciences Meeting, January 1989.
5. Pais, M.R., Chow, L.C., and Mahofkey, E.T., "Surface Roughness and Its Effects on the Heat Transfer Mechanism in Spray Cooling," ASME Paper, Winter Annual Meeting, San Francisco CA, December 1989.
6. Monde, M. "Critical Heat Flux in the Saturated Forced Convection Boiling on a Heated Disk with Impinging Droplets," Trans. JSME, Vol. 45, No.394, pp 849-858, 1979.
7. Bachalo, W.D., and Houser, M.J., "Development of the Phase/Doppler Spray Analyzer for Liquid Drop Size and Velocity Characterization," AIAA Paper No. AIAA-84-1199, 20th Joint Propulsion Conference, Cincinnati, Ohio, June 1984.
8. Ueda, T., Inoue, M., and Nagatome, S., "Critical Heat Flux and Droplet Entrainment Rate in Boiling of Falling Liquid Films," Int. Journal of Heat and Mass Transfer, Vol. 24, pp. 1257-1266, 1981.
9. Garner, F.H., Ellis, S.R.M., and Lacey, J.A., "The Size Distribution and Entrainment of Droplets," Transactions of the Institution of Chemical Engineers, Vol. 32, pp. 222-235, 1954.
10. Newitt, D.M., Dombrowski, N., and Knelman, F.H., "Liquid Entrainment: 1. The Mechanism of Drop Formation from Gas or Vapour Bubbles," Transactions of the Institution of Chemical Engineers, Vol. 32, pp. 244-261, 1954.
11. Manual on the Use of Thermocouples in Temperature Measurement, ASTM Special Publication 470A, Omega Press, Stamford CT. 06907, 1974.
12. Parikh, P.G., Hernan, M.A. Sarochia, V. and Yavrouian, A.H., "Measuring Liquid Drops in Gas Flow," NASA Tech Briefs, p. 79, October 1988.
13. Blevins, R.D., Applied Fluid Dynamics Handbook, Van Nostrand Reinhold Co., New York, p. 192-201, 1984.

14. Lawson, J.D., Phillips, B.C., Circular Hydraulic Jump, Journal of Hydraulic Engineering, Vol 109, p. 505-518, 1983.
15. Khalifa, A.M., McCorquodale, J.A., "Radial Hydraulic Jump," ASCE Journal of the Hydraulics Division, Vol 105, p. 11065-1079, 1979.
16. Udombioresuwan, A., Mesler, R., "The Enhancement of Nucleated Boiling by Foam," Int. Heat Transfer Conference, 1986.
17. Carroll, K., Mesler, R., "Bubble Nucleation Studies, Part II: Bubble Entrainment by Drop-Formed Vortex Rings," AIChE Journal, Vol. 25, p. 853-856, 1981.
18. Brown, W.T., "Study of Flow Surface Boiling," PhD Thesis, M.E. Dept., M.I.T, 1967.
19. Corty, C. Foust, A.S., "Surface Variables in Nucleate Boiling," AIChE Chemical Engineering Progress Symposium Series, Vol. 51, p. 13-19, 1955.
20. Gaertner, R.F., "Distribution of Active Sites in Nucleate Boiling of Liquids," AIChE Chemical Engineering Progress Symposium Series, Vol. 59, p. 52-61, 1963.
21. Kurihara, H.M., Myers, J.E., "The Effects of Superheat and Surface Roughness on Boiling Coefficients," AIChE Journal, Vol. 6, p. 83-91, 1960.
22. Shoukri, M. Judd, R.L., "Nucleation Site Activation in Saturated Boiling," Journal of Heat Transfer, February, p. 93-98, 1975.
23. Forster, H.K., Zuber, N., "Growth of a Vapor Bubble in a Superheated Liquid," Journal of Applied Physics, Vol. 25, p. 474-478, 1954.
24. Sernas, V. Hooper, F.C., "The Initial Vapor Bubble Growth on a Heated Wall During Nucleate Boiling," Int. Journal of Heat and Mass Transfer, Vol 12, p. 1627-1639, 1969.
25. Mikic, B.B., Rohsenow, W.M. Griffith, P., "On Bubble Growth Rates," Int. Journal of Heat and Mass Transfer, Vol 13, p. 657-666, 1970.
26. Mesler, R., Mailen, G., "Nucleate Boiling in a Thin Liquid Film," AIChE Journal, Vol. 23, p. 954-957, 1977.
27. Bergman, T., Mesler, R., "Bubble Nucleation Studies, Part I: Formation of Bubble Nuclei in Superheated Water by Bursting Bubbles," AIChE Journal, Vol. 25, p. 851-853, 1981.
28. Toda, S., Uchida, H., "Study of Liquid Film Cooling with Boiling and Evaporation," Heat Transfer-Japanese Research, Vol. 2, p. 44-62, 1973.

29. Katto, Y., Kunihiro, M., "Study of the Mechanism of Burn-Out in Boiling System of High Burn-Out Heat Flux," JSME Bulletin, Vol. 16, p. 1357-1366, 1973.
30. Monde, M., "Critical Heat Flux in Saturated Forced Convection Boiling on a Heated Disk with an Impinging Jet," Journal of Heat Transfer, Vol. 109, p. 991-996, 1987.
31. Monde, M. Katto, Y., "Burnout in a High-Heat Flux Boiling System with an Impinging Jet," Int. Journal of Heat and Mass Transfer, Vol 21, p. 295-305, 1978.
32. Kurabayashi, T., Karasawa, T., Iida, K., "Impact of Liquid Droplets on a Solid Surface," Preprint # 175, JSME, p. 153-156, 1967.
33. Rizza, J.J., "A Numerical Solution to Dropwise Evaporation," Journal of Heat Transfer, Vol. 103, p. 501-507, 1981.
34. Ames, W.F., Numerical Methods for Partial Differential Equations, Barnes & Noble, New York, 1969.
35. Valenzuela, J., Personal Communication, Creare, New Hampshire, October 1989.
36. Holman, J.P., Experimental Methods for Engineers, McGraw Hill, New York, 1978.
37. Switzer, G., Personal Communication, Systems Research Laboratory, Dayton, Ohio, June 1987.

APPENDIX A

Uncertainty analysis

Appendix A, is a complete uncertainty analysis associated with the present research effort. Appendix B, provides a description of the integral thermocouple measurement technique, and the method of thermocouple reading correction. Appendix C gives experimental results. A table of values, which is often referenced in the text, and the corresponding plots of heat flux versus surface temperature are provided.

A.1: UNCERTAINTY ANALYSIS

The uncertainty analysis for the experiments and calculations is presented in order by chapter. All uncertainty calculations use the standard method of uncertainty calculation unless otherwise specified. The standard uncertainty in a parameter, y , where y is a function of x_1 , x_2 , x_3 , etc. is given by equation A.1.1 [36]:

$$\frac{w_y}{y} = \left[\left(\frac{\partial y}{\partial x_1} w_{x_1} \right)^2 + \left(\frac{\partial y}{\partial x_2} w_{x_2} \right)^2 + \left(\frac{\partial y}{\partial x_3} w_{x_3} \right)^2 + \dots \right]^{1/2} \quad (\text{A.1.1})$$

Chapter 2:

The uncertainty in the volumetric flow rate as read from the rotometer is estimated to be ± 0.21 cc/s. The uncertainty in the nozzle operating pressure is estimated to be ± 2.0 psig, as read from the bourdon tube gage.

The heat flux and surface temperature are estimated using Fourier's Law of Conduction. To determine the uncertainty in the heat flux and surface temperature measurement, the following data are necessary.

Thermal conductivity of copper:	3.89 W/cm K, ± 0.05 W/cm K
Accuracy of thermocouple readings:	± 2.0 °C

Temperature difference between thermocouples:	160 °C, ± 2.8 °C
Distance between thermocouples:	0.635 cm \pm 0.05 cm
Distance between upper TC and surface:	0.318 cm \pm 0.025 cm

The uncertainty in the thermal conductivity of copper results from the variation in thermal conductivity with temperature. The accuracy of the thermocouples is estimated based on manufacturer specifications and limitations of the D/A system. The uncertainty in temperature difference is calculated using equation A.1.1. The distance between the thermocouples is uncertain because it is unknown where in the drilled hole, the bead contacts the copper. The uncertainty is therefore equal to the diameter of the hole in which the thermocouple is placed. The uncertainty in the distance between the upper thermocouple and the surface is equal to the radius of the hole in which the thermocouple is placed. Using the above estimates in equation A.1.1 gives an uncertainty in heat flux of 8.1 percent, at 1000 W/cm². The uncertainty in the extrapolation of the surface temperature is then 10 °C.

The uncertainty in the laser phase Doppler measurements are determined from calibrations [37]. The uncertainty in the droplet velocity is below 5 percent for droplet velocity greater than ± 4.0 m/s. For velocity lower than 4.0 m/s, the uncertainty increases rapidly to as high as 30 percent for very low velocity. The uncertainty in the diameter measurement is also less than 5 percent. The volume flux is estimated to be accurate to within 10 percent. However, comparison with the overall volumetric flow rate was better than this.

Chapter 3:

The uncertainty in the heat flux and temperature measurement with the new apparatus is not as high as with the old apparatus. The analysis is complex due to the method of thermocouple calibration described in Appendix B. A simplified estimate gives a conservative bound. For this estimate, the following data are necessary;

Thermal conductivity of copper:	3.90 W/cm K, ± 0.01 W/cm K
Thermal conductivity of constantan	0.2112 W/cm K, ± 0.005 W/cm K

Accuracy of thermocouple readings:	$\pm 2.0\text{ }^{\circ}\text{C}$
Temperature difference between thermocouples:	$77\text{ }^{\circ}\text{C}, \pm 2.8\text{ }^{\circ}\text{C}$
Distance between thermocouples:	$0.0162\text{ cm} \pm 0.0005\text{ cm}$
Distance between upper TC and surface:	$0.0508\text{ cm} \pm 0.0005\text{ cm}$

The above data give an uncertainty in heat flux of 5.3 percent, at a heat flux of 1000 W/cm^2 . The resulting uncertainty in surface temperature prediction is $2.2\text{ }^{\circ}\text{C}$ (compared to $10\text{ }^{\circ}\text{C}$ with the previous apparatus).

To calculate the uncertainty in the droplet diameter and velocity measurements, the following data are required:

Pixel resolution	
horizontal	$8.5\text{ }\mu\text{m/pixel} \pm 0.5\text{ }\mu\text{m/pixel}$
vertical	$10.0\text{ }\mu\text{m/pixel} \pm 0.5\text{ }\mu\text{m/pixel}$
Distance between droplet images	$\pm 2\text{ pixel} = \pm 20\text{ }\mu\text{m}$
Time between exposures	$20\text{ }\mu\text{s} \pm 1\text{ }\mu\text{s}$

From this data, the uncertainty in droplet velocity at a velocity of 10 m/s is 1.1 m/s or 11 percent.

The uncertainty in droplet diameter is due to scattering of light. The exact perimeter of the droplet may be overestimated by 1 pixel. This gives an uncertainty in diameter of $\pm 20\text{ }\mu\text{m}$.

Chapter 4:

In Chapter 4, the only uncertainty estimate not already given is in the pump flow rates. The pump flow rates were calibrated using a graduated cylinder and a stop watch. The uncertainty in the measured volume was $\pm 2\text{ cc}$. The uncertainty in the time is $\pm .5\text{ s}$. This gives an average uncertainty of approximately $\pm 0.2\text{ cc/s}$. However, the fluctuations in pump output may cause uncertainty somewhat beyond this value. The maximum variation in pump flow rate at a given setting that was observed was less than 0.4 cc/s .

Chapter 5:

In Chapter 5, there is uncertainty associated with the experiments conducted to determine the percent of fluid splashed from the surface, and the thickness of the liquid film. There is also uncertainty associated with some of the estimates used in the modeling and analysis.

The percent splashed was measured using a graduated cylinder and a stop watch. Therefore, the uncertainty is the same as for the flow rate measurement. This gives an uncertainty of 3.8 percent in the amount splashed, at the highest flow rate (nearly 10 percent of the impinging fluid is splashed from the surface). For all nozzles, the variation in percent splashed was less than 20 percent. This is less than the uncertainty estimate.

The uncertainty in the measurement of the film thickness is less than the uncertainty due to the effects of vapor generation within the film, and variation of spray cone uniformity. At a mass flow rate of 7.0 g/s, if the uncertainty in the measurement of the radius of the jump is ± 2 mm, and the thickness of the film is ± 200 μm , equations 5.1.3 and 5.1.4 can be used in the standard uncertainty analysis. This gives an uncertainty in film thickness of ± 31 μm . However, this estimate does not include the uncertainty due to shear losses, or in the simplification of the equations. This provides an additional uncertainty of ± 10 percent from the equation simplification, and 10 percent from neglecting the shear loss, or 60 μm . These measurements are at least useful for explanation of the trends in the data as stated in the text.

In the modeling, the prediction for the number of active nucleation sites is very uncertain. The number of active sites is a strong function of the surface roughness. It is not known how closely the surface roughness conditions match those of the reference from which the prediction was taken. Also, the shape of the thermal boundary layer in spray cooling could differ from that in pool boiling. However, as a microlayer exists in both cases, the difference in the number of active nucleation sites may not be too great. Even with the high uncertainty, this estimation helps to explain the physical phenomena and the trends in the experimental data.

There is also significant uncertainty in the bubble growth rate model proposed. The model has never been experimentally verified in the initial periods of bubble growth, which is the region of interest in spray cooling. Also, the different shape of the thermal boundary layer may also affect the growth rate. However, since the heat for bubble growth is predominantly conducted through the thin microlayer, the difference may not be too great.

The uncertainty in the heat flux removed by nucleation results from the uncertainty in the number of active nucleation sites, and the bubble growth rates as already mentioned, and the high uncertainty in the impingement frequency. There may also be significant uncertainty due to the effects of secondary nucleation. The model should provide an order of magnitude estimate.

Chapter 6:

The uncertainty in the experiments conducted in Chapter six is high as mentioned, for two reasons. First, the apparatus was designed for high flux testing, an uncertainty analysis similar to that for Chapter 3, with a heat flux of 100 W/cm^2 gives an uncertainty of 37 W/cm^2 in heat flux and 2.1°C in Surface temperature. The theoretical predictions match the experimental results within this uncertainty. The uncertainty in the percent of wet surface area measurements may also be high due to error in choosing the proper cutoff value for the pixel intensity. It is estimated that the wet patch perimeter is accurate to within ± 2 pixels. The average wet patch diameter was about $600 \mu\text{m}$. This gives an uncertainty in percent saturation of 14 percent.

The uncertainty in the numerical technique for the modeling is far lower than the uncertainty associated with the model assumptions. The numerical technique is second order accurate. As shown in Chapter 6, the results compare well with those of the ANSYS prediction. The uncertainty in the model comes from variation in droplet diameter and liquid distribution on the surface. For modeling purposes, both are assumed to be ideal. The results indicate that diameter and percent of wet area both have a strong effect on the resulting surface temperature. However, since the effects of larger diameter wet patches

are canceled out by the effects of smaller diameter wet patches, the average diameter should provide a reasonable approximation. The same goes for spatial variation in the surface wetness. It is estimated that the model predictions are accurate to within 20 percent, or 3 °C, whichever is larger.

APPENDIX B: INTEGRAL THERMOCOUPLE TEMPERATURE MEASUREMENT

As mentioned in Chapter 3, the temperature readings from the integral thermocouples must be corrected, as a heat flux exists across the silver solder junction. The correction is based on reference [11].

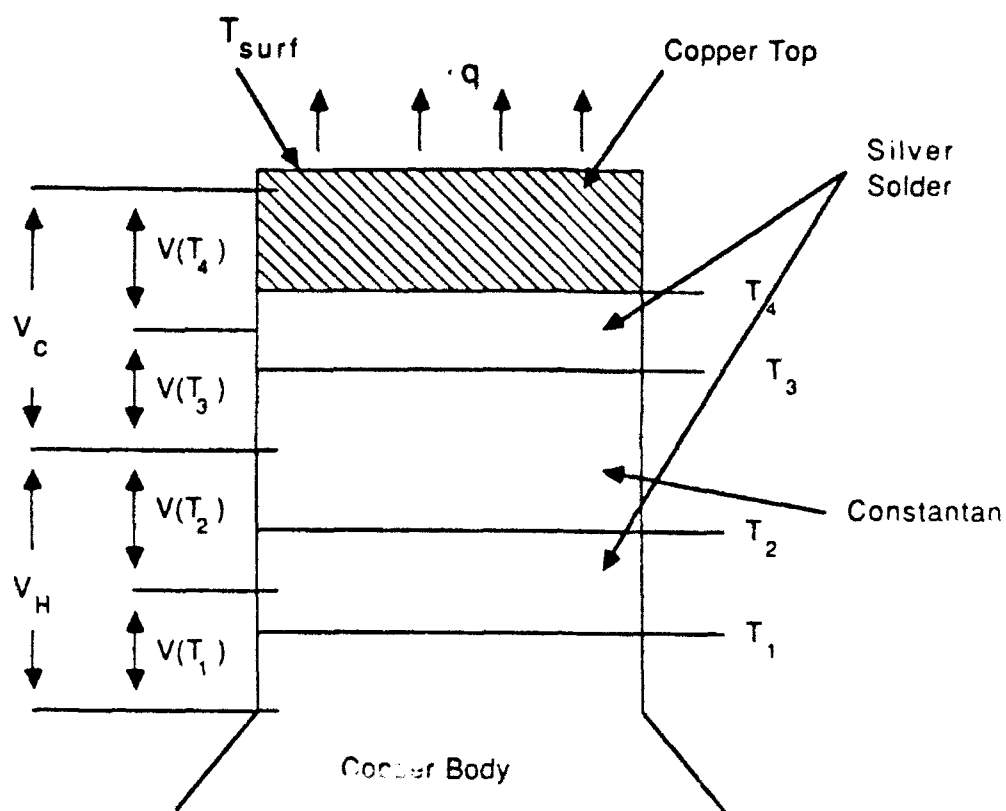
A closer study of the integral thermocouple design shown in Figure B.1a, reveals that the laminate can be viewed as two thermocouples, namely, copper-silver and silver-constantan. Here, the junctions are well defined planes marked by the boundaries of the constantan and copper. The voltage measurement recorded by the data acquisition is actually the sum of the two thermocouples in series as shown in Figure B.1b, the equivalent compensated circuit is shown in Figure 6.1.2c. This requires individual calibrations for both the copper-silver and silver-constantan thermocouples which were performed and the results are presented in Figure B.2, along with their polynomial fits, provided in Table B.1.

Table B.1: Thermocouple calibration

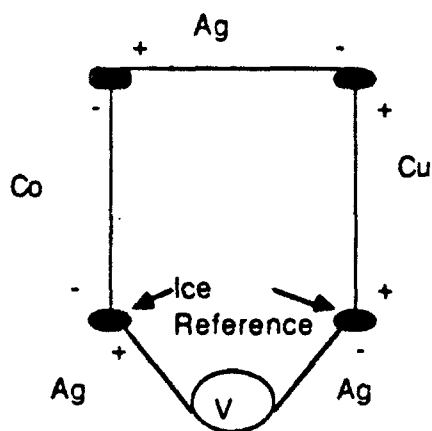
Polynomial Coefficient	Copper- Constantan CuCo	Copper- Silver CuAg	Constantan- Silver CoAg
a_0	7.2633364e-07	-8.2093389e-06	-5.3587533e-06
a_1	3.8522987e-05	1.5605573e-06	4.0999952e-05
a_2	4.3124505e-08	-1.0782581e-08	-5.3762608e-08
a_3	2.2868553e-11	1.8549296e-10	9.1690699e-10
a_4	-4.4466612e-13	-1.4160927e-12	-4.7932901e-12
a_5	1.7744421e-15	5.7250733e-15	1.4669923e-14
a_6	-3.3649500e-18	-1.1647572e-17	-2.5512934e-17
a_7	2.4993808e-21	9.3373451e-21	1.8473597e-20

Where, $V = a_0 + a_1T + a_2T^2 + \dots + a_nT^n$ and

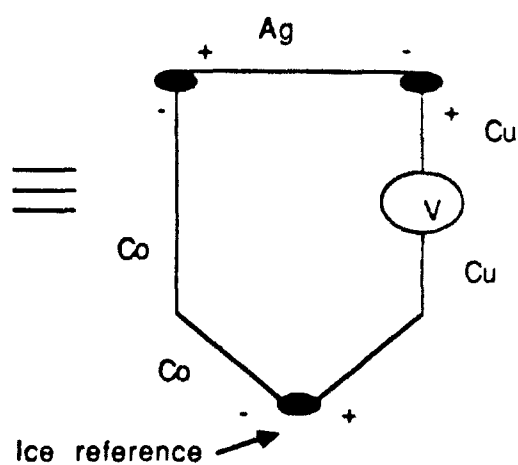
T = Temperature in degrees Celsius
 V = Thermocouple voltage in volts



(a)



(b)



(c)

Figure B.1: Integral thermocouple calibration analysis

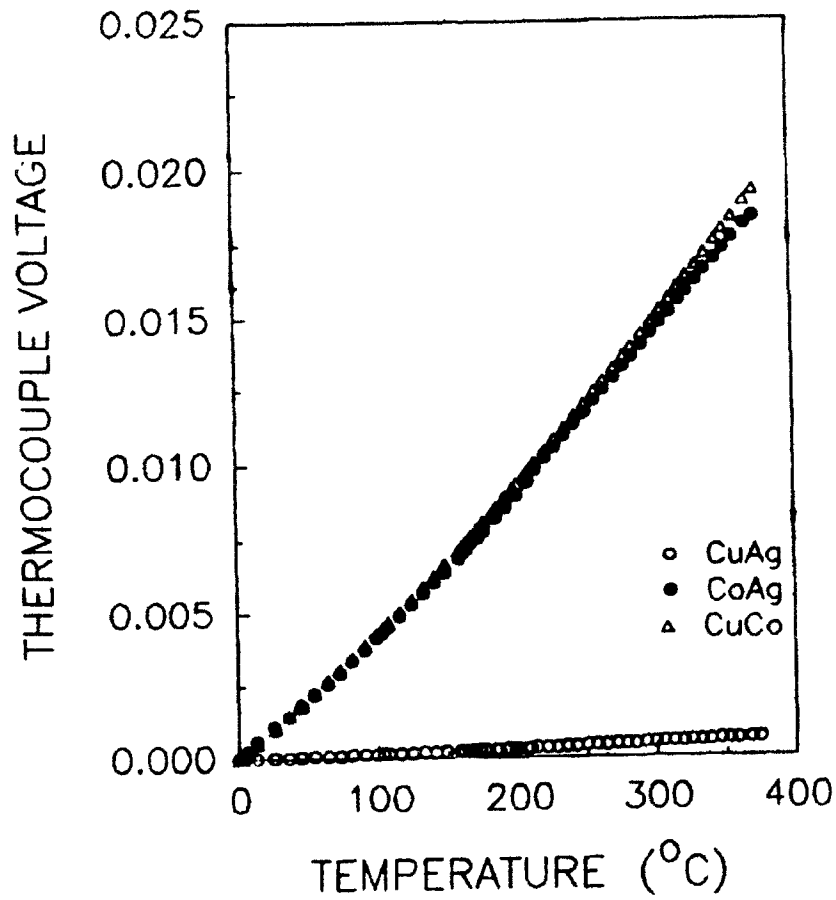


Figure B.2: Calibration results

The corrected heat flux from the surface can then be written as

$$q = K_{Ag} \frac{T_1 - T_2}{\Delta x_{Ag}} = K_{Co} \frac{T_2 - T_3}{\Delta x_{Co}} = K_{Ag} \frac{T_3 - T_4}{\Delta x_{Ag}} \quad (A.2.1)$$

from the first equality in (A.2.1) we get:

$$\frac{K_{Ag}}{\Delta x_{Ag}} T_1 - \left\{ \frac{K_{Ag}}{\Delta x_{Ag}} + \frac{K_{Co}}{\Delta x_{Co}} \right\} T_2 + \frac{K_{Co}}{\Delta x_{Co}} T_3 = 0 \quad (A.2.2)$$

Similarly from the second equality in (A.2.1) we get:

$$T_1 - T_2 - T_3 + T_4 = 0 \quad (\text{A.2.3})$$

The voltages measured by the equipment are:

$$V(T_1) + V(T_2) = V_H \quad (\text{A.2.4})$$

$$V(T_3) + V(T_4) = V_c \quad (\text{A.2.5})$$

We have four equations, A.2.2 through A.2.5 and four unknowns $T_{1,2,3,4}$. Having already obtained the calibrations for the various thermocouples, using a Gauss-Seidel iterative method, we can evaluate the unknowns.

The heat flux at the surface is given by equation (A.2.1) and the surface temperature is evaluated by extrapolation using equation A.2.6:

$$T_{\text{surf}} = T_4 - q \frac{\Delta x_{\text{Cu}}}{k_{\text{Cu}}} \quad (\text{A.2.6})$$

APPENDIX C:
EXPERIMENTAL RESULTS REFERENCE

This section presents a complete set of the closed-system, single-component test data taken with the smooth surface. A table of values giving many calculated parameters is also given for reference.

Table C.1: Experimental Results

Nozzle	\dot{Q} cc/s	$\dot{n} \times 10^{-6}$ s^{-1}	CHF W/cm^2	ΔT $^{\circ}C$	h $W/cm^2 K$	δ μm
TG.3	4.33	4.39	642	30	21.4	134
	5.16	5.28	810	35	23.1	152
	5.93	6.15	893	36	24.8	190
	6.65	7.29	907	36	25.2	245
	7.33	8.71	983	39	25.9	255
TG.4	4.55	4.42	672	30	22.4	136
	5.25	5.18	692	30	23.1	164
	5.75	5.74	753	32	23.5	193
	6.36	6.53	800	34	24.0	257
	7.32	7.73	862	35	24.6	276
TG.5	4.44	4.09	752	36	20.9	147
	5.14	4.77	856	38	22.5	165
	6.01	5.62	895	38	23.6	193
	6.72	6.31	943	38	24.8	211
	7.45	7.20	947	36	26.3	239
TG.6	4.49	3.55	458	22	20.8	125
	5.21	4.20	592	27	21.9	186
	5.93	4.92	703	32	22.0	213
	6.66	5.72	760	34	22.4	260
	7.46	6.58	781	33	23.7	303
TG.7	5.27	3.83	608	28	21.7	230
	6.07	4.61	715	32	22.3	277
	6.79	5.17	744	33	22.5	296
	7.50	5.86	826	36	22.9	347

Figures C.1 through C.5 show the experimental heat flux versus superheat curves for the cases in the above table.

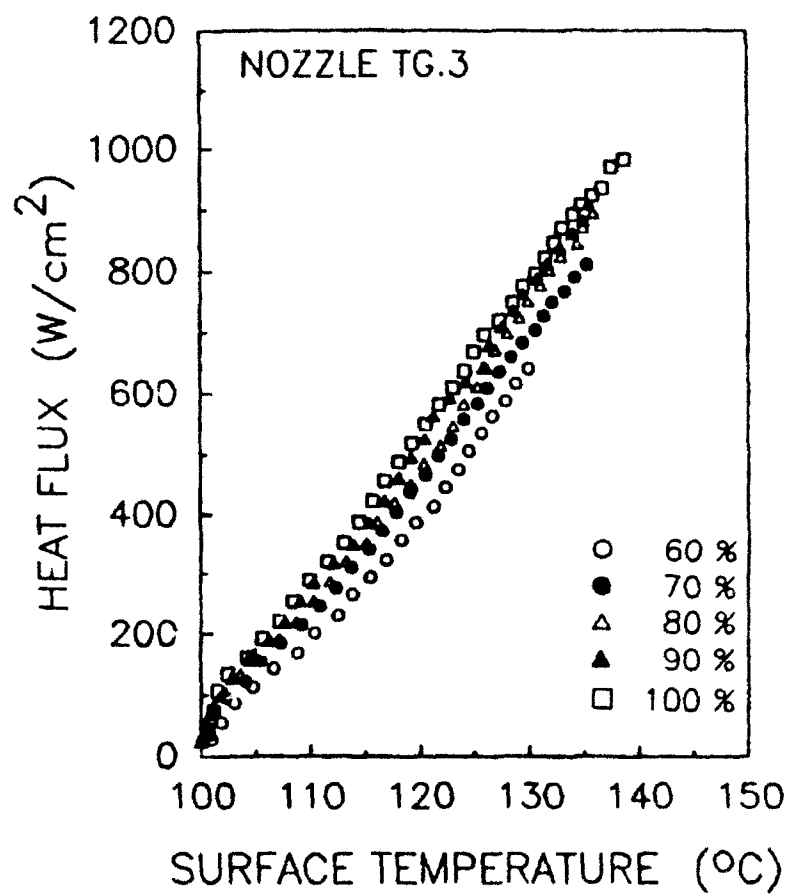


Figure C.1: Heat flux vs. superheat, nozzle TG.3

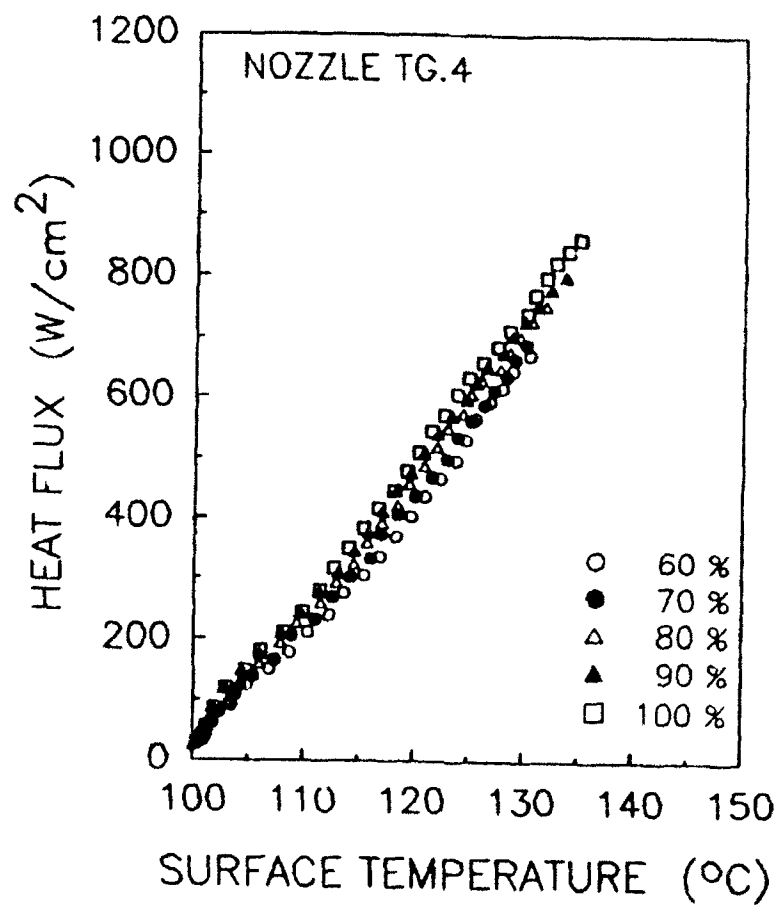


Figure C.2: Heat flux vs. superheat, nozzle TG.4

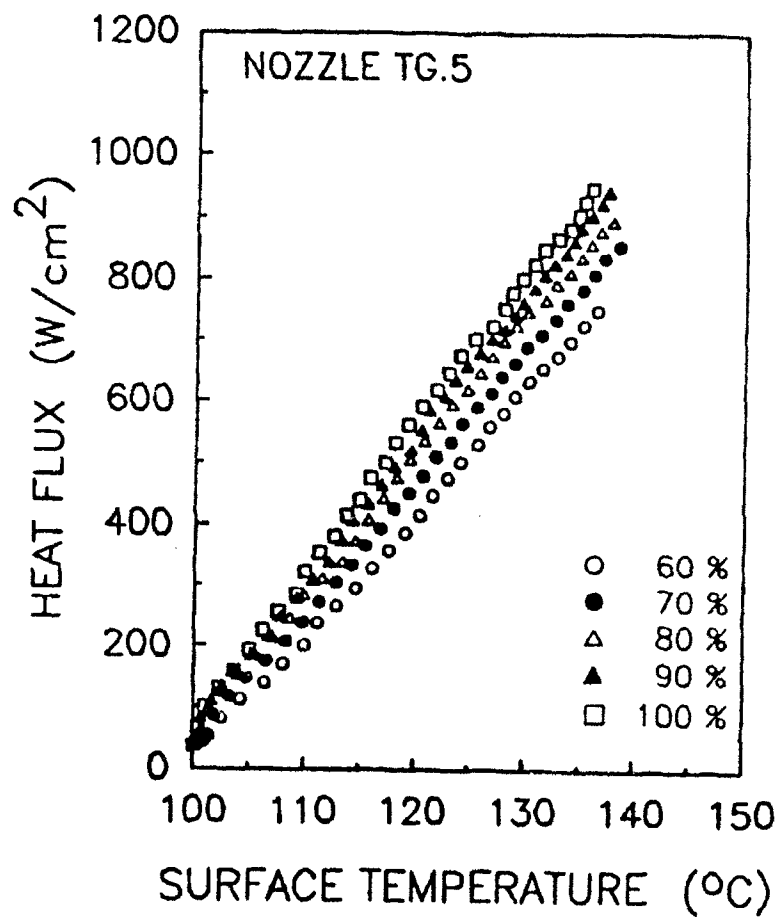


Figure C.3: Heat flux vs. superheat, nozzle TG.5

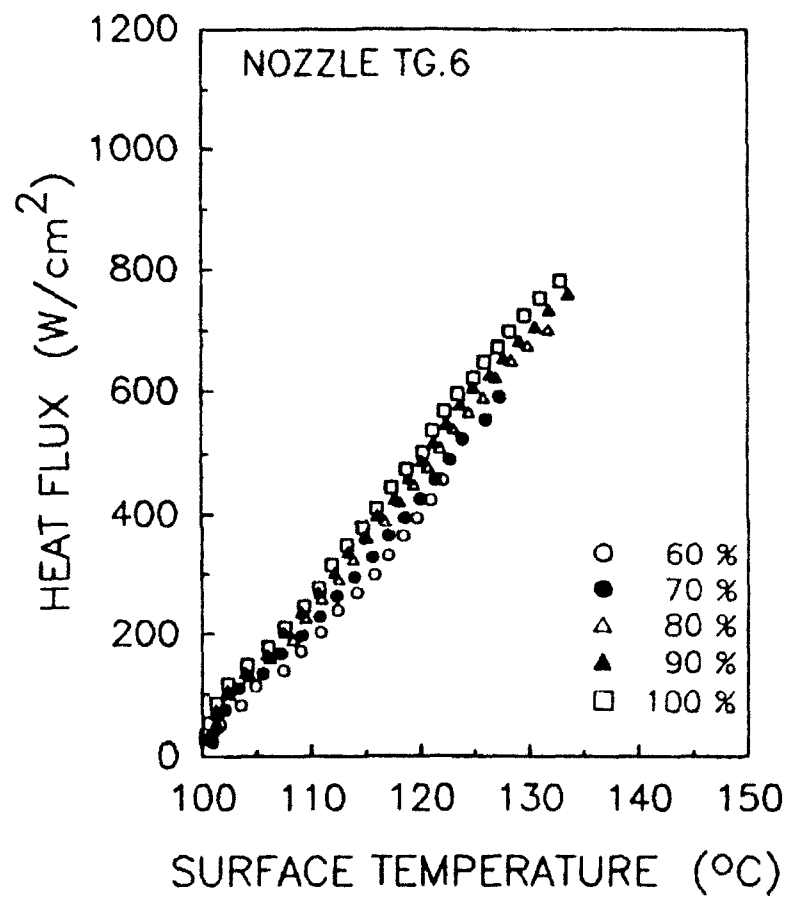


Figure C.4: Heat flux vs. superheat, nozzle TG.6

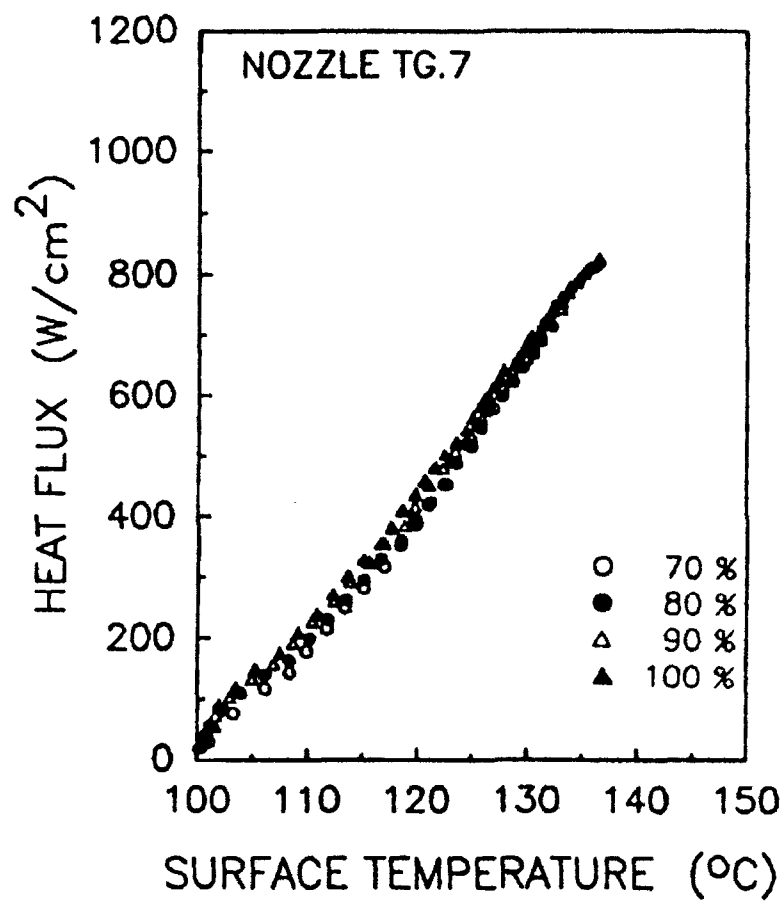


Figure C.5: Heat flux vs. superheat, nozzle TG.7